Characterizing the Anisotropic Electrical Properties of 3D Printed Conductive Sheets

A.P. (Alexander) Dijkshoorn

MSc Report

Committee:
Prof.dr.ir. G.J.M. Krijnen
Dr.ir. E. Dertien
M. Schouten, MSc
Dr.ir. T.H.J. Vaneker

June 2019

019RAM2019
Robotics and Mechatronics
EE-Math-CS
University of Twente
P.O. Box 217
7500 AE Enschede
The Netherlands

Summary

This study introduces a model and characterization techniques to investigate anisotropic, electrical properties of conductive 3D-printed sheets, where anisotropy is induced by 3D-printing. A model is presented that predicts the electrical properties of 3D-printed conductors based on the combination of electrical bulk and interface properties in and between the printed traxels (track elements). The model shows the importance of the relative interface impedance for the conduction mode through samples. An RC-model describes the bulk properties of the conductive polymer composite with quantum-tunneling. Dielectric impedance spectroscopy is used to measure the total impedance, on which the bulk material and electrical interface parameters can be fitted. High permittivity values are determined from measurements with the RC-model, which are likely too high because of incomplete knowledge of the structure on the nano-level. Samples are fabricated with FDM, giving rise to the electrical interfaces. The nature of these electrical interfaces is still unclear. The use of the SEM voltage contrast method is presented to determine the potential distributions of 3D-printed sheets. Through pixel-wise calibration and curve fitting a reliable qualitative voltage distribution can be obtained. IR thermography is implemented to characterize the power dissipation in samples. A frequency analysis of the temperature of the harmonically heated sample, called lock-in thermography, can be used to improve the measurements. High frequency measurement methods for VCSEM and IR thermography are proposed.

The developed modelling and measurement methods show good consistency of the qualitative results when applied to the same sample and can therefore be used alongside each other. Quantitative measurements are shown as well, however they still require improvements of the developed methods. All in all the model and characterization methods show promising results, enabling improvement of 3D-printed transducer designs, and exploit electrical properties of 3D-printed conductors.

Dankwoord

Vanaf eind september 2018 heb ik met veel plezier aan de totstandkoming van deze thesis gewerkt. Op een ijskoude ochtend las ik, gehuld in drie lagen kleding en een te koude slaapzak in het prachtige IJsland, een mailtje van Gijs over een model waar hij mee bezig was voor geleiding in 3D-prints. Het idee sprak me direct aan en bij thuiskomst mocht ik er mee aan de slag. Daarom wil ik Gijs graag bedanken voor de kans om aan dit project te werken. Zijn enthousiasme over het project en daarnaast het vertrouwen en de vrijheid die hij me gaf om mijn interesses te volgen binnen het onderzoek stel ik erg op prijs.

Daaropvolgend kon ik tijdens het dagelijks reilen en zeilen altijd terecht bij Martijn voor hulp. Ondanks zijn eigen drukke schema, had hij altijd wel tijd om te helpen met de dingen waar ik zelf niet uit kwam (of dat nou berekeningen, printen, metingen of het verslag waren, hij had altijd een oplossing), bedankt hiervoor. Ik kijk nog steeds uit naar zijn nieuwe Diabase koekjes en taart icing extruder, een ideaal project voor gepersionaliseerde RAM versnaperingen. Daarnaast wil ik Gerjan bedanken voor zijn hulp met het printen en met meten in de gevallen Martijn bij TMSI was.

In gevallen van nieuwe experimenten kon ik bouwen op de bij vlagen onvindbare Remco (ook wel bekend als Pino in de wandelgangen). Hem wil ik bedanken voor zijn hulp met de experimenten, zijn gigantische praktische kennis en vooral ook de goede sfeer in het lab. Zijn vaardigheid om “in de ruis te roeren” heeft menig van mijn SEM plaatjes mooier gemaakt.

Verder wil ik de dr. Dertien en dr. Vaneker bedanken voor het plaatsnemen in mijn commissie en voor de feedback tijdens de halfway meeting.

In de gevallen dat er een korte pauze of ontspanning nodig was kon ik altijd rekenen op de gezelligheid van mijn medestudenten en mensen bij RAM. Of de koffiebois ooit rijk gaan worden van het investmant capital blijft echter wel de vraag.

Als laatste wil ik mijn ouders, broer en vrienden bedanken voor hun steun en gezelschap tijdens de afgelopen 6 jaar studeren. Op de momenten dat het nodig was, kon er een biertje gedronken worden of een stevige wandeling gemaakt worden. Zonder hen was deze thesis er niet gekomen. En nu op naar het volgende avontuur.

Alexander Dijkshoorn
Enschede, Thursday 30th May, 2019

Contents

List of Abbreviations

BSE	Backscatter Electron
CB	Carbon Black
CFRP	Carbon Fiber Reinforced Polymer
CNT	Carbon Nanotubes
CPC	Conductive Polymer Composite
EEM	Eigenmode/Eigenvector Model
EIS	Electrochemical Impedance Spectroscopy
ET	Everhart-Thornely
FDM	Fused Deposition Modeling
FEM	Finite Element Method
IC	Integrated Circuit
IR	Infrared
KK	Kramers-Krönig
LCR	Inductance (L), Capacitance (C), and Resistance (R)
NTC	Negative Temperature Coefficient
PDE	Partial Differential Equation
PE	Primary Electron
PTC	Positive Temperature Coefficient
RMSE	Root Mean Squared Error
SE	Secondary Electron
SEM	Scanning Electron Microscopy
SNR	Signal-To-Noise-Ratio
TPU	Thermal Polyurethane
Traxel	Track Element
TTL	Through-The-Lens
VCSEM	Voltage Contrast Scanning Electron Microscopy

List of Symbols

Parameter	Unit	Description
Γ	-	Parameter describing the conduction mode
δ	m	Gap width
ϵ	$\mathrm{F\,m^{-1}}$	Electrical permittivity
ϵ	-	Emissivity
μ	Pa s	Dynamic viscosity
ρ	$\Omega\,\mathrm{m}$	Electrical bulk resistivity
σ	$\Omega\,\mathrm{m^2}$	Contact resistivity
σ_{SB}	$\mathrm{W\,m^{-2}\,K^{-4}}$	Stefan-Boltzmann constant
ϕ	eV	Work function (or potential in V in appendix A)
χ	eV	Electron affinity
ω	$\mathrm{rad\,s^{-1}}$	Angular frequency
A	$\mathrm{m^2}$	Area
B	$\mathrm{K^{-1}}$	Thermal expansion coefficient
C	F	Electrical capacitance
C_0	$\mathrm{F\,m^{-2}}$	Electrical contact capacitance per contact area
C_p	$\mathrm{J\,kg^{-1}\,K^{-1}}$	Specific heat at constant pressure
E	J	Energy
f	Hz	Frequency
g	$\mathrm{m\,s^{-2}}$	gravitational acceleration
h	$\mathrm{W\,m^{-2}\,K^{-1}}$	Convection coefficient
H	m	Sample height
I	A	Electrical current
J	$\mathrm{A\,m^{-2}}$	Current density
k	$\mathrm{W\,m^{-1}\,K^{-1}}$	Thermal conductivity
L	m	Sample length
N	-	Number of traxels
p	Pa	Pressure
P	W	Power
Q	J	Heat
R	Ω	Electrical resistance
R_{s}	$\mathrm{J\,kg^{-1}\,K^{-1}}$	Specific gas constant
T	K	Temperature
U	V	Voltage
V	V	Voltage (appendix)
W	m	Traxel width
Z	Ω	Electrical impedance

1 Introduction

This report describes the work done by Alexander Dijkshoorn for his Master Assignment. The goal of the assignment is to verify a model and develop methods to characterize 3D-printed conductive sheets. The model and developed methods will be used to study the effect of the 3D-printing process on the electrical properties of prints.

This chapter introduces the underlying context for the study followed by the challenges and questions that will be researched for the project, as well as the methods. Finally an overview of the report structure is given.

1.1 Context

3D-printing transducers is an upcoming research area (1), where already multiple 3D- printed piezo resistive, EMG and capacitive sensors have been demonstrated (2) and significant research has been done on electrical properties of conductive-polymer composites for printing (3; 4; 5). The field of 3D printing of transducers and electronics in particular has many different implementations, of which almost all of them are still under research. Noteworthy examples are the embedding of components during the printing process, filling channels with conductive ink, inkjetting conductive materials and multi-material Fused Deposition Modeling (FDM) printing (with silver ink (6) or with conductive particle polymers composites (4; 1). All but the last one have as a disadvantage that conductors and elements have to be included during or after printing. The possibility to also co-print the conductive structures with one low-cost printer makes FDM the most prolific low-cost technology for printing electronics (4; 2). With FDM a material, e.g. a thermoplast, is extruded through a nozzle onto a build plate where needed. The head and/or built plate can move to deposit one horizontal plane at a time, as is schematically shown in figure 1.1.

Various materials are commercially available for printing conductive structures with FDM. For most of them conductivity is obtained by mixing in conductive additives like carbon black (8; 9) or carbon nano tubes (CNT) (1). However, FDM printing conditions remarkably affect the electrical properties between adjacent fibers, yielding anisotropic resistivity. Various studies point out the difference in resistance for different print directions, where the conductive path in parallel with the printed tracks has a higher conductance than the paths perpendicular to the layers (4; 10; 11). Possible given physical explanations of the resistance between tracks are due to voids and bonding conditions like imperfect fusion between layers (4; 10; 11). Substantiation of these claims can be found in SEM imaging of prints showing imperfect fusion, as shown in figure 1.3. The raster angle (infill angle) is therefore proposed as a major parameter for changing the resistance of prints (12; 5; 10). Next to this it has already been shown by Wolterink that it is possible to use the contact resistance between layers for the design of capacitive force sensors, where the capacitance between printed layers is dominant due to a high interlayer resistance

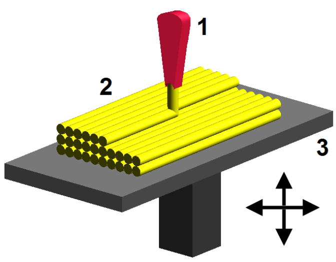

Figure 1.1: Fused Deposition Modelling: 1. extrusion of (molten) material, 2. print under construction, 3. (moving) build plate (7).

for high enough frequencies (13). Insight in the anisotropic electrical behaviour can be gained by developing appropriate models. Next to this electrical characterization of transducers has primarily focused on global impedance (or resistance) measurements and homogenized properties (2; 14; 3; 11), whereas the entire distribution of the electrical impedance is of interest with enough resolution and precision to measure at the 3D-print resolution. By implementing characterization methods that can measure the electrical properties locally in an effective manner, it will be possible to validate models and it will be possible to study single-layer, 3D-printed transducers more effectively.

(a) Example of an FDM-printed whisker sensor with integrated strain sensors for force sensing (15).

(b) Example of 3-D printed sEMG electrodes, printed using a combination of conductive and dielectric TPU (16).

Figure 1.2: Examples of FDM-printed sensors using a combination of conductive and dielectric TPU.

1.2 Project Goals

With the challenge as stated above clear objectives can be determined. The main research question becomes:

"How can the anisotropic, electrical characteristics of 3D-printed, conductive structures be modelled and determined?"

This study will focus on the main electrical characteristics that are of interest for 3D-printed transducers. This thesis will treat the modelling, simulating and measuring of the electrical characteristics of 3D-printed conductive structures. This gives rise to the following subquestions:

- How can the electrical characteristics of 3D printed conductive structures be modelled, to gain a deeper understanding?
  Are the results of the analytical model verified by FEM simulations?

Figure 1.3: SEM picture of printed ABS tracks with imperfect fusion (15).

- How can the electrical characteristics of 3D printed conductive structures be measured experimentally?
- Do results of experimentally determined electrical characteristics of 3D-printed conductors validate the analytical models?

To be able to answer these questions, several steps will be taken.

1.3 Approach

The project goals are mainly research oriented, so a scientific approach will be used. Modelling and experiments will be used to be able to answer the research questions. Literature will be studied for the status quo of modelling and a model of Gijs Krijnen will be used and extended if needed. FEM simulations based on this model will be performed for verification. The (electrical) properties of the conductive material and of printed samples will then be studied by means of experiments.

As mentioned earlier an experimental method suitable for measuring local anisotropic electrical properties needs to be found. Most methods make use of indirect measurements with ill-posed conversions and measure either local or homogenized properties. Among these methods are four-point probing methods as used for anisotropic solids (Montgomery method) (17) and textiles (van der Pauw method) (18; 19), electrical impedance tomography (a technique that determines the internal conductivity distribution from a solid using electrodes fabricated along the boundary of the conductive material) as used for detecting defects in carbon fiber reinforced polymers (CFRP) (20; 21) and for strain sensor design (22), an Eddy current method (inducing Eddy currents with an excitation coil and measuring them with a pick-up coil) as used for characterization of CFRP (23; 24), magnetic sensing of the current-induced magnetic field (measuring the magnetic field as result of a current density) (25; 26), IR thermography (thermal imaging of the resistive heating due to a current density) by induction (27) or by Joule heating (28) and finally voltage contrast scanning electron microscopy (measuring a differences in contrast due to a voltage distribution with a scanning electron microscope).

In this report it will be shown that IR thermography, as used for studying heating power in 3D-printed samples (10), characterization of CFRPs (29) and characterization of conductive woven textiles (28) can also be used for studying the anisotropic electrical properties of 3D-printed samples. And voltage contrast scanning electron microscopy (VCSEM), used to characterize conducting networks in CNT composites (30) and failure localization in integrated circuits (31), can be applied to 3D printed conductors. Both methods are chosen for their ability to measure the entire sheet surface with currently available tools and their insensitivity to contact resistance (in contrast to probe-based methods).

1.4 Report Structure

Chapter 2 will cover the modelling methods and numerical verification. Chapter 3 will discuss the properties of the used material and will treat the global electrical measurements. The fabrication of samples for the characterization experiments will be explained in chapter 4. Next chapter 5 goes into the voltage contrast measurement method, followed by chapter 6 on IR thermography. In chapter 7 the corresponding results are shown and compared. Finally chapter 8 concludes the report.

2 Modelling

In this chapter an overview of the current modelling methods in literature is given, followed by a derivation and discussion of the model investigated in this research. Furthermore a numerical model is presented and compared to the model for verification.

2.1 Related Work

3D-printed conductive objects have anisotropic electrical properties as described in section 1.1. For a model to properly describe the conductivity in anisotropic 3D-printed samples it is therefore of importance that local effects in and between printed track elements, “traxels”[1], are included in a model. In various fields of research models for samples with anisotropic resistivity are developed as discussed below.

In the field of conductive textiles and fabrics one often works with resistor networks to model the anisotropic electrical behaviour (28; 32), as shown in figure 2.1. These models however are meant for woven fabrics, which only make contact at discrete locations where the threads touch each other. This makes a discretized resistor network a logical choice, since there are only electrical connections at discretized locations. These methods are strongly related to measurement methods, to be able to determine the resistivity and anisotropy for different weaving patterns with electrical probes (33; 34). Although modelling 3D-printed conductive samples by discretizing into an electrical network is possible, it does not directly present clearly interpretable equations.

Homogenized properties of equivalent electrical conductivity tensors are often used in the field of composites (29; 35; 36). In these cases a homogeneous material is assumed, for this the partial differential equation (PDE) can be evaluated analytically for simple cases (36) and numerically for more complex situations (29). With this approach it is not possible to model local properties properly, furthermore it is difficult to solve the PDE with boundary conditions on particular traxels. Therefore it is not chosen as method to study 3D-prints for this research. For large collections of traxels the results could start to resemble the homogeneous case with anisotropic conduction. In appendix A a derivation of a continuum model for 3D-prints is presented.

Finally some research represents anisotropic structures by means of fitting a simple equivalent circuit to experimental data from impedance spectroscopy measurements. This has in the past been done for among others characterization of carbon fiber reinforced polymers (CFRP) (37) and 3D-printed conductors (38), however it is limited in the physical behaviour it can represent.

[1] "Traxel" is a word introduced to describe the individual printed track elements like e.g. “voxel” for a volume element.

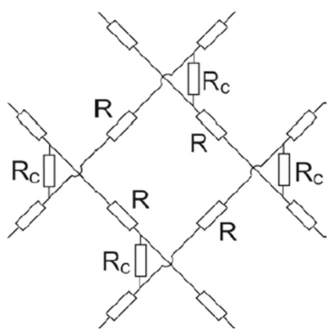

Figure 2.1: Equivalent electrical model for a fragment of woven textile (28).

The literature with respect to modelling of conductive 3D-prints is limited. A simple model for anisotropic resistance of 3D-printed structures was presented by (15). It was based on SEM images that showed incomplete fusion between the 3D-printed traxels in a sample (figure 1.3). In this model three different resistances contribute to the total resistance of the print, as shown in figure 2.2a. The layer resistance R_L represents the bulk material resistance in the direction of the 3D-printed traxels and has the highest conductance. Its resistivity is only defined by the material and the printing parameters. The intralayer resistance R_{IL}, R_{IR} describes the resistance within a horizontal layer between two 3D-printed traxels. Finally the interlayer resistance R_{IL} gives the resistance between traxels in two vertical layers, lowering the conduction in vertical direction.

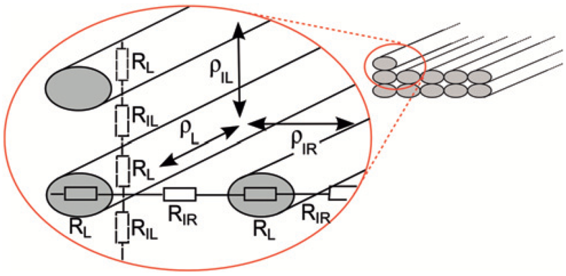

(a) Model of conductance of 3D printed structures by (15).

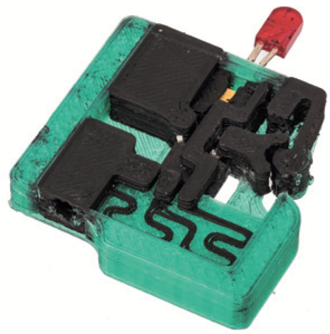

(b) A 3D-printed flash light circuit with resistances designed via equation 2.1 (15).

Figure 2.2: A model of conductance in 3D-prints (left) used to calculate resistances in a printed circuit (right) (15).

In the research with this model, measurements were done on samples to determine the three different resistivity terms. Based on this model, an equation for the one-dimensional resistance of a 3D-printed object was presented (15):

$$R = \rho_L \frac{L}{A} + \rho_{IL/RL} \frac{N_{\text{transitions}}}{A} \tag{2.1}$$

Where L is the length of a track, A the cross-section area and $N_{\text{transitions}}$ the number of transitions between tracks. With this model resistors were designed and operated in a 3D-printed circuit, as shown in figure 2.2b.

The model of Hampel incorporates the fundamental concepts of bulk and contact properties to describe the resistance, however limits this with equation 2.1 to a one-dimensional situation and furthermore only represents the DC case. This is not sufficient in case 2D-behaviour and frequency behaviour need to be modelled. The model of Gijs Krijnen incorporates the contact capacitance between tracks as well as the bulk permittivity to be able to describe the impedance of prints. Next to this the tracks are modelled in a 2D fashion and meanders can be included to be able to better represent 3D-printed sheets. Due to the possibility to model the impedance of 2D prints locally, without homogenization over the entire sample or having to convert the geometry into an unnecessarily discretized electrical circuit, the model of Gijs Krijnen will be used for this study.

2.2 Analytical Model

The model of Gijs Krijnen tries to model the conduction in 3D-printed structures as a collection of traxels, assuming they exist. The model describes the most important electrical properties for 3D-printed structures. A model is built out of a finite number of traxels, which form the dis-

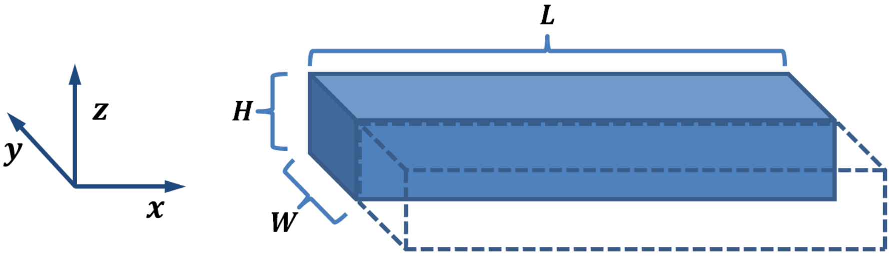

Figure 2.3: Schematical drawing of the 3D printed tracks as present in the model.

crete deposited line elements of which an FDM 3D-printed material consists. Figure 2.3 shows the geometrical lay-out of a print, where a modelled traxel has a length of L in x-direction, is W wide in y-direction and is H high in the z-direction. Traxels are stacked against each other in y-direction and voltage and current boundary conditions are prescribed on the ends of the track (the yz-planes). Every traxel has a certain bulk resistivity and permittivity, whereas the traxels are connected via contact resistance and contact capacitance over their contact surfaces. Due to these electrical connections current can flow through traxels and to neighbouring traxels, as shown in figure 2.4a. This interaction leads to changing potentials and currents in the individual traxels, which depend on each other and need to be solved together. For N traxels there are $2N$ equations to be solved. The potential and current relations lead to a set of coupled differential equations which are solved using an eigenmode / eigenvector solution with coefficients determined by (given) boundary conditions. Note the similarity with the physical model of Hampel in figure 2.2a and in equation 2.1, which is basically the same for a 1D approach in the DC case.

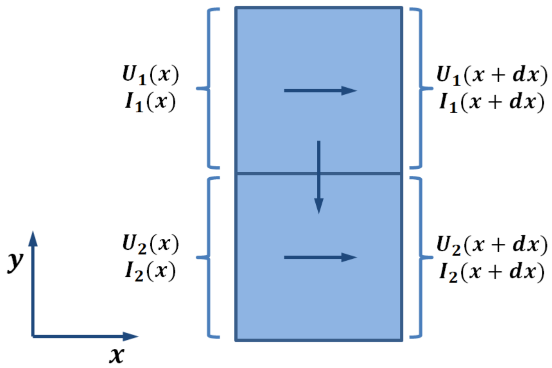

(a) Schematic interaction of the voltage and current between two neighbouring traxels slices of Δx wide.

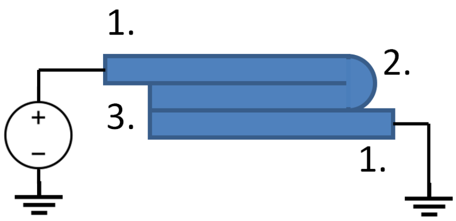

(b) Possible boundary conditions for traxels: 1. Prescribed Voltage, 2. Meandering End, 3. Open End.

Figure 2.4: Schematical drawings of the conduction in the model (left) and of the various boundary conditions (right).

For every traxel there are three possible boundary conditions, as illustrated in figure 2.4b. They all have their own implications for the voltage $U(x,t)$ and current $I(x,t)$ at the boundaries $x = 0$ and $x = L$:

- 1. Prescribed Voltage: a fixed voltage at a boundary because of the presence of a terminal or ground.
  $U(0,t) = U_{\text{prescribed}}$
- 2. Open End: a floating electrical voltage and no current flowing since there is no connection with other traxels or sources.
  $I(0,t) \propto \frac{\partial U(0,t)}{\partial x} = 0$

- 3. Meandering End: a connection to another traxel (normally a neighbouring traxel), causing an equal voltage and an equal but opposite current.
  $U_N(0,t) = U_{N-1}(0,t)$
  $I_N(0,t) = -I_{N-1}(0,t)$

The analytical model can be derived by considering the distributed electrical properties of the traxels and the contacts between the traxels, represented by an equivalent network as shown in figure 2.5.

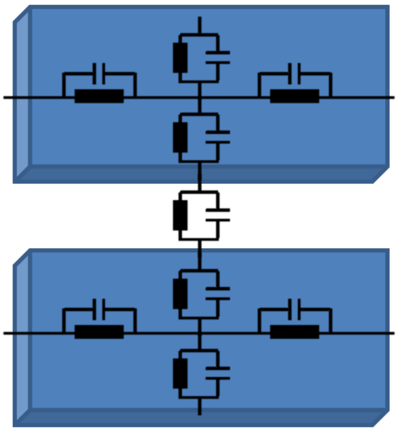

Figure 2.5: Equivalent circuit representation for the electrical properties of a slice of traxel Δx wide.

2.2.1 Derivation

The model starts from the expressions of the bulk and contact properties for a piece of traxel of Δx wide (like the slice in figure 2.3). The bulk resistance can be defined as $R_{\text{bulk}} = \frac{\rho \Delta x}{HW}$ with ρ being the volume resistivity of the material in Ωm. The bulk capacitance arises due to the permittivity of the material, and is described with $C_{\text{bulk}} = \frac{\epsilon_0 \epsilon_r HW}{\Delta x}$ with ϵ_0 the permittivity of vacuum in F m^{-1} and with ϵ_r the relative permittivity. The contact resistance is defined as $R_{\text{contact}} = \frac{\sigma}{A} = \frac{\sigma}{H\Delta x}$, with σ being the contact resistivity between two tracks in $\Omega\,\text{m}^2$. Finally the contact capacitance can be expressed as $C_{\text{contact}} = C_0 H \Delta x$ with C_0 being the contact capacitance per contact area in F m^{-2}.

For the model parallel traxels are placed directly next to each other in-plane. Each traxel has four important variables. On each end a current or a voltage condition is present. The system is solved in terms of the potential, where the boundary conditions are given in either $U = U_{\text{in/out}}$ or $\frac{\partial U}{\partial x} = 0$ This yields for every traxel two variables, the voltage $U(x,t)$ and its spatial derivative. The model aims at solving for these two variables at every location x. Based on the bulk and contact properties in figure 2.5 separate equations can be derived and put together. One challenge of this approach is to represent the vertical bulk properties (the voltage drops perpendicular to the contacts) in this approach. This can be solved by simplifying the vertical properties as additional term in the contact properties.

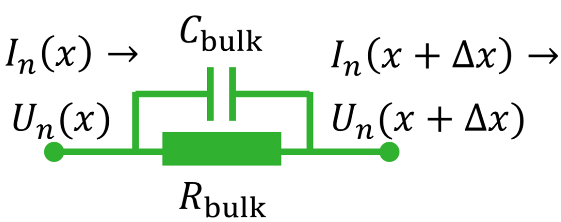

Figure 2.6: Equivalent circuit representation for the horizontal electrical bulk properties of a slice of traxel Δx wide.

Bulk Properties

A single piece of traxel is represented by means of a parallel resistor and capacitor as schematically shown in figure 2.6. The piece of traxel is Δx long, has a potential $U(x)$ and $U(\Delta x)$ on its ends and a current I flows through. For the equations an arbitrary n^{th} traxel is considered, therefore indication the variables U and I with n. The bulk resistor can then be expressed with $R_{\text{bulk}} = \frac{\rho \Delta x}{HW}$ and the bulk capacitor with $C_{\text{bulk}} = \frac{\epsilon_0 \epsilon_r HW}{\Delta x}$. Current flows through the traxels from left to right. On the left the current of traxel n can be expressed as the current that flows due to the potential difference over the section:

$$I_n(x,t) = \frac{\Delta U_n(x,t)}{R_{\text{bulk}}} + C_{\text{bulk}} \frac{\partial(\Delta U_n(x,t))}{\partial t} \tag{2.2}$$

By substituting the expressions for R_{bulk} and C_{bulk} one obtains:

$$I_n(x,t) = -\frac{U_n(x+\Delta x,t) - U_n(x,t)}{\frac{\rho}{HW}\Delta x} - \frac{\epsilon_0 \epsilon_r HW}{\Delta x} \frac{\partial}{\partial t}(U_n(x+\Delta x,t) - U_n(x,t)) \tag{2.3}$$

When taking the slice of traxel infinitesimally thin, the expression can be rewritten with partial derivatives:

$$I_n(x,t) = -HW\left(\frac{1}{\rho}\frac{\partial U_n(x,t)}{\partial x} + \epsilon_0 \epsilon_r \frac{\partial}{\partial t}\frac{\partial U_n(x,t)}{\partial x}\right) \tag{2.4}$$

When assuming only harmonic expressions for U_n and I_n, the Fourier transform can be applied, resulting in:

$$\hat{I}_n(x,\omega) = -HW\left(\frac{1}{\rho} + j\omega\epsilon_0\epsilon_r\right)\frac{\partial \hat{U}_n(x,\omega)}{\partial x} \tag{2.5}$$

This expression can be differentiated to x to give a second order expression for U_n:

$$\frac{\partial \hat{I}_n(x,\omega)}{\partial x} = -HW\left(\frac{1}{\rho} + j\omega\epsilon_0\epsilon_r\right)\frac{\partial^2 \hat{U}_n(x,\omega)}{\partial x^2} \tag{2.6}$$

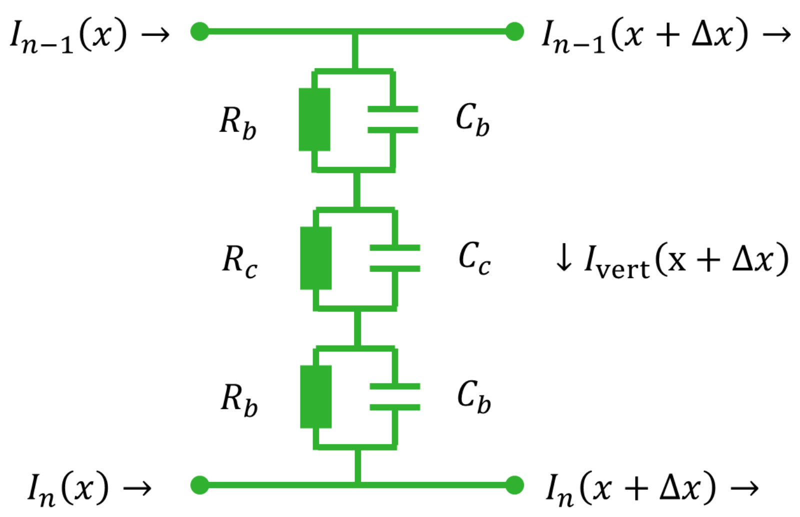

Figure 2.7: Equivalent circuit representation for the electrical contact properties c combined with the vertical bulk properties b of a slice of two neighbouring traxels of Δx wide.

Contact Properties

The contact between two pieces of traxel is also represented by means of a resistor and capacitor in parallel. The vertical bulk properties are combined in series as schematically shown in figure 2.7, based on the equivalent network in figure 2.5 to represent half of the traxel on both sides of the contact. An equivalent impedance can be derived for this circuit, for which the derivation is given in appendix B:

$$\hat{Z}_{\text{eq}}(\omega) = \frac{1}{H\Delta x}\frac{\rho W + \sigma + j\omega\rho\sigma W C_0 + j\omega\rho\sigma\epsilon_0\epsilon_{\text{r}}}{(1 + j\omega\rho\epsilon_0\epsilon_{\text{r}} + j\omega\sigma C_0 - \omega^2\rho\sigma\epsilon_0\epsilon_{\text{r}} C_0} \tag{2.7}$$

The pieces of traxel are Δx long, have a potential U on both ends and a current I flows through. For the equations an arbitrary n^{th} traxel is considered, with a neighbouring traxel $n-1$. Current flows through the traxels from left to right and can also flow through the contact impedance due to the potential difference. The equivalent impedance is already expressed in the Fourier transformed form, assuming harmonic functions. This is also done for the current balance:

$$-\left(\hat{I}_{n-1}(x+\Delta x,\omega) - \hat{I}_{n-1}(x,\omega)\right) = \frac{\hat{U}_n(x,\omega) - \hat{U}_{n-1}(x,\omega)}{\hat{Z}_{\text{eq}}(\omega)} \tag{2.8}$$

Furthermore a parameter Γ is introduced (which combines the bulk and contact properties):

$$\Gamma(\omega) = \frac{1}{W\left(1/\rho + j\omega\epsilon_0\epsilon_{\text{r}}\right)}\left(\frac{1 + j\omega\rho\epsilon_0\epsilon_{\text{r}} + j\omega\sigma C_0 - \omega^2\rho\sigma\epsilon_0\epsilon_{\text{r}} C_0}{\rho W + \sigma + j\omega\rho\sigma W C_0 + j\omega\rho\sigma\epsilon_0\epsilon_{\text{r}}}\right) \tag{2.9}$$

Substituting the expression for the equivalent impedance 2.7 in combination with the expression for Γ yields:

$$-\left(\hat{I}_{n-1}(x+\Delta x,\omega) - \hat{I}_{n-1}(x,\omega)\right) = H\Delta x W\left(\frac{1}{\rho} + j\omega\epsilon_0\epsilon_{\text{r}}\right)\Gamma(\hat{U}_n(x,\omega) - \hat{U}_{n-1}(x,\omega)) \tag{2.10}$$

When taking the slice of traxels infinitesimally thin, the expression can be rewritten with partial derivatives:

$$\frac{\partial \hat{I}_{n-1}(x,\omega)}{\partial x} = -HW\left(\frac{1}{\rho} + j\omega\epsilon_0\epsilon_{\text{r}}\right)\Gamma(\hat{U}_n(x,\omega) - \hat{U}_{n-1}(x,\omega)) \tag{2.11}$$

Combined Properties

The full equation can be found by combining the equations for bulk and contact properties by substituting equation 2.11 into equation 2.6 and rewriting (the term $-HW(\frac{1}{\rho} + j\omega\epsilon_0\epsilon_{\text{r}})$ occurs on both sides of the equation and drops out):

$$\frac{\partial^2 \hat{U}_{n-1}(x,\omega)}{\partial x^2} - \Gamma(\omega)(\hat{U}_n(x,\omega) - \hat{U}_{n-1}(x,\omega)) = 0 \tag{2.12}$$

Equation 2.12 describes the case for a traxel with a single neighbour, so at the edge of a printed sample. In the general case however there is a neighbouring traxel on both sides, additional terms for the neighbouring traxel need to be included.

$$\frac{\partial^2 \hat{U}_n(x,\omega)}{\partial x^2} + \Gamma(\omega)(\hat{U}_{n-1}(x,\omega) - 2\hat{U}_n(x,\omega) + \hat{U}_{n+1}(x,\omega)) = 0 \tag{2.13}$$

Note that the last 3 terms of this equation would go over into $\frac{\partial^2 \hat{U}}{\partial y^2}$ for decreasing traxel width (since Γ contains the term $1/W^2$), resolving the Laplacian for homogeneous anisotropic materials (39). Equation 2.13 needs to be solved for every traxel with two neighbours, whereas equation 2.12 needs to be solved for the two traxels on the outer edge. So in this way any 2D structure with a finite number of parallel traxels can be described. The method is not restricted to 2D-structures though, it can be extended to 3D-structures by taking upper and lower neighbouring traxels into account in equation 2.13.

Solving the Equations

Equations 2.13 and 2.12 can be combined into a system of equations that describe the entire system. To solve for this system of equations, the system can be turned into an eigenvalue problem. This is illustrated with an example with three traxels, from which the traxels are numbered 1 till 3. The system consists of three second order differential equations, hence the expected outcomes are something in the form of:

$$\hat{U}_n(x,\omega) = \sum_{i=1}^{6} C_i e^{\lambda_i x} \tag{2.14}$$

Substituting this in the system equations for the second row ($n = 2$) yields e.g.:

$$\lambda^2 \hat{U}_2(x,\omega) - \Gamma(\omega)(2\hat{U}_2(x,\omega) - \hat{U}_1(x,\omega) - \hat{U}_3(x,\omega)) = 0 \tag{2.15}$$

Combining the three equations in matrix form yields the eigenvalue problem ($(A-\lambda^2 I)\vec{U} = \vec{0}$), where in this specific case the eigenvalues are given by λ^2 and the whole thing is multiplied by -1:

$$\begin{bmatrix} (\lambda^2+\Gamma) & -\Gamma & 0 \\ -\Gamma & (\lambda^2+2\Gamma) & -\Gamma \\ 0 & -\Gamma & (\lambda^2+\Gamma) \end{bmatrix} \begin{Bmatrix} U_1 \\ U_2 \\ U_3 \end{Bmatrix} = \begin{Bmatrix} 0 \\ 0 \\ 0 \end{Bmatrix} \tag{2.16}$$

The eigenvalue problem has a nontrivial solution when the determinant of the matrix equals 0. From this the eigenvalues are found to be $\lambda^2 = 0$, $\lambda^2 = \Gamma$ and $\lambda^2 = 3\Gamma$. In this way six individual terms for λ and the corresponding eigenvectors are obtained:

$$\lambda_1 = -\lambda_2 = 0, \qquad \vec{v}_1 = \vec{v}_2 = (1,1,1)^{\mathrm{T}} \tag{2.17}$$

$$\lambda_3 = -\lambda_4 = -\sqrt{\Gamma}, \qquad \vec{v}_3 = \vec{v}_4 = (-1,0,1)^{\mathrm{T}} \tag{2.18}$$

$$\lambda_5 = -\lambda_6 = -\sqrt{3\Gamma}, \qquad \vec{v}_5 = \vec{v}_6 = (1,-2,1)^{\mathrm{T}} \tag{2.19}$$

The solutions arising from these eigenvalues and vectors are in the form of (with $\vec{\hat{U}}(x,\omega)$ to indicate that it is a vector with the complex voltage amplitude for every traxel):

$$\vec{\hat{U}}(x,\omega) = \alpha_1\vec{v}_1 + \alpha_2\vec{v}_2 x + \alpha_3\vec{v}_3 e^{(-\sqrt{\Gamma}x)} + \alpha_4\vec{v}_4 e^{(\sqrt{\Gamma}x)} + \alpha_5\vec{v}_5 e^{(-\sqrt{3\Gamma}x)} + \alpha_6\vec{v}_6 e^{(\sqrt{3\Gamma}x)} \tag{2.20}$$

By using boundary conditions the coefficients α_i can be found. On both ends every track has either a condition for the voltage or the derivative of the voltage given. Either the voltage is given $\hat{U}_N(0,\omega) = U$ or there is no current flowing through the boundary $\hat{I}_N(L,\omega) \propto \frac{\partial \hat{U}_N(L,\omega)}{\partial x} = 0$. For the situations where the current is taken as boundary, the derivative of equation 2.20 has to be used.

$$\frac{\partial \vec{\hat{U}}(x,\omega)}{\partial x} = 0 + \alpha_2\vec{v}_1 - \sqrt{\Gamma}\alpha_3\vec{v}_2 e^{(-\sqrt{\Gamma}x)} + \sqrt{\Gamma}\alpha_4\vec{v}_2 e^{(\sqrt{\Gamma}x)} - \sqrt{3\Gamma}\alpha_5\vec{v}_3 e^{(-\sqrt{3\Gamma}x)} + \sqrt{3\Gamma}\alpha_6\vec{v}_3 e^{(\sqrt{3\Gamma}x)} \tag{2.21}$$

Every track has its own equation and for every equation two boundary cases need to be solved to find all parameters. Solving these cases together yields all necessary coefficients. The equation 2.21 can be written into matrix form. For the geometry track 1 is the upper, 2 the middle and 3 the lower track. On the left of track 1 a voltage $U_{\mathrm{in}} = 1\,\mathrm{V}$ is applied and on the right of track 3 a ground is connected $U_{\mathrm{out}} = 0\,\mathrm{V}$, the currents are variables on these two boundaries. For all the other boundaries the current is taken to be 0 A (open boundaries) and the voltage is taken as variable.

The matrix form then becomes, with the upper row the equation for $\hat{U}_1(0,\omega)$ and the lower row for $\hat{U}_3(L,\omega)$:

$$\begin{bmatrix} 1 & 0 & -1 & -1 & 1 & 1 \\ 0 & 1 & \sqrt{\Gamma}e^{(-\sqrt{\Gamma}L)} & -\sqrt{\Gamma}e^{(\sqrt{\Gamma}L)} & -\sqrt{3\Gamma}e^{(-\sqrt{3\Gamma}L)} & \sqrt{3\Gamma}e^{(\sqrt{3\Gamma}L)} \\ 0 & 1 & 0 & 0 & 2\sqrt{3\Gamma} & -2\sqrt{3\Gamma} \\ 0 & 1 & 0 & 0 & 2\sqrt{3\Gamma}e^{(-\sqrt{3\Gamma}L)} & -2\sqrt{3\Gamma}e^{(\sqrt{3\Gamma}L)} \\ 0 & 1 & -\sqrt{\Gamma} & \sqrt{\Gamma} & -\sqrt{3\Gamma} & \sqrt{3\Gamma} \\ 1 & L & e^{(-\sqrt{\Gamma}L)} & e^{(\sqrt{\Gamma}L)} & e^{(-\sqrt{3\Gamma}L)} & e^{(\sqrt{3\Gamma}L)} \end{bmatrix} \begin{Bmatrix} \alpha_1 \\ \alpha_2 \\ \alpha_3 \\ \alpha_4 \\ \alpha_5 \\ \alpha_6 \end{Bmatrix} = \begin{Bmatrix} U_{\text{in}} \\ 0 \\ 0 \\ 0 \\ 0 \\ U_{\text{out}} \end{Bmatrix} \tag{2.22}$$

Taking the inverse of the matrix and multiplying it with the vector with boundary conditions yields the coefficients. The current can then be found from equation 2.5. The total impedance of the system can be found by dividing the voltage difference between both ends by the input current:

$$Z_{\text{total}} = \frac{\hat{U}_1(0,\omega) - \hat{U}_3(L,\omega)}{\hat{I}_1(0,\omega)} \tag{2.23}$$

The given example has been implemented in MATLAB and the result is shown in figure 2.8. The voltage source and ground indicate the connections, all other boundaries were given open ends as condition. Both the voltage and current are given at every position in the tracks in the upper two graphs of figure 2.8. The anisotropic nature of the printed structure becomes clear from the voltage and current density distribution plots.

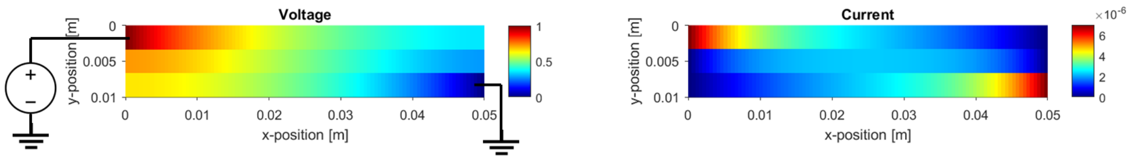

Figure 2.8: Example of the model of 3 parallel conductive tracks with open ends, showing the corresponding voltages (left) and currents (right). The voltage leads are indicated on the left. The voltage and current per traxel as plot can be found in figure 2.17

Matlab Implementation

The model has been implemented in Matlab for the general case. The model works for N-traxels where both the bulk and contact properties are included. For every boundary the condition can be given with an of 1,2 or 3 (respectively prescribed voltage, open end, meandering end). First the voltage everywhere is determined in the model, from which then the currents are derived via equation 2.21 in combination with equation 2.5. Besides the voltage and current, also the power dissipation is determined in the model (which can be used to determine the resistive heating). Figure 2.9 shows an example of the implemented model with the voltages, currents and power dissipation. The whole model is frequency dependent, where a sweep over prescribed frequencies can be performed to find the impedance as a function of frequencies.

2.2.2 Frequency behaviour

Γ is the key parameter of the system, determining the way the current flows through the samples. Current can flow via the shortest path (bulk conduction, the case where the contact properties dominate the conduction), flow following the traxels (traxel conduction, the case

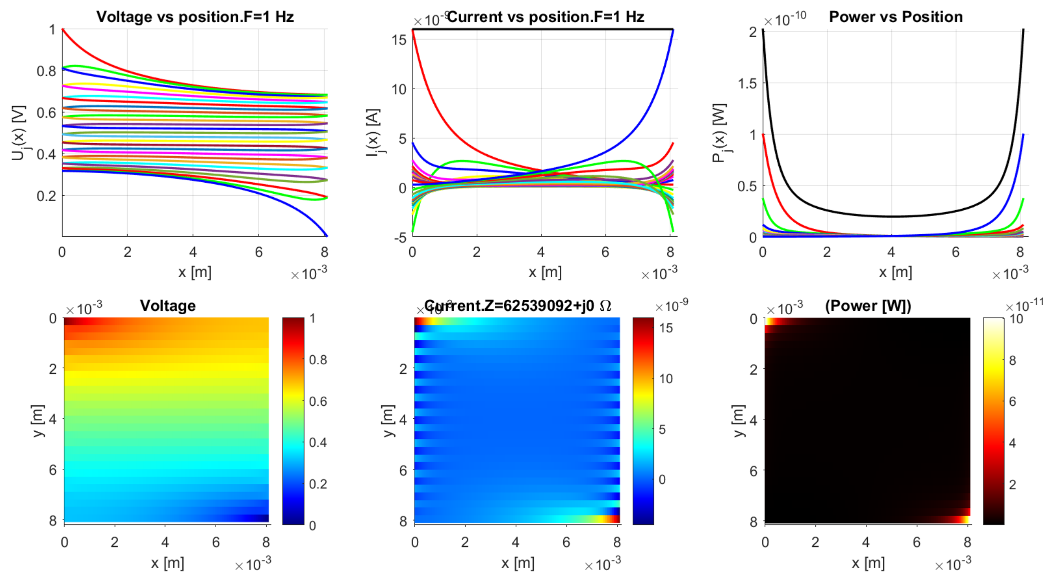

Figure 2.9: Example of the model showing 27 meandering, conductive tracks with the corresponding voltages and currents as well as the power due to horizontal currents.

where the bulk properties dominate the conduction) or somewhere in between (mixed conduction). By rewriting Γ in equation 2.9 the form can be obtained that gives more insight in the influence of the various parameters:

$$\Gamma = \frac{1}{W^2} \cdot \frac{1}{1 + \frac{\sigma}{\rho W} \left\{ \frac{1 + j\omega\rho\epsilon_0\epsilon_r}{1 + j\omega\sigma C_0} \right\}} \tag{2.24}$$

For low frequencies the purely resistive nature of Γ dominates and Γ can be approximated as follows:

$$\lim_{\omega \to 0} \Gamma(\omega) = \frac{1}{W^2} \cdot \frac{1}{1 + \frac{\sigma}{\rho W}} = \frac{1}{W} \cdot \frac{\rho}{\rho W + \sigma} \tag{2.25}$$

Therefore Γ gives a measure for how the horizontal bulk resistance relates to the combination of vertical bulk resistance and surface resistance, since the effect of the contact capacitance and permittivity are negligible at low frequencies. The value of Γ determines for the resistive case the conductive behaviour. If $\sigma \gg \rho W$, i.e. when Γ becomes small, there will only be traxel conduction. For $\sigma \ll \rho W$, i.e. when $\Gamma \approx W^{-2}$, current will take the shortest path crossing the traxels. When ρ_x and ρ_y are the same with the bulk conduction and there is no contact resistance, isotropic conduction takes place. In that case Γ is only determined by geometry (since a square anisotropic sample and an isotropic rectangular sample are scaled versions of each other):

$$\Gamma_{\text{isotropic}} = \frac{1}{W^2} \tag{2.26}$$

It is advised for future modelling to redefine Γ by taking out $\frac{1}{W^2}$, making Γ dimensionless. In this case the redefined $\Gamma^* = 1$ for isotropic conduction and the redefined PDE becomes:

$$\frac{\partial^2 \hat{U}_n(x,\omega)}{\partial x^2} + \Gamma^*(\omega) \frac{(\hat{U}_{n-1}(x,\omega) - 2\hat{U}_n(x,\omega) + \hat{U}_{n+1}(x,\omega))}{W^2} = 0 \tag{2.27}$$

When the traxel width W then becomes close to 0, the PDE would resolve into the Laplacian for homogeneous anisotropic materials as mentioned earlier:

$$\frac{\partial^2 \hat{U}(x,y,\omega)}{\partial x^2} + \Gamma^*(\omega) \frac{\partial^2 \hat{U}(x,y,\omega)}{\partial y^2} = 0 \tag{2.28}$$

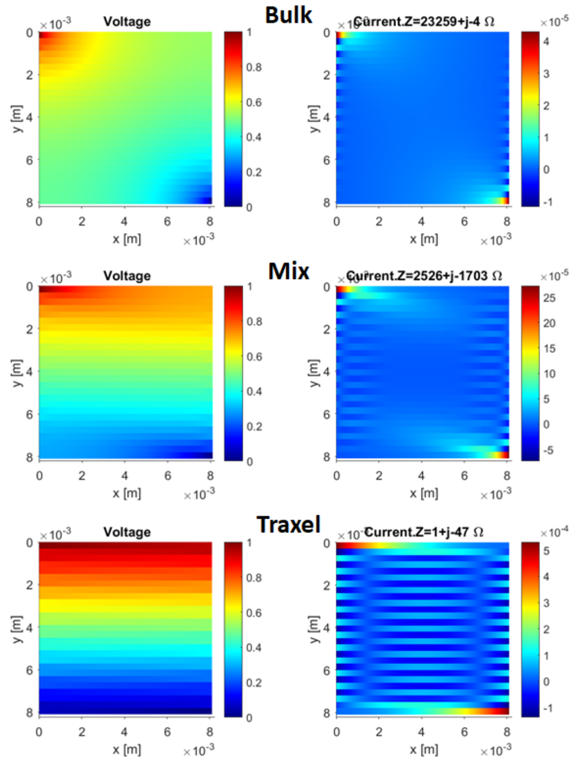

Figure 2.10: Voltage and horizontal Current plots for the three different conduction domains in a meandering sample, showing bulk conduction (voltage distribution over the entire bulk as well as current through entire bulk), mixed conduction (partly distributions through bulk and partly through traxels) and traxel conduction (voltage almost constant over a traxel and current mainly in traxel direction). The plots were created with the same parameters for different frequencies, the modes change due to the influence of the permittivity at higher frequencies.

A high frequency limit also exists for the current Γ. For high frequencies the capacitive effects become dominant instead of the resistive terms:

$$\lim_{\omega\to\infty}\Gamma(\omega) = \frac{1}{W^2}\cdot\frac{1}{1+\frac{1}{W}\left\{\frac{\epsilon_0\epsilon_r}{C_0}\right\}} = \frac{1}{W}\cdot\frac{C_0}{C_0W+\epsilon_0\epsilon_r} \tag{2.29}$$

For high frequency Γ hence gives the ratio of contact capacitance over the combination of bulk capacitance with vertical polarization. In case $\Gamma \approx 1$ the contact capacitance is dominant and bulk conduction occurs (again isotropic conduction occurs). In case $\Gamma \ll 1$ the bulk capacitance is dominant and traxel conduction occurs (since a higher capacitance yields lower total impedance). The three different conduction modes are shown in figure 2.10. The figure shows the voltage and current plots in the Matlab model for the three different conduction domains: bulk conduction (voltage distribution over the entire bulk as well as current through entire bulk), mixed conduction (partly distributions through bulk and partly through traxels) and traxel conduction (voltage almost constant over a traxel and current mainly in traxel direction). For the plots the same parameters have been used, where the rather high permittivity becomes significant for higher frequencies.

One other case can be imagined. If $\Gamma > 1$ than the voltage would drop from left to right instead of from top to bottom like in the lower left graph in figure 2.10. This is however physically impossible for the passive, isotropic system in the case of isotropic material properties ($\rho_x = \rho_y$ and $\epsilon_x = \epsilon_y$), since it would require either σ, C_0 or ϵ in equation **??** to be negative (it can occur for anisotropic properties). The conduction modes can be tweaked further by also having anisotropic resistivity and permittivity in the bulk itself. This can for example be done by including

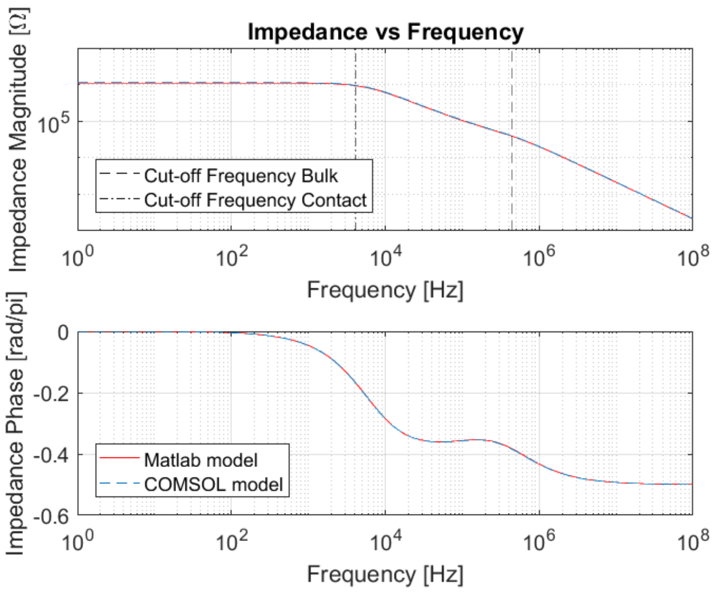

Figure 2.11: Modelled impedance magnitude and phase for a print with 27 traxels with meandering boundaries and voltage leads on the opposite corners. The two vertical lines in the upper graph indicate the theoretical cut-off frequencies, whereas both graphs show the Matlab model result and the FEM result (section 2.3).

conductive particles with high aspect ratio (e.g. carbon fibers). This would yield the following description of Γ, with in the left fraction the horizontal bulk properties and in the right fraction the contact and vertical bulk properties:

$$\Gamma = \frac{\rho_x}{W(1 + j\omega\rho_x\epsilon_x)} \frac{(1 + j\omega\rho_y\epsilon_y)(1 + j\omega\sigma C_0)}{(\rho_y W + \sigma + j\omega\rho_y\sigma W C_0 + j\omega\rho_y\sigma\epsilon_y)} \tag{2.30}$$

The three conduction domains recognized in Γ can be related to the cut-off frequencies of the sample. In case the contact and bulk parameters are of another order of magnitude one of the two is dominant at a certain frequency and can be treated as a single RC-model per mode with a cut-off frequency. The cut-off frequency for an RC-circuit is given by $f_{\text{cut-off}} = \frac{1}{2\pi RC}$. For the contact mode the cut-off frequency tells us at which frequency the contact capacitance will be the dominant factor in the contact impedance:

$$f_{\text{cut-off, contact}} = \frac{1}{2\pi R_{\text{contact}} C_{\text{contact}}} = \frac{1}{2\pi\frac{\sigma}{A} C_0 A} = \frac{1}{2\pi\sigma C_0} \tag{2.31}$$

For the bulk mode the cut-off frequency tells us at which frequency the permitivity will be the dominant factor in the bulk impedance:

$$f_{\text{cut-off, bulk}} = \frac{1}{2\pi R_{\text{bulk}} C_{\text{bulk}}} = \frac{1}{2\pi\frac{\rho L}{A}\frac{\epsilon A}{L}} = \frac{1}{2\pi\rho\epsilon} \tag{2.32}$$

These cut-off frequencies can be used to indicate the transitions between the different conduction modes. In the impedance plot of an arbitrary sample (with 27 traxels and voltage leads on the opposite corners) one can clearly recognize the cut-off frequencies in the magnitude and phase plot in figure 2.11.

The impedance magnitude graph shows three areas with a distinct slope, which are the traxel conduction; mixed conduction and bulk conduction respectively. This also becomes clearer when studying the frequency dependence of Γ (or more precisely, the dimensionless form

$\sqrt{\Gamma}W$). The parameter Γ is not dimensionless, it has the unit m^{-2}. For obtaining a dimensionless expression, the length of the system should also be taken into account. Therefore $\sqrt{\Gamma}W$ is a better parameter for studying the system behaviour, like a dimensionless eigenvalue (or ΓW^2 when a more linear scaling in line with equation 2.26 is desired). In case the parameter can be controlled through the printing parameters, it could for example be used for improving sensor performance. It is therefore interesting to study this parameter more closely. Different conduction modes can be recognized in the value of $\sqrt{\Gamma}W$. For low frequencies the conduction is purely resistive, then mixed and then purely capacitive at high frequencies, as shown in figure 2.12 (where the horizontal lines indicate the DC, AC and isotropic case for $\sqrt{\Gamma}W$ and the vertical lines the cut-off frequencies).

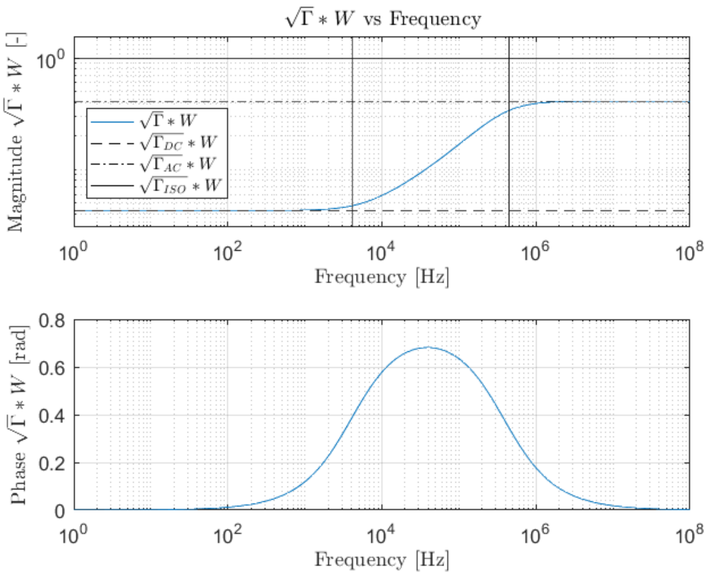

Figure 2.12: Modelled Γ as a function of frequency for a meandering sample. The vertical lines indicate the theoretical cut-off frequencies and the flat horizontal lines show the low and high frequency approximations of Γ (respectively being $\sqrt{\frac{1/\sigma}{W*1/\rho}} * W$ and $\sqrt{\frac{C0}{W*\epsilon}} * W$) as well as the isotropic limit.

In figure 2.12 the theoretical cut-off frequencies (from equation 2.31 and 2.32) clearly mark the transitions between the different conduction modes. The low frequency mode is in this case traxel conduction and the high frequency mode is bulk conduction. The mixed conduction mode can be recognized by a smooth transition of Γ between both other both modes.

A simple circuit approximation with an RC model was made to fit the total impedance of the model. This model is shown in figure 2.13.

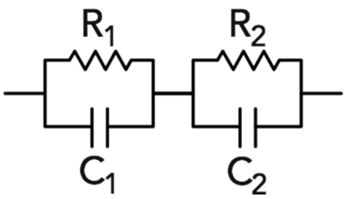

Figure 2.13: Equivalent circuit RC-model used for fitting the electrical properties of the 3D-printing conduction model. R_1 and C_1 mimick the bulk properties and R_2 and C_2 mimick the contact properties.

The total impedance of the model can then be represented by:

$$Z_{\text{RC-fit}} = \frac{R_1}{1+\omega^2\rho^2\epsilon^2} + \frac{R_2}{1+\omega^2\sigma^2 C_0^2} = \frac{R_{\text{bulk}}}{1+f^2/f^2_{\text{cut-off,bulk}}} + \frac{R_{\text{contact}}}{1+f^2/f^2_{\text{cut-off,contact}}} \tag{2.33}$$

The two resistances could be fitted on the low frequency impedance of the Matlab model. It was shown that the conduction modes for low and high frequencies can be fitted properly with an RC-circuit with the theoretical cut-off frequencies, however the mixed conduction could not be recreated. This is due to the fact that in the mixed conduction mode, the bulk and contact conduction are not just in a series network (there is interaction between both).

2.3 Numerical Simulations

Numerical simulations can be used to verify the analytical model. Next to this they can be used to simulate more complex structures and coupled physics to compare to experiments (bridging the gap between the analytical model and the experiments), like including the shapes of printed tracks as done by (11) for conductive ABS. The simulations will be done with the Finite Element Method in the COMSOL software. The multiphysics options in COMSOL provides additional opportunities, like including Joule heating in the model to compare simulations to thermal imaging experiments.

COMSOL Implementation

The physical model has been implemented in COMSOL version 4.3. A geometry was made of rectangles and semicircles to represent the traxels and bends. The material properties were taken similar to those in the analytical model, for most results in this chapter the parameters are given in table 2.1. For the simulations the Electric Currents (ec) physics module is used, including terminals and contact impedances. The mesh size was based on the default for physics module, where an example is shown in figure 2.14 (showing a higher element concentration in the bends). A frequency domain study was performed to determine the electrical properties as function of frequency (like in equation 2.13). The impedance between the voltage leads was simulated, as well as the local voltage and current density everywhere. This data can be used for comparison to calculate the error between the Matlab model and FEM simulations. Several differences exist between the Matlab model and the COMSOL simulations. In COMSOL 2D-conduction and polarization is present inside the traxels (whereas in Matlab the vertical conduction and polarization through bulk are located together in the contacts). Furthermore the COMSOL model also includes the meandering bends, making it more realistic.

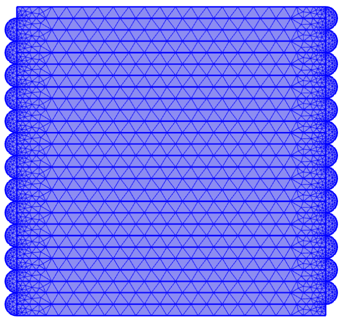

Figure 2.14: Default mesh as applied to a square 3D-print used for a COMSOL simulation (e.g. 3704 elements).

To verify the COMSOL simulations a mesh study was performed on an example in COMSOL. The results of this are shown in figure 2.15, where the relative error of the impedance magnitude and absolute error of the impedance phase with the result from the finest mesh in COMSOL is shown at the frequencies 1 Hz and 1 MHz. The mesh study showed that already the coarsest mesh has a reasonable result (below 0.5 %), whereas finer meshes give even better results. The errors in impedance are for the used default mesh settings (3704 elements) generally below 0.1 %.

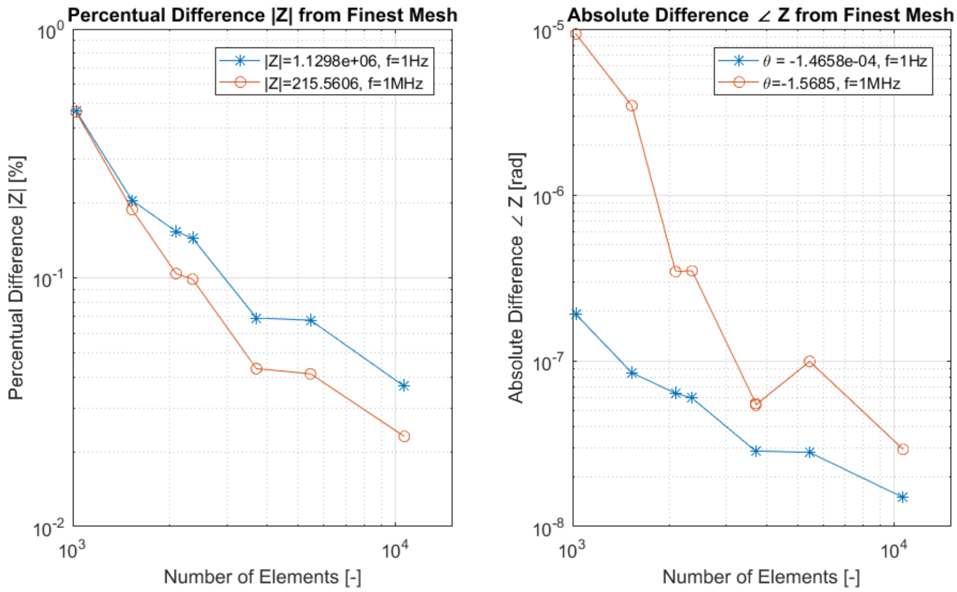

Figure 2.15: Mesh Convergence Study of the magnitude and phase of the impedance for different meshes as compared to the finest possible mesh.

Parameter	Value	Unit
Resistivity ρ	0.4	$\Omega\,\mathrm{m}$
Relative Permittivity ϵ_r	1×10^5	-
Contact Resistivity σ	6.5×10^{-2}	$\Omega\,\mathrm{m}^2$
Contact Capacitance C_0	6×10^{-4}	$\mathrm{F\,m}^{-2}$
Number of Traxels N	27	-
Traxel Length L	$1, 8.1, 65.61$	mm
Traxel Width W	0.3	mm
Traxel Height H	0.1	mm

Table 2.1: Parameters as used for the Models and Simulations in this chapter, except specified otherwise.

2.4 Model Verification

To verify the model, model results and FEM results are compared. Figure 2.11 shows the impedance as calculated with the model and with COMSOL. The sample in this case has traxels of 8.1 mm long (a square sample). The comparison shows a good fit with small deviations for higher frequencies. A similar verification has been done by means of an equivalent circuit in LTspice, this showed the same values albeit with a bigger error due to the rough discretization.

The error between the modelled impedance and the FEM simulation results is shown in figure 2.16. In the shape of the error curve the three conduction domains can be recognized. The biggest error occurs in the traxel conduction. A possible explanation for this is the lack of the bends in the analytical model, which has less influence in case of the bulk conduction.

Next to a comparison of the global properties, the solution also needs to be verified locally. For this the voltages and currents in the traxels can be considered. Figure 2.17 plots a comparison of the DC-case with voltages and currents in all the traxels for the example from section 2.2.1, showing good correspondence (in this particular case an error of around 0.01 %).

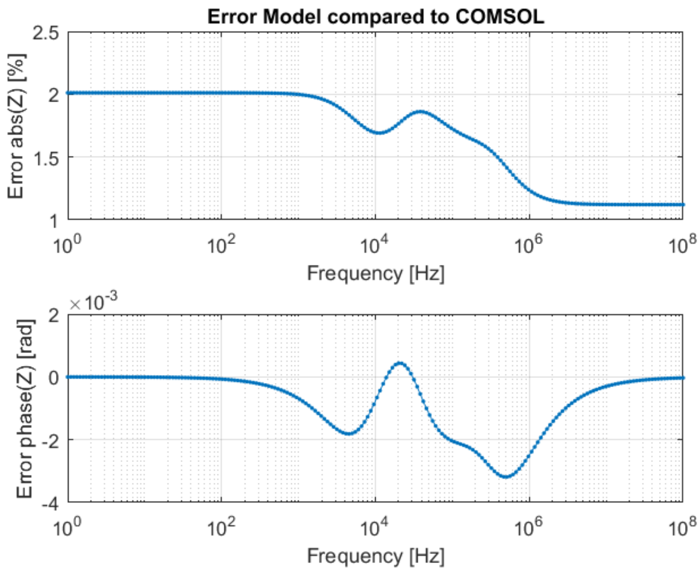

Figure 2.16: The impedance error of the model of a meandering sample as compared to COMSOL, showing a similar shape as Γ in figure 2.12.

For AC also the voltages and current can be compared, of which a comparison of the voltage at 1 MHz in the lowest traxel is shown in figure 2.18. From this comparison can be seen that for this high frequency the real part of the voltage phasor has an error of at most 0.12 % and the imaginary part of the voltage phasor an error of at most 6.4 %. This is significantly higher than for the DC case in figure 2.17. The biggest errors occur at the side next to a bend. Especially the phase seems to be affected by this. In COMSOL most of the current flows through the bend, close to the contact, whereas in the model this behaviour is not present due to the lack of a 2D-bend.

Besides the frequencies, different aspect ratios also indicate that a case with more 2D and bend effects yields bigger errors. If a sample has a high aspect ratio (in this case defined as width/height, so $\frac{L}{N*W}$), less vertical current flows through the bulk since there is relatively less 2D-conduction. Figure 2.19 shows the errors in magnitude and phase of the impedance, showing both an increase of the maximum errors with an increasing aspect ratio and with a decreasing frequency.

These short checks only verify up to a certain extent that the model works as it should compared to the finite element software. For a proper verification the Root Mean Squared Error (RMSE) should be used, comparing the outcomes from the model and FEM simulations everywhere, instead of just at a few positions. The relative RMSE would be calculated as follows and it is proposed to use it in future studies (it has not been implemented since special care has to be taken in combining the Matlab and COMSOL data correctly):

$$\sqrt{\frac{\sum_{i=1}^{M}\sum_{j=1}^{N}\left(U_{i,j}^{\text{Model}} - U_{i,j}^{\text{FEM}}\right)^2}{MN}} \tag{2.34}$$

The problem of lack of bends has already been mentioned shortly, however this is not the only limitation of the analytical model. These things can possibly be improved in future research. The main limitations of the analytical model are as follows:

- 2-Dimensional Conduction and Polarization

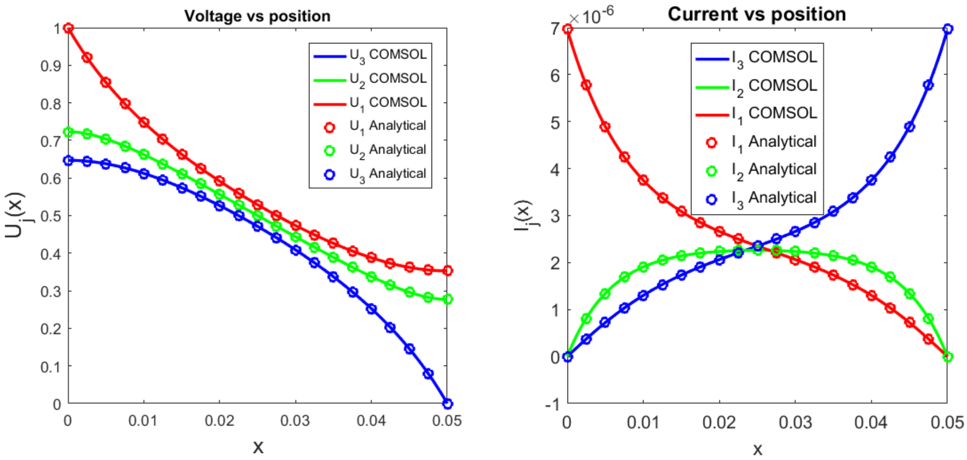

Figure 2.17: Comparison of the DC voltage and current in the traxels of the example of figure 2.8 compared to COMSOL showing similar results. A sample with open ends and opposite connections has been used, like in figure 2.8.

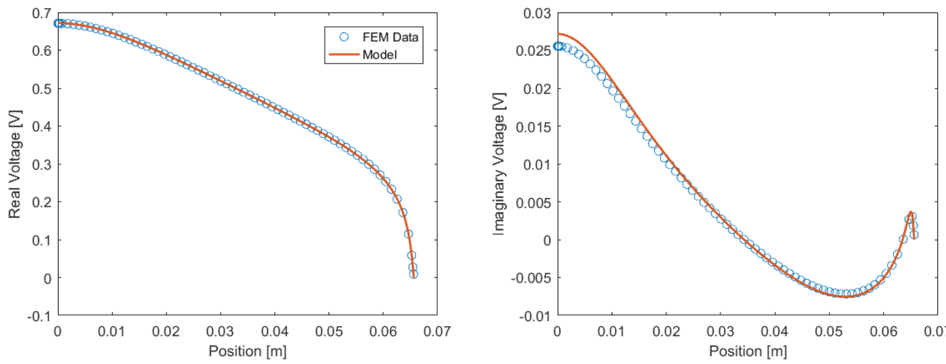

Figure 2.18: The real and imaginary voltage in the lowest traxel of a meandering sample, as modelled and simulated at 1 MHz with the parameters from table 2.1 (a traxel length of 65.61 mm at 1 MHz).

2-Dimensional Conduction and Polarization are limited, since the vertical currents and polarization from the bulk are represented in the contacts. This has as a result that for samples with few traxels model results become less accurate

- Simplified geometry

  The model uses a simplified geometry, where bends are not included as part of the current path. For structures with a relatively large portion of bends, this can affect the model outcomes. This seems to be the main error, since the errors from samples with open ends is smaller than for meandering samples (a result for open ends is shown in figure 2.17).
- Lacking multi-physics effects

  The model only considers the electrical domain. Joule heating however heats the sample, possibly yielding a significant change in conductivity for higher currents.
- 3D-functionality

  For now there is only a 2D-implementation of the model, with only in-plane currents. A 3D implementation is expected to also be possible, with several layers of traxels on top of each other.

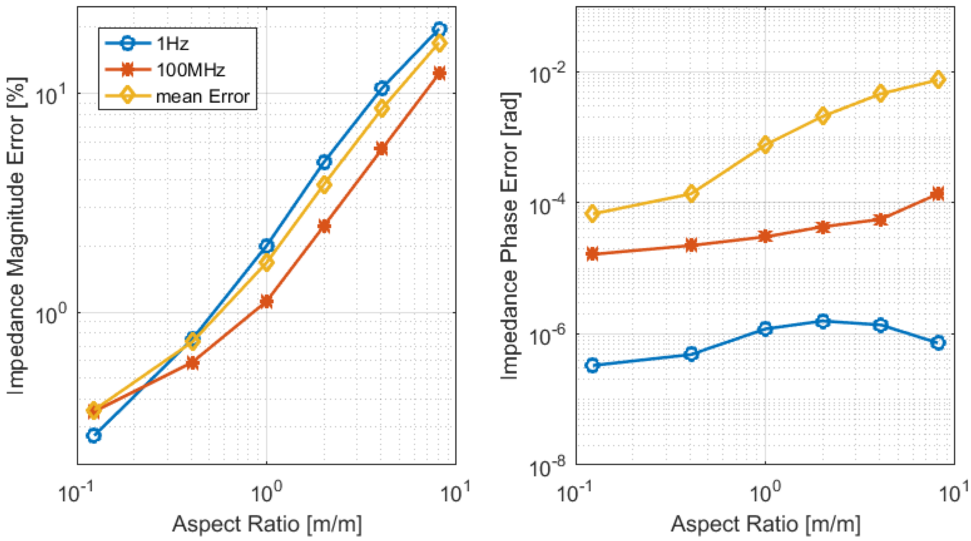

Figure 2.19: The error of the impedance in COMSOL as a function of the aspect ratio (length over height) for a meandering sample, showing a larger error for samples with shorter traxels. The mean phase error is bigger than the two shown errors, since the main phase error occurs in the mixed conduction region.

2.5 Conclusion

To model the anisotropic electrical properties of 3D-prints a partial differential equation has been derived based on the combination of bulk and contact properties in and between traxels. An eigenvalue expansion method has been used to solve the model and to calculate the voltages and currents. With the model it could be shown that three possible different conduction modes exist depending on the relative importance of the contact impedance: conduction through the traxels, through the bulk and a mix of both. The dimensionless form of Γ can be used to identify the conduction mode. A Finite Element Software package has been used to verify this model, where a mesh convergence study was performed to check the trustworthiness of the FEM simulations. Small deviations occur between the model and the FEM results due to assumptions and simplifications in the model, but overall both correspond well. The main differences occur due to the simplified meandering bends in the model. Furthermore it was shown that the error becomes bigger for larger aspect ratios of the traxels and for lower frequencies. Finally a validation step of the model is still necessary to validate the assumptions in the physical model.

3 Materials and Global Characterization

The aim of this chapter is to introduce the reader to the current use and theory of conductive polymer composites (specifically carbon black-polymer composites), combined with the default electrical characterization method. Finally measurements on the chosen material and samples are presented for illustration purposes.

3.1 Related Work

3D printing of conductors, and in particular of transducers, by means of Fused Deposition Modelling (FDM) is an upcoming research area (1). Conductive Polymer Composites (CPC) have been researched intensively for smart structure applications in electromagnetic shielding, electrostatic charge dissipation, electronic switches, self regulating heaters and sensors (40). The conductive materials for 3D printing mainly comprise metal, carbon, and their polymer composites. Their advantages include excellent flexibility, low weight, high environmental stability and safety as well as low manufacturing cost (40). Since CPC's are often thermoplastic, they can be handled by FDM (11). Especially polymer composites mixed with the various forms of carbon have attracted considerable attention. Carbon cannot be oxidized and as a result of that become non-conductive. Furthermore carbon-based CPC's typically do not need additional processing steps after printing such as thermal annealing or evaporation of solvent and they have significantly longer shelf life than that of metallic ink (3). The following paragraph gives several examples from research as well as commercially available products.

Researched materials for 3D-printable CPC's mainly focuses around carbon black (CB) (11; 4; 40; 3), carbon nanotubes (CNT) (41; 5; 42) and graphene platelets (5; 43) fillers with different types of polymers and elastomers. These studies have mainly focused on developing the materials, showing suitability for FDM printing and showcasing them with different sensor designs. From these studies it becomes clear that using these materials for 3D-printing is rather new, and no benchmarks, rules or non-research applications exist yet. A first improvement in that sense is the commercial availability of 3D-printable CPC's. Important examples on the market are Black magic 3D (44), Protopasta (9) and PI-eTPU85-700+ (8). Several comparative studies have been performed with these materials (14; 10) and the first examples of printed transducers exist (mainly capacitive and strain sensors, like the whisker sensor in figure 1.2a) (2; 45; 46; 15; 47). In this research the material PI-eTPU85-700+ will be used, for its flexibility and relatively low resistivity.

PI-eTPU85-700+ has been studied before by Schouten, and he found for his measurements an electrical resistivity of $7.43\,\Omega\,\mathrm{m}$ and a relative permittivity of 176 (48). It has to be taken into account that the material is made per batch and large differences in specifications can exist between batches. So far different sensors have been made with PI-eTPU85-700+: a flexible capacitive force sensors (49; 13), flexible soft EMG electrodes as shown in figure 1.2b (16) and displacement sensors (50). This shows the suitability of the material for FDM-printed transducer purposes. Next a clear view on the electrical properties of the material is necessary.

3.2 Material Properties

3.2.1 Carbon Black Networks

Carbon Black (CB) is an amorphous form of carbon, produced from the incomplete combustion of heavy petroleum products. As such it is a readily available and inexpensive (4). Most carbon black grades have an electrical volume resistivity in the range of $0.001\,\Omega\,\mathrm{m}$ to $1\,\Omega\,\mathrm{m}$, which is in the range of semiconductors (51). When used for adding electrical conductivity to polymers, CB exhibits a phenomenon known as percolation. As the loading of the carbon black

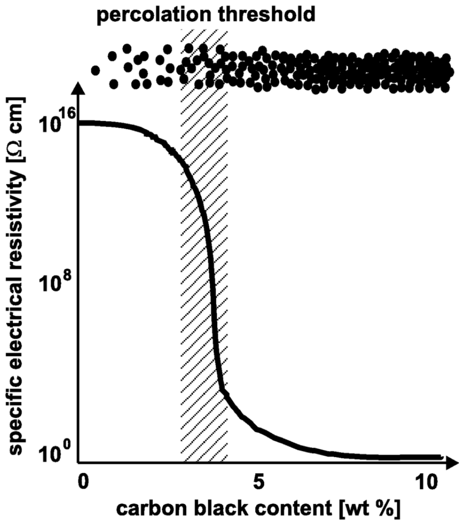

Figure 3.1: Qualitative dependence of the electrical resistivity on carbon black content. The hatched part is called the percolation threshold (54).

in the compound increases, initially the plastic compound remains insulating. With percolation the concentration of carbon black is sufficient to cause a sharp and abrupt rise in electrical conductivity. The narrow threshold range is known as the percolation threshold. Figure 3.1 illustrates this qualitatively, showing a high resistivity for low CB concentrations, followed by a steep drop around the percolation threshold and finally giving rise to low resistivity for high CB loading. At this concentration the conducting primary aggregates connect to each other and form a conducting network, facilitating the electronic conduction through the polymer-filler composite (51). The electrical percolation threshold is strongly related to the nature as well as to the aspect ratio of the filler (52). The percolation threshold generally decreases with increasing filler aspect ratio, therefore a lot of research is done on large aspect ratio and multifunctional conductive fillers, such as carbon nanotubes (CNTs) and graphene nanoplatelets (53).

3.2.2 Conduction

For the conduction effects in carbon-based networks it is widely thought that the quantum mechanical junction tunneling is responsible (55; 53). Tunneling is a quantum mechanical process in which the wave function of the electron has a small tail extending beyond the potential barrier, making it possible for the electrons to flow through the insulating polymer between particles (56). Conduction through direct physical contact of particles without the influence of the polymer only occurs for particles bigger than 300 nm (51). For smaller CB particles the polymer influences the conductivity (51).

Carbon black particles included in polymers gives rise to complex dielectric behaviour with different types of (polar) losses (57). The Maxwell-Wagner model studies the effect of conductive particles in a dielectric medium, however this model does not take into account the quantum tunneling, and changes in characteristic frequency upon mechanical deformation (57). By modelling the CB-polymer composite as a series of micro-resistors and micro-capacitors, this can be taken into account (57; 58; 59). Figure 3.2 (a) shows such a microcapacitor schematically with the corresponding tunneling barrier.

If one simplifies the junction as being two parallel circular plates with area A and gap δ the classical resistance and capacitance become:

$$R = \frac{\rho\delta}{A} \text{ and } C = \frac{\epsilon A}{\delta} \tag{3.1}$$

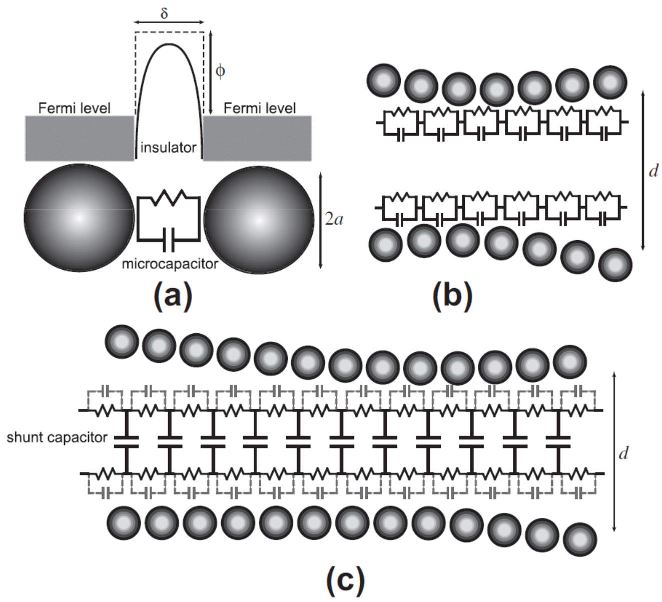

Figure 3.2: Models for electrical conduction in carbon black networks: a. the microcapacitor model describing the junction between CB particles, b. the series microcapacitor percolation path and c. the transmission line network (55).

This yields for the cut-off frequency of a parallel RC-circuit: $f_{\text{cut-off}} = \frac{1}{2\pi\rho\epsilon}$. Because the gap size is taken constant and tunneling is not taken into account in this equation, the cut-off frequency becomes a fixed value. By including the tunneling current density across a junction, a dependency on the gap size can be derived for the cut-off frequency (57; 58). When taking typical barrier value and particle diameter in this model, gap sizes of 2 nm to 5 nm have been predicted (58). Since in this research no mechanical interaction is taken into account (hence a fixed gap size), a constant resistivity ρ and permittivity ϵ are assumed for the material and equation 3.1 can be used. In this way a sample if represented as if it consists of a series microcapacitor percolation path, as shown in figure 3.2 (b). When modelling a geometry with length L and cross-sectional area A this yields a cut-off frequency of $f_{\text{cut-off}} = \frac{1}{2\pi\rho\epsilon}$ and an impedance magnitude only depending on geometry and material constants:

$$|Z| = \frac{R}{\sqrt{1+\omega RC}} = \frac{\rho L}{A\sqrt{1+\omega\rho\epsilon_0\epsilon_\mathrm{r}}} = \frac{\rho L}{A\sqrt{1+f/f_{\text{cut-off}}}} \tag{3.2}$$

Furthermore the impedance phase also solely depends on material constants:

$$\angle Z = -\arctan(\omega RC) = -\arctan(\omega\rho\epsilon_0\epsilon_\mathrm{r}) = -\arctan(f/f_{\text{cut-off}}) \tag{3.3}$$

The microcapacitor model can be used to model these materials, however it has one drawback. Values of the relative permittivity for CB CPC's measured in literature go up to and even above $1e4$ (60; 58; 55; 61). The junction area has to be unrealistically high to account for such values (when considering a typical junction area, the resulting permittivity would typically be hundreds of times lower than found in literature) (55). The estimations of the gap width from the cut-off frequency are not affected by this, since the frequency is independent of A. Shin et al propose a solution by means of modelling the capacitance effects as microcapacitor transmission lines, as shown in figure 3.2 (c) (55). This model seems to be able to capture the high permittivity values and explains them in a physical way, at low frequencies the conduction is mainly along the backbone pathways, however at high frequencies the entangled nature plays a major role. The mathematics of the model correspond to that of the electrochemical diffusion process or Warburg impedance, which corresponds to the successful use of a Warburg

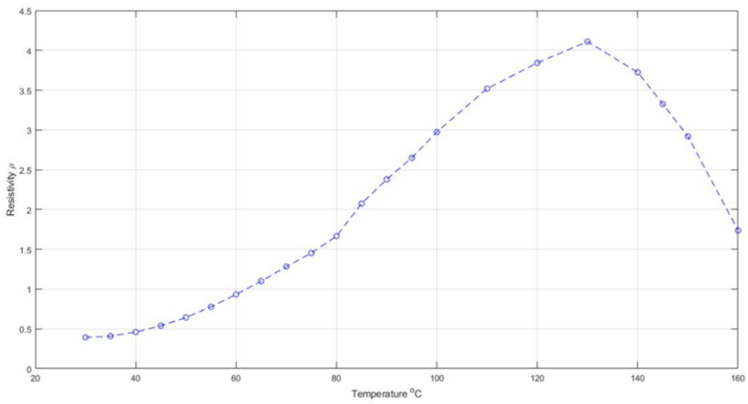

Figure 3.3: Temperature-dependence of the resistivity of a PI-eTPU85-700+ filament sample, showing the PTC behaviour below and NTC behaviour above a phase-transition temperature (adapted from the MSc thesis work of A. Umrani).

element in fitting the PI-eTPU85-700+ impedance data by Dias (38). Although the transmission line model shows promising results, for this research the simpler microcapacitor model will be used, since it serves all the needs and its shortcomings are of no influence for this research. So far the resistivity and permittivity have been treated as constants, however both parameters are temperature dependent.

3.2.3 Pyroresistive Behaviour

CPC's can also show interesting pyroresistive behaviour. Pyroresistivity either yields an increase in electrical resistivity with increasing temperature, known as the positive temperature coefficient (PTC) effect, or a decrease in electrical resistivity, known as the negative temperature coefficient (NTC) effect. CPC's can have large positive temperature coefficient (PTC) effects, which have found applications in self-regulative heaters and over-current protectors (62; 63). The general accepted explanation for the PTC effect is believed to be a mismatch of thermal expansion coefficient between polymer and filler, together with melting of the polymer matrix. Because of the significant volume expansion at the melting temperature, the gaps between the conductive particles increases [246,257]. However the cause of the resistance change is not fully clear, being explained in different ways (in terms of percolation behaviour, void formation, interfacial polarisation, tunnelling current, or potential tunnel barrier height) (62). It has been demonstrated that the PTC effect increases with increasing filler size and with decreasing filler content, both for spherical and platelet-like conductive fillers (62; 63). The negative temperature coefficient (NTC) effect on the other hand is assumed to be caused by the decrease of the elastic modulus of the polymer matrix at the melting point, facilitating the reconnecting of the conductive particles and therefore the repair of disconnected conductive pathways (64; 65). Hence the interpretation of the PTC and NTC effect is still not fully clear, but the effects are clearly there. Figure 3.3 shows a measurement on the resistivity of a PI-eTPU85-700+ sample. The PTC effect is present until a certain temperature after which the NTC effect sets in. For temperatures just around room temperature no large deviations occur for the resistivity, legitimizing the use of a fixed resistivity for the models. In case no heating occurs CPC's are ohmic of behaviour, showing linear current-voltage curves. So for low voltages and for short voltage pulses linear IV-curves have been shown (and hence the absence of Schottky barriers (66)) (67; 68; 66; 59).

For more theory on the conduction in carbon black the author would like to refer the readers to the mentioned literature. In literature mainly dielectric impedance spectroscopy was used to measure the impedance to research the discussed electrical properties.

3.3 Electrical Measurements

Several measurements have been done to determine the material properties as presented in the previous section. These measurements consist of SEM imaging and dielectric impedance spectroscopy, which are the main measurement methods for (electrically) characterizing CB-polymer composites and printed sensors in literature (e.g. (11; 58; 15)).

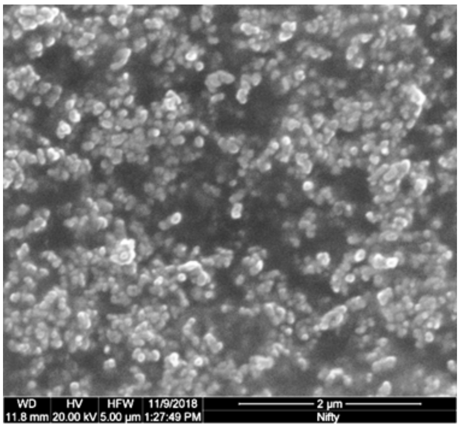

Figure 3.4: Scanning Electron Microscopy image of the Carbon Black distribution in unprinted filament, showing CB particles and aggregates. The sample is prepared by cryo-fracturing.

3.3.1 SEM Imaging

The volume percentage and micro-dispersion of the CB particles in PI-eTPU85-700+ are unknown. To study the material at a micro scale, samples were prepared by cryo-fracturing (freezing them far below the glass transition temperature with liquid nitrogen to make them brittle and then smashing them to pieces). By SEM imaging a rather homogeneous distribution of particles of around 100 nm is found in the samples. A good estimate of the volume percentage can not be given based on the SEM images, since SEM's in general have a large depth of field and the structure has quite some roughness (resulting in imaging of particles at different depths). For the estimated gap size in literature of 5 nm, the gaps in figure 3.4 should roughly be 0.4 pixels wide (the 2 μm scale is 150 pixels wide). From figure 3.4 this seems an acceptable estimate.

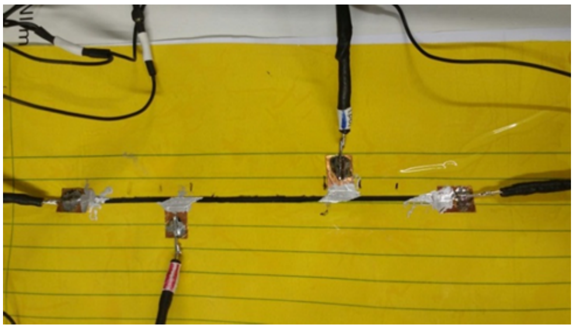

Figure 3.5: A dielectric impedance spectroscopy sample with copper tape and silver ink contacts.

3.3.2 Dielectric Impedance Spectroscopy

The method used in literature for measuring the impedance and determining resistivity and permittivity is done by using dielectric impedance spectroscopy (57; 58; 55). With this method generally the impedance magnitude and phase are measured, for which the theoretical values are given in equations 3.2 and 3.3 respectively. By using the parallel RC nature of the material

($Z = \frac{R}{1+j\omega RC}$), the resistance and capacitance can be derived from these measurements in the following way:

$$R = \frac{|Z|}{\cos(\angle Z)} \text{ and } C = -\frac{\sin(\angle Z)}{\omega |Z|} \tag{3.4}$$

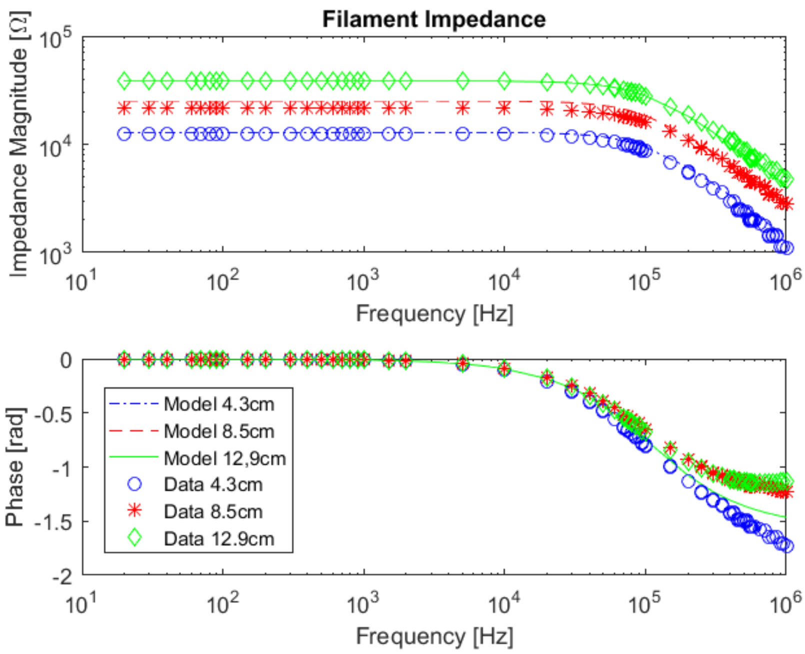

Figure 3.6: LCR-measurements of different filament lengths, showing identical cut-off frequencies. The dots show experimental values and the solid lines show the RC-model.

Subsequently the resistivity and permittivity can be determined with equation 3.1 in case the geometry is known (and is a beam with a fixed cross section). An advantage of this method is that the experimental data can easily be compared to the modelling results from equation 2.23. Samples are made by taking pieces of filament and taping them to a kapton sheet. Contacts are made to the filament by means of pieces of copper tape stuck to the kapton and connecting to the filament with silver ink (Electrolube (69)). 4-point measurements are performed to reduce contact issues and parasitics of the cables. This set-up can be seen in figure 3.5. The impedance measurements are performed with an LCR meter (the HP 4284A) with a small signal to prevent heating (to prevent nonlinear effects). The impedance magnitude drops several orders of magnitude for higher frequencies causing the LCR autorange to switch between measurement ranges, resulting in hysteresis-like measurements. Therefore a fixed range resistor was set for the LCR (around the magnitude of the DC resistance of the sample). A limitation of this is the limited range of frequencies over which can be measured with a certain range resistor of the LCR meter, giving incorrect results at the outer frequencies for which in a certain range can be measured (70). Measurements were done for filament samples with different lengths. The results are shown in figure 3.6 and are fitted with the RC-model from equation 3.2 and 3.3. It becomes clear that the samples all have the same cut-off frequency, which is in correspondence with the RC-model in which the cut-off frequency only depends on material properties. For higher frequencies ($> 10 \times 10^5$ Hz) the phase starts to deviate, this might be caused by the difficulty to also measure at the higher frequencies with the fixed impedance range. The LCR measurements where performed over the frequency range from 20 Hz to 1×10^6 Hz and back. In this sweep drift of only a few tenths of a percent where found, indicating little drift in the measurements.

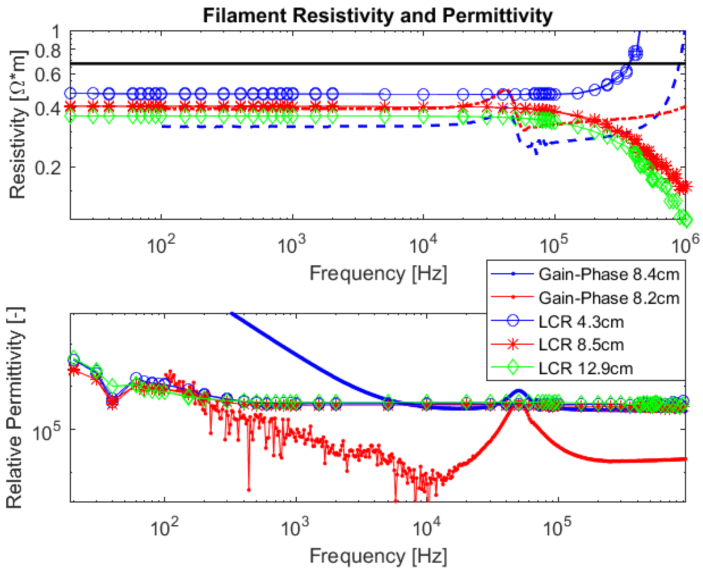

Figure 3.7: Resistivity and permittivity as measured with the LCR (from the data in figure 3.6) and with a gain-phase analyzer.

Measurements are also done with a gain-phase analyzer (HP 4194A) as a reference, because of the possible LCR range errors. Within the frequency range of 2×10^1 Hz to 1×10^5 Hz the resistivity values are very close, and within a range of 1×10^4 Hz to 1×10^6 Hz the relative permittivity values coincide. Hence only for a small range the measurements of both devices coincide. For low frequencies and high frequencies the gain-phase measurements deviate significantly. The values for the resistivity and relative permittivity are derived by means of formula 3.1 in combination with the measured sample geometries. Figure 3.7 shows the derived values over the entire measured frequency range for both the LCR and gain-phase meter. The values have also been derived from a least squares fitting of a parallel RC-circuit to the LCR data. These values are plotted as the horizontal lines in figure 3.7. With a least squares fit of a parallel RC-circuit to the LCR data a resistivity of $0.670\,\Omega$m and a relative permittivity of 2.472×10^5 were found (used in figure 3.6). The values found from the data however are approximately $0.4\,\Omega$m and 4×10^5. A sample of multiple bundled filaments (11 segments) also showed a resistivity of $0.4\,\Omega$m and a relative permittivity of 8×10^4. The determined values differ significantly from the RC-fit values. This could have different causes, for example deviations from a perfect RC-model and difficulty of the LCR to measure the full frequency range with a one fixed resistance range. Interesting to note is that the both methods do yield the same cut-off frequency. The residuals from the lsq-fit are shown in figure 3.8, indicating that indeed a significant deviation from the RC-model occurs.

To check the validity of the LCR data, the lin-KK tool can be used. This is a tool from the field of Electrochemical Impedance Spectroscopy (EIS), a method for materials research which uses impedance measurements and fits standard circuits to them (like done in this case with a parallel RC-circuit). The tool is based on the Kramers-Krönig transform, which give a relation between the real and the imaginary impedance of the sample for a causal, linear, stable and finite system. The tool uses multiple RC circuits in series to solve the transform (to fit all relevant time constants) and determines the number of linked circuits based on a set of rules. More theory on this can be found in (71; 72; 73), and the tool is distributed by (74). Figure 3.9 presents the residuals from the Lin-KK check with LCR data from the sample of 8.5 cm long from figure 3.7, showing significant errors above frequencies of 2×10^5 Hz and showing some minor drift in

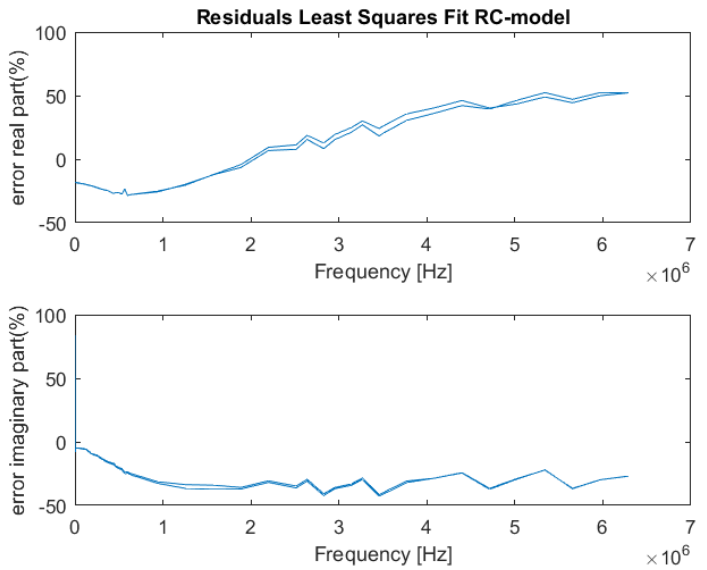

Figure 3.8: Residuals found from the least squares fit of the impedance to a parallel RC-model.

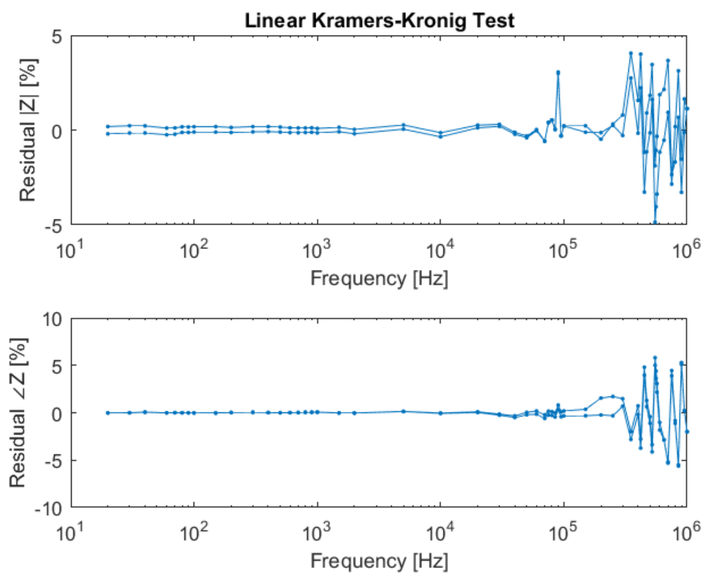

Figure 3.9: Residuals for the Linear Kramers-Krönig validity test. Drift in the low-frequency real part of the impedance and major devations at high-frequencies can be recognized.

the low-frequency real impedance. Multiple RC-circuits were used for the check, showing that one RC-circuit is indeed insufficient to represent the data.

Rather high values (and possibly inaccurate) for the relative permittivity are found. Since they are measured on slender structures (filament), it might be the case that significant fringing of the electric field is present outside of the samples, yielding higher capacitance values (and hence higher relative permittivity values than actually present). An FEM simulation in COMSOL was performed to show the difference between the simulation including fringe fields and the used analytical parallel plate equation used for calculating the relative permittivity values. In figure 3.10 the comparison of the simulations and analytical result can be seen, showing that the fringe fields are negligible above relative permittivities of 1×10^4, from this value onwards the capacitance calculated with the parallel plate model is within less than 5 % difference from

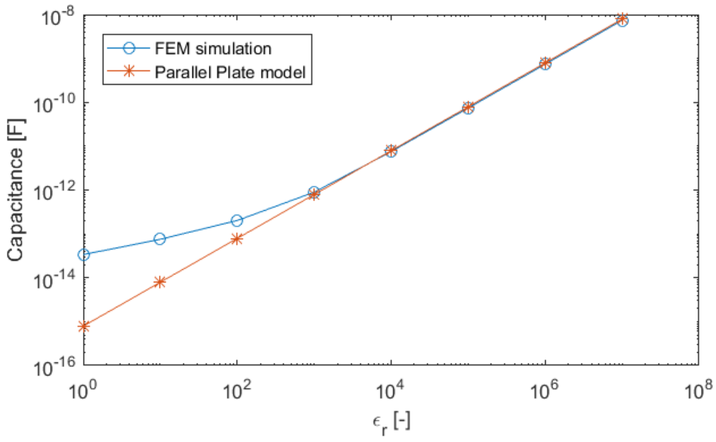

Figure 3.10: The capacitance results from a FEM simulation with fringe fields compared to the analytical parallel plate capacitor model.

the FEM simulation results. Therefore in these performed measurements the fringe fields do not alter the determined relative permittivity significantly.

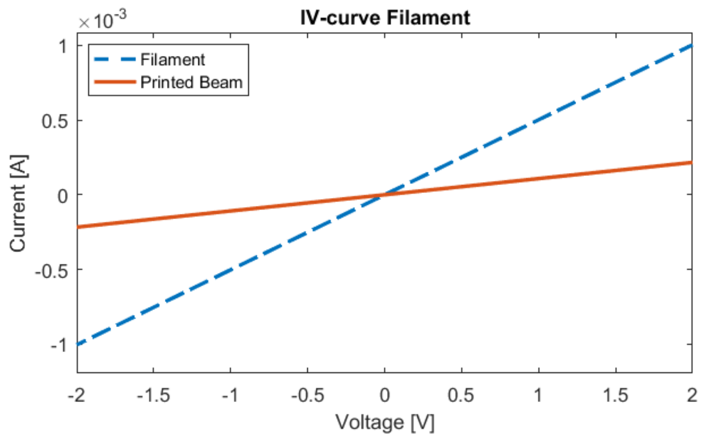

Figure 3.11: IV-curves, showing ohmic behaviour for PI-eTPU85-700+ filament and a printed beam.

It also has to be checked if nonlinear effects (like the thermal effects) affect the measurements. An IV-measurements is performed with a device suited for nonlinear measurements. During these measurements a piece of filament and a printed sample (beam) were placed in a Faraday cage and a low-voltage 4-point measurement was performed with shielded triax cables. The results in figure 3.11 show perfect ohmic behaviour and no significant nonlinear effects (the drift is at most 0.1 %). Striking is the difference in resistance for the printed sample and the unprinted material, showing a significant influence on the electrical properties by printing.

All in all the measured resistivity and relative permittivity are different from earlier measurements on the same material by Schouten, who measured $\rho = 743\,\Omega\text{m}$ and $\epsilon_r = 136$ (48). For his measurements he used a set-up for 2-point measurements, possibly affecting the outcomes because of the contact properties. A check by means of fabricating a dielectric actuator based on the work of Schouten was not possible, since due to the resistivity of the material the thermal effects would be significantly bigger than the Maxwell stresses. A final possible explanation of the high permittivity might stem from the way the permittivity is determined. So far the measured impedance is used to determine a resistance and capacitance value in parallel (based on the RC-model), from which the resistivity and permittivity can be calculated. In equation 3.2 it becomes clear that these calculations depend on the cut-off frequency and cross-sectional area. In the model the assumption of a parallel plate capacitor is taken, whereas the carbon black particles are spherical. The use of the same area for the resistivity and permittivity calculation could be the cause of the measured high permittivity, since the capacitance and the quantum-mechanical junction tunneling have a different effective area between the particles. A more extensive explanation is given in appendix C.

3.4 Conclusion

A lot of research has been done on conductive polymer composite for 3D-printing. For this particular research the commercial material PI-eTPU85-700+ is used. This material is a CPC for which the conduction can be explained by percolation theory with quantum-mechanical junction tunneling. A series micro-capacitor model is used to describe the AC electrical properties of the material. This is a simplification that does not explain the physics properly, however it captures all necessary behaviour. A more promising model for future research is the RC transmission line model. The electrical properties of PI-eTPU85-700+ are temperature dependent, but around room temperature this can be neglected. A rather homogeneous distribution of the CB particles is found in the material by SEM imaging. Dielectric impedance spectroscopy is subsequently used to measure the electrical properties. Measurements and fits to the RC-model do not fit properly, which is probably caused by the simplicity of the RC-model. The resistivity is measured to be around $0.4\,\Omega\,\mathrm{m}$ and the relative permittivity around 4×10^5. Especially the permittivity value is quite high compared to theory, however it is shown that this is not caused by non-linearities or fringe fields. Despite the large errors, the fitted values will be used as an estimate for modelling and further research. Better ways of determining and validating the values are required for future research.

4 Fabrication

This chapter discusses the sample fabrication and some effects that arise from the fabrication methods, in particular 3D-printing. As already mentioned in chapter 1, 3D-printing conditions remarkably affect the electrical properties (11).

4.1 Fabrication and Results

CAD designs are sliced with Simplify3D and 3D-printed from flexible carbon black-filled TPU (Palmiga Innovations PI-ETPU 85-700+ (8)) using a Flashforge with Flexion extruder. The designs have electrical leads on either the same (parallel) or opposite side, figure 4.1. The samples are single-layer sheets of 15 mm by 15 mm printed on glass wafers. The electrical contacts are made by putting copper tape on the wafer and connecting to the print with Ag-conductive paint (Electrolube SCP26G (69)), figure 4.2. Next wires can be soldered to the copper tape for electrical connections. Varnished wires are used (instead of a plastic shell), to prevent a lot of outgassing with SEM measurements.

A disadvantage of the Flashforge printer is the need for manual leveling of the printing bed. The manual leveling (by means of three turning knobs) can introduce significant change in the height for the single layer prints, which invalidates the model with a constant height. This could have a large effect on the voltage distribution. An attempt was done to measure the height profile by means of white light interferometry, however the lack of reflection from the black sample made it impossible to get proper results with the interferometer (Polytec MSA-400). Painting the sample white improved the measurements, however the height range of the Polytec is insufficient to measure the full height. Future measurements can be performed by means of a profilometer or stereo imaging with a SEM to determine how much the height changes. A different printer can also be used, the newly acquired Diabase Engineering printer has a probe for height calibration (the anisotropic sample from previous chapters was made on the Diabase) to adjust for the uneven printbed.

4.1.1 Nature of Contact Properties

The contacts with their electrical properties arise because of 3D-printing. The impedance of layered 3D-prints have been shown to be anisotropic because of printing (11; 10) and it was shown that an increase of z-layers for a sample with the same geometry increases the impedance (13). The nature of the contact properties has been explained by improper fusing (15) and an inhomogeneous distribution of carbon black (13).

SEM imaging of samples printed with the Flashforge printer showed voids between improperly fused traxels, figure 4.3. In these voids carbon black particles can be seen, showing that there are CB particles present between traxels. Further research is necessary to determine the nature of the contacts, since information on the contacts can be used to controlling their electrical properties.

SEM imaging from the upper surface of samples shows a varying overlap over the sample width, figure 4.4. The edges of traxels are highlighted in the SEM image (figure 4.4 a) and a paper

Figure 4.1: Sample design with leads on opposite and same (parallel) side.

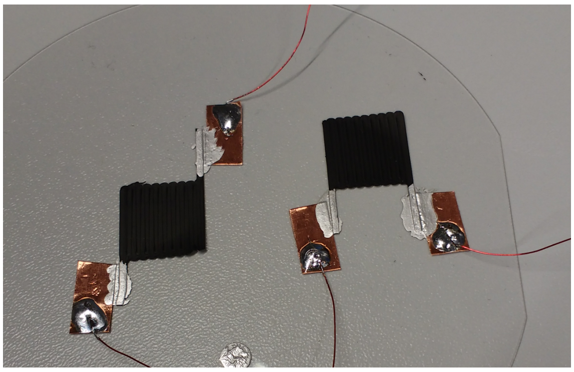

Figure 4.2: Samples on a glass wafer with wiring soldered to copper pads, connected via silver paint.

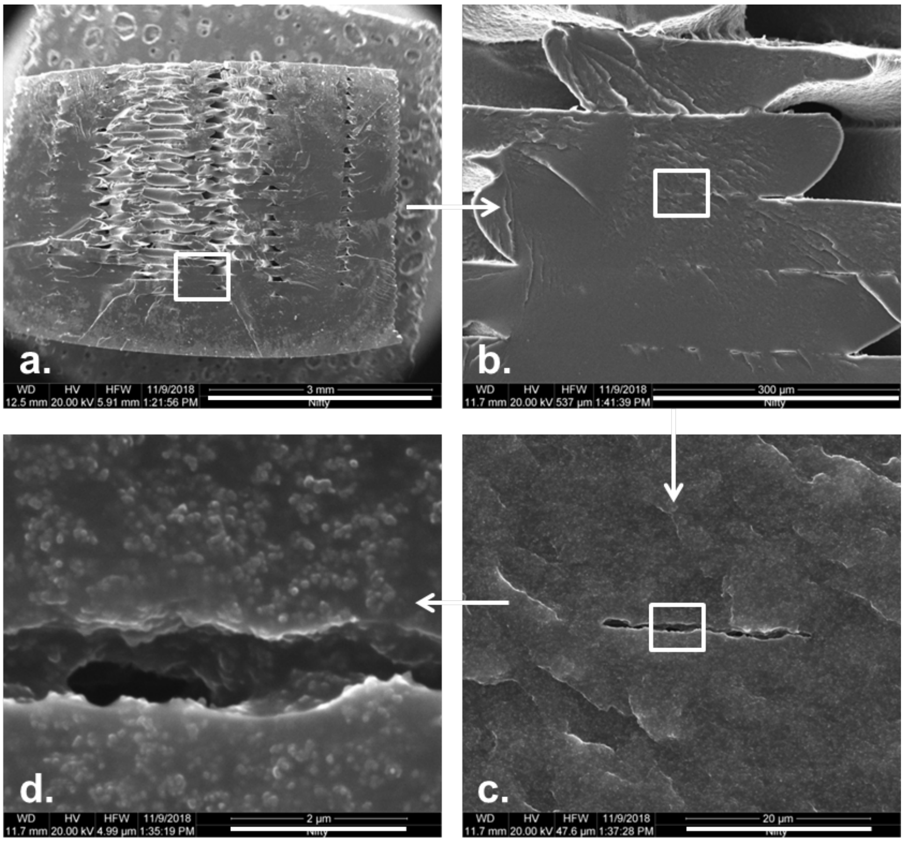

Figure 4.3: SEM images of a 3D-printed cross section prepared with cryo-fracturing: a. the full cross-section (scale bar 3 mm), b. several traxels (scale bar 300 µm), c. void between traxels (scale bar 20 µm) and d. void close-up showing CB particles in the void (scale bar 2 µm).

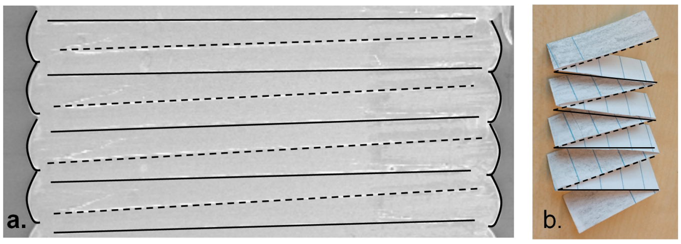

Figure 4.4: SEM image of the overlap of the traxels, with the visible edges highlighted (a), the overlap is illustrated by a folded piece of paper with the same edges highlighted (b). The overlap area is not constant over the sample width.

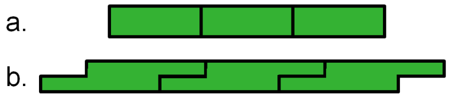

Figure 4.5: The contact geometry of the model (a) versus the contact geometry as deduced from figure 4.4. The real contact area is significantly larger than modelled, especially due to the large width compared to the height of the traxels.

imitation illustrates the edges systematically (figure 4.4 b). Because of the changing overlap over width, the contact resistance and capacitance are most likely not constant over the sample width.

Furthermore the overlap shows that the simplified contact geometry in the model (figure 4.5 a) is a lot smaller than the actual contact geometry (figure 4.5 b), especially since the traxels are only 100 μm high and 800 μm wide in the example from figure 4.4. On the measured impedance the electrical contact parameters are fitted. Since the contact area is larger in real life than the modelled contact area, the fitted contact capacitance is actually smaller and the fitted contact resistance is actually larger in they are in real life (in case the area $H\Delta x$ increases for a measured resistance and capacitance, the contact capacitance per area becomes smaller according to $C = C_0 H\Delta x$ and the contact resistance becomes bigger according to $R = \frac{\sigma}{H\Delta x}$).

4.2 Conclusion

The fabrication of the samples has been explained. For future studies it is desired to measured the height profile of 3D prints, to see how much the height influences the voltage distribution. Although the nature of the contacts is not fully clear yet and the shown differences between the model and real contact geometries affect the used resistance and capacitance, the model can still be used because of its abstraction of the actual structure into capacitances and resistances. Since the electrical contact parameters are fitted to the data, they still give the best possible representation of the actual values. The effects of the printing parameters have to be studied to understand how they both qualitatively and quantitatively affect the electrical contact characteristics. Better methods to determine the contact properties also need to be developed for this.

5 Voltage Contrast SEM

This chapter introduces the Voltage Contrast Scanning Electron Microscopy method (VCSEM) and ellaborates on it. The method makes use of the contrast that arises in SEM imaging upon a difference in electrostatic potential, since electrons at different potentials are decelerated or accelerated towards the detector in dependence of the potential of the surface. First related work with this method is presented, followed by a basic explanation of the science and operation behind a scanning electron microscope. Then the active and dynamic VCSEM theory and results are discussed.

5.1 Related Work

Over the years different applications have been found for VCSEM. Among others it is useful for direct examination of integrated circuits (IC) in the semiconductor industry, since the effects of sample biasing can be observed directly (in idustry these checks are performed with designated electron-beam systems). With IC failure analysis the failed parts of integrated circuits can often be identified quickly and the source of the difficulty traced with SEM (31; 75). This is even being used for full wafer analysis (76). An example of a failure in an IC is shown in figure 5.1a: the floating structures appear dark, whereas the grounded structures appear bright.

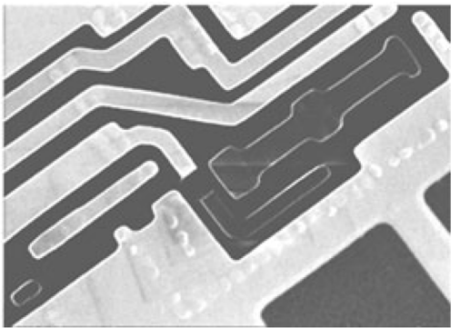

(a) A failing IC imaged with VCSEM, showing dark floating traces and bright grounded traces (31).

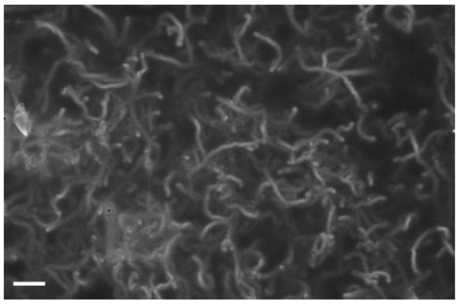

(b) SEM image of a CNT-composite with 1.3 wt.% of CNT's (at 15 kV), the scale bar is 200 nm (77).

Figure 5.1: VCSEM imaging of an IC (left) and of CNTs (right).

Another area of interest is in the field of characterizing conductive polymer composites. Imaging of carbon nano tube (CNT) percolation networks has been performed with VCSEM successfully for checking the conductive CNT networks (30; 78; 79; 80; 77). An example is shown in figure 5.1b. Similar examples discuss the use of VCSEM for the determination of the carbon black density (81) and characterization of single CNT devices (82).

Despite the elaborate research on VCSEM in certain fields, so far no example on using VCSEM to determine anisotropic properties of a conductor or mapping of the voltage in an entire area is known to the author. As a first step towards this topic, the basic operation and effects of the SEM need to be discussed.

5.2 (Voltage Contrast) SEM Basics

Image formation in scanning electron microscopy (SEM) is a combination of physical processes, electron emissions from the sample, and of a technical process related to the detection of a fraction of these electrons. This section presents the basics of SEM. It covers the microscope lay-out, the sample-beam interaction, artifacts that arise during imaging and operation parameters that are of importance. For an extended view on SEM the following work is recommended (83; 84; 85).

5.2.1 SEM Lay-out

A Scanning Electron Microscope (SEM) is a device used for studying surfaces of samples. Figure 5.2 shows the basic lay-out of the device. An electron gun emits an electron beam which is accelerated down the column. A series of electromagnetic lenses (condenser and objective lenses) and apertures control the diameter of the beam and focus the beam on a specific place of the specimen. The beam is moved in a raster like manner over the sample by a scanning coil. The sample is placed on an xyz-table which can orientate it (positioning and rotating it). Besides the sample a detector is placed to measure the electrons that arise upon interaction of the beam with the sample. The signal can then be converted into an image to be displayed. The entire device is contained within a vacuum chamber at a high vacuum level to improve the performance.

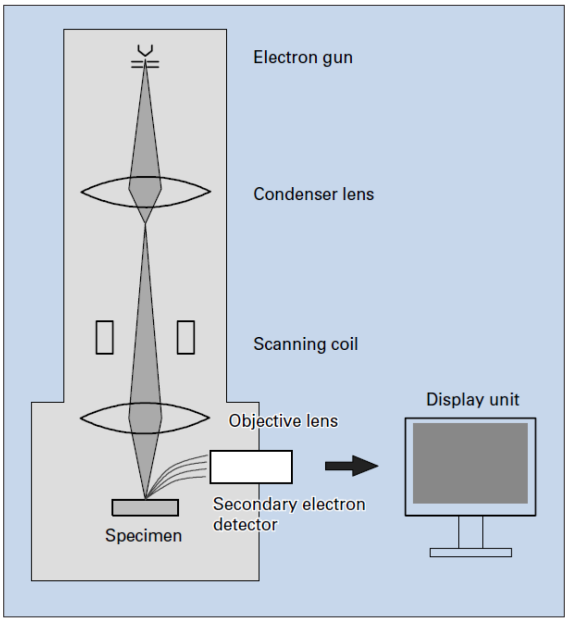

Figure 5.2: The basic lay-out of a Scanning Electron Microscope (83).

5.2.2 Beam-Specimen Interaction

The primary electrons (PE, electron from beam) can interact in the samples with the electric charge of both the atom nucleus and electrons. When the PEs enter the sample,they are scattered within the sample and gradually lose their energy until they are absorbed or leave the material again. These interactions yield multiple types of signals: backscattered electrons (BSEs), secondary electrons (SEs), X-Rays, Auger electrons and cathodeluminescence (83; 85). Our discussion will be restricted to SEs and BSEs since they are used for standard SEM imaging. The energy transfer reduces the electron travel in the solid and alters the electron directions, creating an interaction volume as shown in figure 5.3. In this volume the SEs result from inelastic events when the beam electron transfers energy to the electrons of an atom. The SEs are defined to have an energy of at most 50 eV, which makes their trajectory sensitive to local voltages (giving rise to voltage contrast). The BSEs result from elastic events when the PEs interact with the electric field of the nuclei of sample atoms, deflecting them back out of the sample. They have a high energy, ranging from 50 eV to nearly the beam energy, making them insensitive to local voltages. The elastic and inelastic events together yield the interaction volume of which the dimensions depend on both SEM settings as the sample material. The SEs have a small escape depth (approximately 5 nm for conductors and around 50 nm for insulators), whereas the BSEs can travel from a hundred times deeper due to their higher energy. Figure 5.3 shows different types of SEs.

- SE1: produced by inelastic scattering of the PEs as the beam enters the sample. These are high resolution SEs
- SE2: produced by inelastic scattering of the BSEs as they leave the sample. These are low resolution SEs
- SE3: produced by the interaction of the BSEs with the microscope pole and walls, not from the sample itself

Heavy elements have more backscattering and hence in these cases SE2 is dominant. For light elements the SE1 signal is dominant.

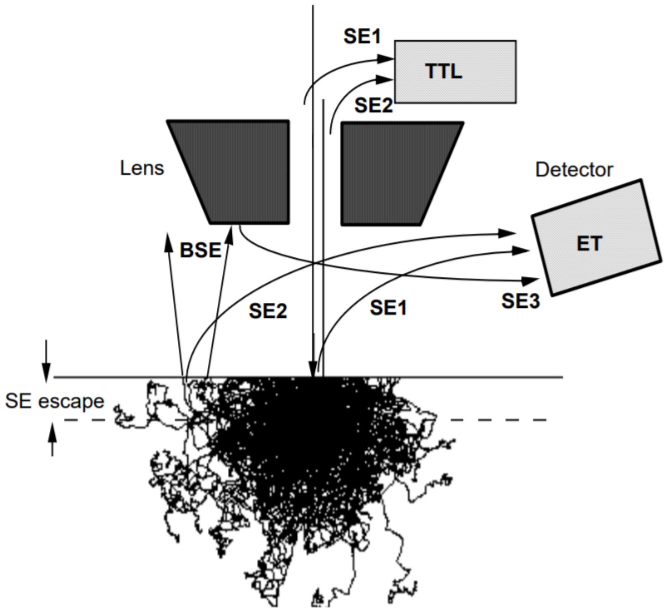

Figure 5.3: The interaction between the primary electrons (beam) and the sample, yielding different types of electrons (secondary and backscatter electrons) that are measured by the detector. The Everhart-Thornley (ET) detector is generally used for SE detection, whereas the Through-The-Lens (TTL) detector can be used to get a shadow free image (86).

As a detector mainly the Everhart-Thornley (ET) detector is used as shown in figure 5.3. It uses a Faraday cage with a positive bias relative to ground as collector electrode to attract electrons, inside the ET-detector the electrons are accelerated towards a scintillator which generates photons when hit by the electrons (83). A photomultiplier tube transforms single photons into an electric signal. The SEs are effectively pulled towards the ET-detector due to the potential difference between sample and collector. BSEs have a high energy and only hit the detector when already traveling towards it.

5.2.3 Artifacts

The standard SEM operation mainly works on the basis of material contrast (different materials yield different numbers of SEs) and topographic contrast, each with their own artifacts (both are superimposed on the voltage contrast). Figure 5.4 shows an example of topographic contrast in a 3D-printed sample with bright ridges and shadows. Topographic contrast enables to see the size, shape and texture of samples, mainly caused by the edge effect and the illumination effect. The edge effect explains the bright edges and ridges of the sample, since more SEs reach the edges through diffusion after scattering as shown in figure 5.5a. The illumination effect explains the apparent light source from the position of the detector (by default the top side of the image). BSEs and SEs with high energy directly strike the detector on the side, while from the SEs in the other direction only the lower energies electrons are attracted towards the detector.

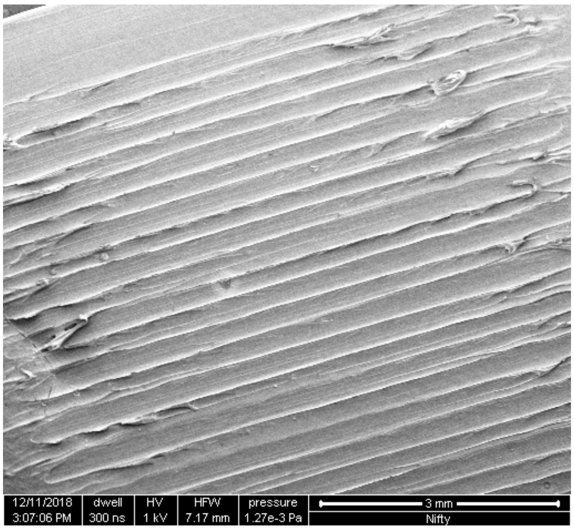

Figure 5.4: A SEM image of a conductive, single-layer, 3D-printed sheet. From the “shadows” it becomes clear that the detector is placed at the top edge of the image. The edge and topographic effect clearly show the single printed traxels.

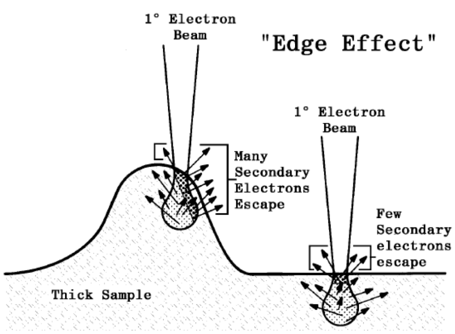

(a) Ridges and skewed surfaces emit more SEs, causing a higher measured intensity at those features (which is called the edge effect) as adapted from (85).

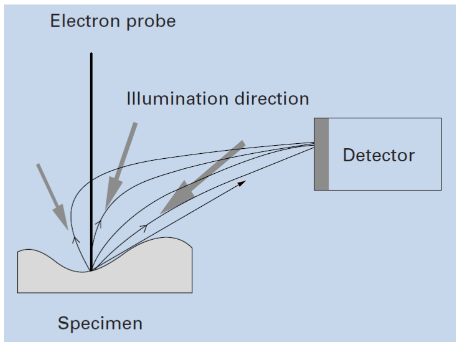

(b) The trajectory of the secondary electrons attracted towards the detector causes the illumination effect, as adapted from (83).

Figure 5.5: The edge effect (left) and illumination effect (right), which give rise to the topographical contrast in SEM.

Also beam-related contamination degrades the images. Beam-related contamination refers to the deposition of material in a region on the sample where the beam has been scanning. This is a result of the interaction of the electron beam with gaseous molecules (such as hydrocarbons) in the vacuum chamber, giving darker areas after scanning (figure 5.6).

Noise is the main limitation of SEM results. It arises from the statistical fluctuations in the discrete electron production and interaction with the sample and hence is always present (detector and circuitry noise are significantly lower than the inherent signal shot noise (87)). Due to the statistical nature the noise can be treated as Gaussian. The noise cannot be removed, but the signal-to-noise ratio (SNR) can be maximized (either by filtering or by taking more images and averaging them). The SNR is commonly used as a quantitative measure of image noise. It

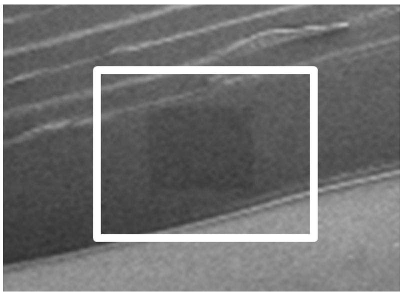

Figure 5.6: A zoomed out SEM image after scanning the same area for a while, revealing a darker rectangle of contamination within the white encirclement.

can be calculated from a series of images (e.g. a video) by a method proposed by (88) using the variances and covariances of the images:

$$\begin{aligned} R_n &= \frac{\text{cov}(I_1, I_2)}{\sqrt{\text{var}(I_1).\text{var}(I_2)}} \\ SNR &= \frac{R_n}{1 - R_n} \end{aligned} \tag{5.1}$$

R_n is called the correlation coefficient, which gives a measure for the correlation between image I_1 and I_2. This gives a good estimate of the SNR over a wide range of images with topographic detail. For estimating the SNR from single images a method exist based on median filtering (89). For this method it is assumed the image $I(x, y)$ is affected by spatially uncorrelated Gaussian white noise $N(x, y)$:

$$I(x, y) = S(x, y) + N(x, y) \tag{5.2}$$

Then $S(x, y)$ is obtained by median filtering the image $I(x, y)$ (the number of neighbours is chosen by trial-and-error). The SNR then becomes:

$$20 \log_{10}\left(\frac{\text{std}(S)}{\text{std}(N)}\right) \tag{5.3}$$

The presented methods for calculating the SNR can be used for estimating the noise in the measurements. Since in this research project the aim is to determine the voltage over an entire surface, random noise everywhere can be filtered out by median filtering and only has a small influence (sharp features are not necessary for determining the voltage).

To reduce the artifacts a low beam energy is used (defined as an acceleration voltage below 5 keV (84)). With a lower beam energy less BSE, SE2 and SE3 are generated, reducing the edge effect. A major disadvantage however is a reduced brightness (84). As will be shown later, for a large part calibration can be used to get rid of the remaining topographic artifacts and median filtering for noise.

5.2.4 Voltage Contrast Method Basics

The trajectories of secondary electrons with their low energy are sensitive to the local potentials near the specimen surface. For example, if a specimen is placed at a positive potential of 5 V with respect to ground, then there is a very high probability that the SEs will not escape the sample (they are too much attracted to the sample surface). On the other hand, a negative bias of a few volts will act as a booster for the escape of SEs and hence more of these electrons are likely to arrive at the detector. Figure 5.7 illustrates this with a sample with one side connected to ground and the other side to a positive potential. The regions with a lower positive potential are brighter since more SEs are collected in those regions.

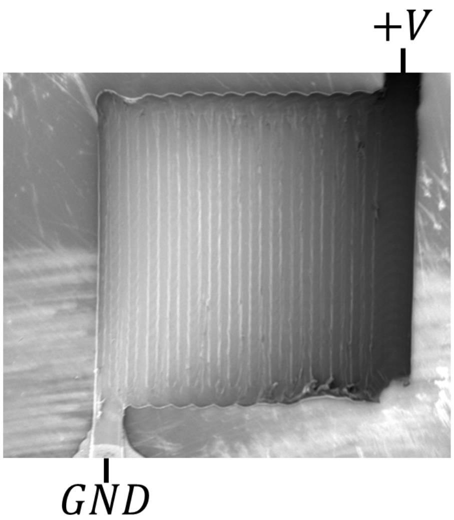

Figure 5.7: A 3D-printed sample studied with VCSEM on one end connected to ground and on the other end to a positive potential.

Figure 5.8 shows the theoretical curves associated with VCSEM. On the left the energy distribution for SEs is shown, which shifts with the value of their difference on the energy scale which in this case is the bias voltage (90) (forming the basis for active voltage contrast). The measured SE intensity as a function of bias voltage is shown on the right, where for positive potentials the SEs with the same energy do not contribute (the dark shaded area in figure 5.8 on the left). This nonlinear intensity curve can be used to map the intensities to voltages.

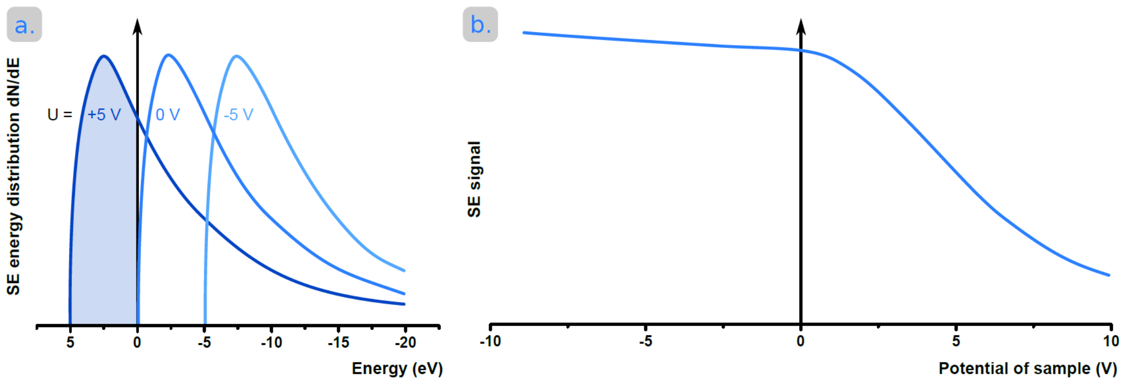

Figure 5.8: (a) The SE energy distribution ($\frac{\partial\delta}{\partial E}$) for different sample bias voltages. A bias voltage yields a shift of the total distribution. The shaded part of the distribution indicates the part of energy distribution of the electrons for which they are attracted back to the sample and hence not contributing to the image. (b) The SE signal intensity (δ) as a function of bias voltage (which is added to E in equation 5.5). Positive voltages lead to a strong decrease of the SE amount reaching the detector, while a negative potential only slightly enhances the SE yield. Adapted from (30).

The shape of the SE energy distribution can be calculated for respectively metals and insulators with (91; 92):

$$\begin{aligned}\left(\frac{\partial\delta}{\partial E}\right)_{\text{metal}} &= F_1\frac{E}{(E+\phi)^4}\\ \left(\frac{\partial\delta}{\partial E}\right)_{\text{insulator}} &= F_2\frac{E}{(E+\chi)^3}\end{aligned} \tag{5.4}$$

With δ the detected SE yield, E the SE energy, ϕ the work function of the material (the mininum amount of required work to remove an electron from the solid to a point in vacuum) and χ is the electron affinity (defined as the energy obtained by moving an electron from the vacuum just outside the semiconductor to the bottom of the conduction band just inside the semiconductor). The prefactors F are superfluous since they only affect the magnitude and not the shape (the normalized curves are sufficient). Upon integration of equation 5.4 over E one arrives at the theoretical SE intensity curve shapes (where the minus sign is taken in the proportionality):

$$\begin{aligned} k_{\text{SE,metal}} &\propto \frac{3E+\phi}{6(E+\phi)^3} \\ k_{\text{SE,insulator}} &\propto \frac{2E+\chi}{2(E+\chi)^2} \end{aligned} \tag{5.5}$$

There are different types of voltage contrast, being caused by: charging of electrically floating objects (accelerating or decelerating the PEs), external biasing (shifting the SE energy distribution), deflection of SEs in the electric field and finally contrast due to ferroelectric domains (30). The biasing method is called active VCSEM and will be used throughout this study.

Quantitative VCSEM

There is no unambiguous relation between voltage and image intensity because both the local micro fields but also the macro fields influence the SE contrast formation, resulting in different contrast of regions at the same potential (30; 93) (this can only partially be calibrated for, since the calibration is done with homogeneous voltages and not for distributions). The SE trajectories are very sensitive to the transverse electric field and uniform fields. The presence of a uniform field does not affect the determination of relative potentials, but disturbs quantitative measurements. The effect of transverse fields can be reduced by using a large acceleration voltage normal to the sample by means of an extraction electrode biased positively to a few hundreds of volts (26), however proper quantitative voltage contrast is only possible by using (retarding-field) energy spectrometers (30; 94; 93) with which the shift in the peak of the SE yield can be measured (and even for spectrometers errors of millivolts to volts can be expected (95; 96; 97)). Since a SEM will be used without vertical extraction field or spectrometer, only small voltages will be used to limit the disturbances (for small voltages the microfields are closer to homogeneous sample potential fields as used for calibration). Also microfields from the grounded stage and chamber affect the trajectories and therefore the detection of SEs. FEM simulations have been done to investigate this, the results are given in appendix D. It was found that the grounded stage and chamber affect the SE trajectories, influencing the measured intensity of the detector.

VCSEM with Carbon-Based CPCs

For inhomogeneous conductive materials like CPCs the voltage contrast can be generated as long as two requirements are met: non-uniform permittivity and avoidance of charging of the specimen as a whole (77). Some research has been done on VCSEM with carbon-based CPCs (98; 81; 80; 77). Li et al. focused on the low voltage case (80), where they showed that the contrast between the polymer and CNTs inverts two times in the acceleration voltage range of 0.3 kV to 5 kV as shown in figure 5.9. At high energies CB particles appear brighter than the polymer, which is believed to be mainly because of electron trapping in CB due to polarization charges on the material interface (and a lowering in polymer charging because PEs penetrate deeper and are conducted away by the CB network). The negative charging of the CNTs push the SEs to the detector, causing them to light up. In general for cases where charge reversal occurs, it is advised to operate below 2 kV acceleration voltage since positive charging can only go up to a few volts while negative charging can become rather big and deflect the electron probe. Furthermore a high energy beam implants charges deep in the sample and negative charge can remain there for a long time (99). The switch between positive and negative charging occurs at the acceleration voltage E_2 (figure 5.9), which is generally above 1 kV for polymers. Below E_2 the SE yield of the CB is not dominant (and hence using carbon data for equation 5.5 is not fully correct). However it is chosen to use an acceleration voltage of 1 kV for the positive charging and reduced damage.

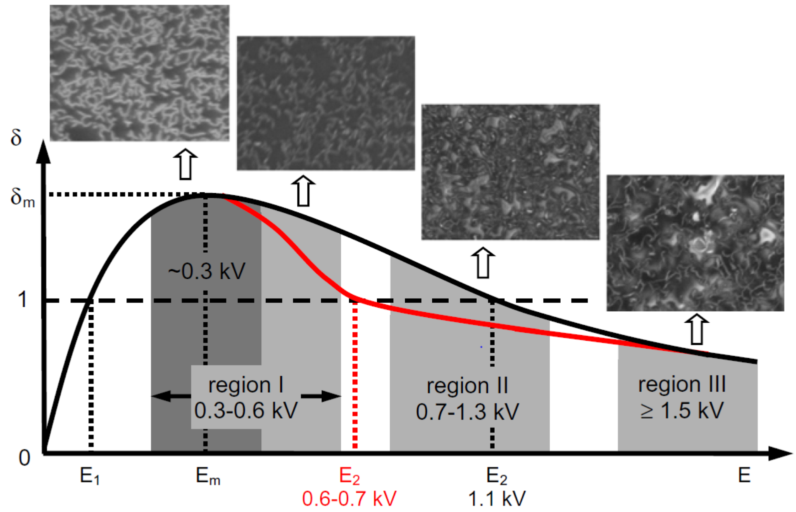

Figure 5.9: Schematic diagram of SE yield δ as a function of accelerating voltage with corresponding CNT contrast images. The black and red curves denote the two possible SE yield trends for epoxy. The curves are divided into three segments according to the contrast of the displayed images (80).

5.3 SEM Settings

The VCSEM measurements are performed with an FEI Quanta 450, all the mentioned parameters refer to this device. This device adjusts many of the parameters automatically, hence only some parameters have to be adjusted by the user making it more user-friendly. VCSEM in practice is influenced by several parameters (which mainly affect the ratio of the useful SE1 yield with respect to the combined noisy SE2/SE3/BSE yield). The parameters that can be affected are:

- Acceleration voltage: increases the PE energy which reduces voltage contrast (30). For charging and degradation purposes a value of 1 kV is chosen (suited for delicate samples).
- Magnification: reduced voltage contrast with increased magnification. Due to the large sample size low magnification is chosen.
- Working distance: an increase in working distance reduces the voltage contrast (30). Increasing the working distance increases the depth of focus, which on its turn decreases resolution and increases aberrations. Furthermore a large working distance automatically places the ET-detector higher above the sample, giving more vertical extraction and reducing micro field disturbances. The maximum working distance was chosen (also to get the sample fully in view).
- Spot size: in the FEI the spotsize can be chosen as a unitless number (the actual value is determined by acceleration voltage), for which 4 was chosen (suited for low magnification)
- Contrast and brightness sensitivity: these settings are determined individually per sample by means of the autosetting of the SEM and increase the contrast (generally both are around 0.5).
- Detector voltage: an increased detector voltage increases the voltage contrast (since it extracts the low energy SEs). The default of 250 V is used.

5.4 Active VCSEM

The previous sections have focused on the working of scanning electron microscopy with VCSEM in particular. The first VCSEM operation mode studied is active voltage contrast, in which a DC bias is applied and the SE intensity is studied. For every pixel a calibration curve is recorded (like the theoretical curve in figure 5.8 b) by biasing the entire sample. The images are filtered with a median filter to remove the stochastic noise and every curve is normalized (with respect to its own maximum value) to obtain the pixel-wise calibration curves (topographic effects are reduced in this pixel-wise normalization). An example is given in figure 5.10. The typical curves can be seen for different samples (with as inset a sample image), where one drawback is that clipping of the intensity occurs for (a) outside of the voltage range 2 V to 7 V, for (b) for a bias larger than 2 V and for (c) for a bias larger than 6 V. The black line in every plot in figure 5.8 corresponds to the theoretical value of carbon (equation 5.5), which does not fit well likely due to the clipping.

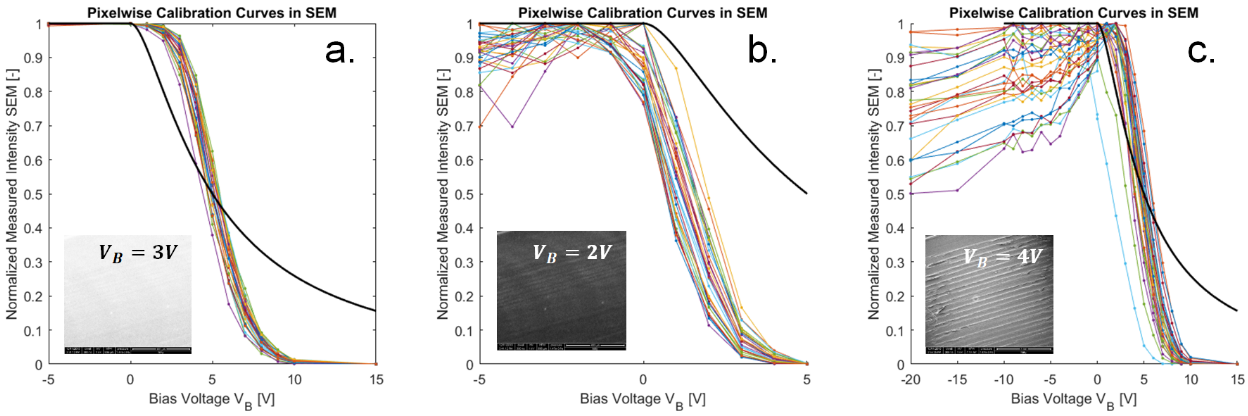

Figure 5.10: Pixel-wise calibration curves as function of bias voltage V_B with insets of the corresponding sample for (a): a close-up of a 3D-printed sample without topography and with high brightness (intensity clipping outside of the voltage range 2 V to 7 V), (b): the same sample as in (a) with a lower brightness (intensity clipping for a bias bigger than 2 V) and (c) a 3D-printed sample with topography (intensity clipping for a bias bigger than 6 V). The black line in every image is the theoretical intensity for carbon.

From figure 5.10 (c) it becomes clear that a sample with more topography gives a larger spread in calibration curves and has a bivalent curve (it is monovalent if just the negative or positive voltages are considered). After calibration one sample lead is grounded while a bias is applied to the other lead. An image can be made of the sample intensity distribution and again be median-filtered. Polynomials are fit to the pixel-wise curves to determine the voltage distribution of the image (where it is important to have a monovalent curve since every intensity value needs to be mapped to a single voltage value) as shown on the left in figure 5.11. After multiplying the intensity image with the inverse fits, the voltage distribution is obtained (right side figure 5.11). The image can then also be masked (a mask is created by means of edge detection and logical operations) to remove the background for more clarity as shown in figure 5.12.

The sample in figure 5.11 is made of paper with pencil graphite, giving a very smooth surface and almost no topography artifacts. Results of printed samples are shown in figure 5.12, giving the VCSEM contrast compared to the determined voltage. This result shows the difficulty of proper quantitative analysis without an energy spectrometer. The applied voltage are respectively −1 V to 1 V and 10 V to 20 V, so the quantitative comparison shows that the VCSEM results are off by approximately 0.4 V for the opposite sample at the leads (which is around 20 %) and approximately 1.0 V for the parallel sample at the leads (which is around 10 %).

In figures 5.11 and 5.12 bulk conduction occurs. To also show anisotropic behaviour in figure 5.13 a sample tailored for traxel conduction is shown (it is printed as a single, meandering

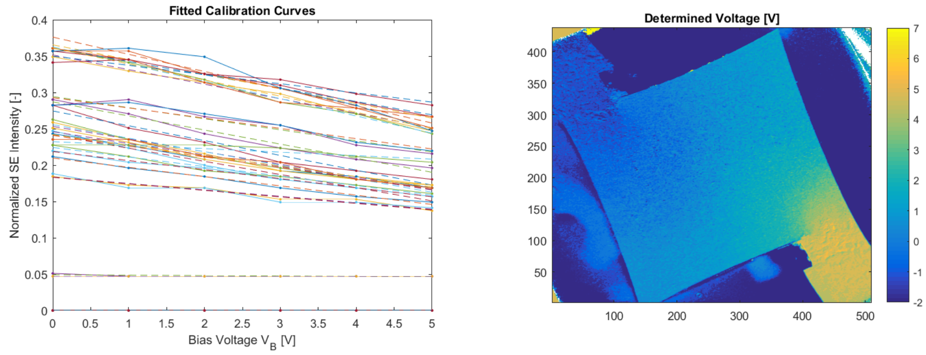

Figure 5.11: Pixelwise calibration curves with linear fits (left) and the determined sample voltage by mapping the measured intensity (the applied voltage is 0 V to 5 V, the fits are also made in this range).

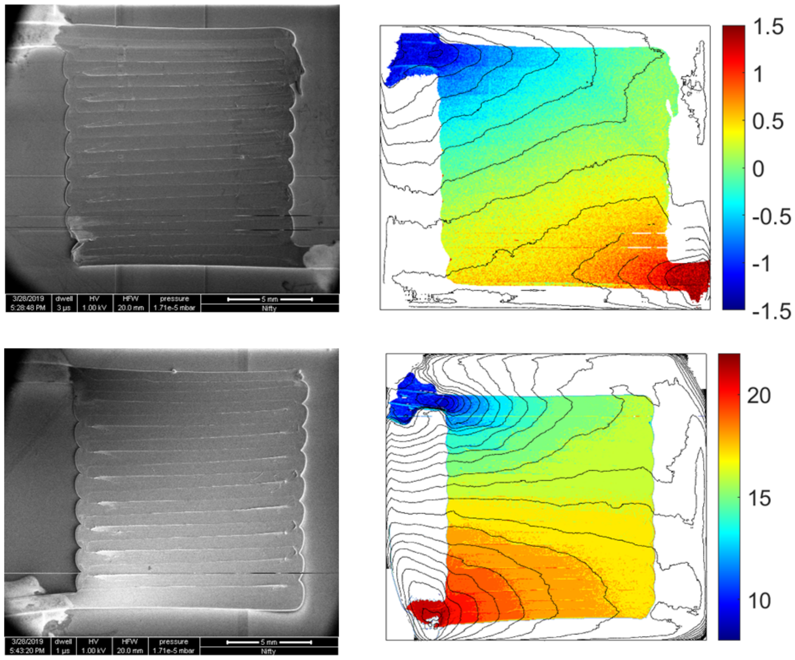

Figure 5.12: VCSEM contrast compared to the determined voltages for opposite (top) and parallel leads (bottom). The applied voltages are −1 V to 1 V (top) and 10 V to 20 V (bottom), which is exceeded in both cases by the determined voltages.

traxel with gaps between the meanders). From this sample the calibration curves could not be used for determining the voltage since they are ambivalent (the average curve over the entire sample is shown in figure 5.15). This brings us to the challenges that still need to be tackled for understanding and improving active VCSEM.

5.4.1 Challenges active VCSEM

The basic operation of active VCSEM is understood and can be used qualitatively and a first steps is made towards quantitative measurements, however there are still many effects that pose challenges and still need further research. An overview is listed below:

- Topography Artifacts: the edge and illumination effect in the ridges of the sample generate quite some artifacts in the determined voltage as can be seen when comparing the smooth paper sample (figure 5.11) to 3D-printed samples (figure 5.12). Pixel-wise calibration and median-filtering is not sufficient to fully remove this.

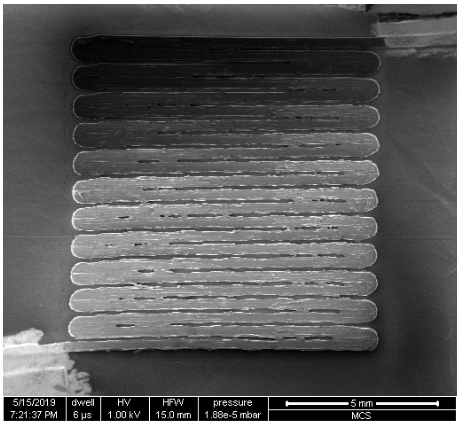

Figure 5.13: A VCSEM image of a purely anisotropic sample (meandering traxel without contacts), showing traxel conduction.

- Fitting Errors: So far mainly linear fits have been applied for determining the voltage from the calibration curves to prevent issues with bivalent calibration curves. For small voltage differences this works quite well (figure 5.11), however higher order fits can significantly improve the results when single-valued curves can be guaranteed.
- Chamber Electric Fields: The electric fields (e.g. caused by the grounded stage and sample) in the SEM chamber significantly affect the measurements. The grounded stage and charging of the substrate attracts or accelerates electrons, changing the SE detector yield. As discussed earlier, this can be circumvented by using an energy spectrometer (or improved by using a larger, more symmetrical extraction field). If this is not possible further study is necessary to determine the ideal substrate voltage conditions by for example grounding the substrate.
- Detector Voltage: Some presented measurements have been done at a normal detector voltage (250 V) and some at 0 V. Despite a lower SNR and less intensity, the second case gives monovalent curves around 0 V to 10 V where this sometimes is not the case for normal operation. Since only the high energy SEs are measured, some artifacts are reduced. This can be used for better results when the effects in normal operation are not satisfactory. The difference in calibration curves for the detector voltages can be seen in figure 5.14, where for the 0 V detector voltage in the range 0 V to 10 V the intensity is quite linear.
- Substrate Material and Charging: Substrates of silicon, glass or one of both covered with kapton have been used, all yielding different calibration curves. Silicon seems to give the least amount of charging, however it gives problems with shorting and capacitive coupling with AC signals (and is less suited for thermal measurements). The glass and kapton substrate surfaces showed significant charging, making it more difficult to do repeatable measurements. A better way to reduce the influence of the substrate is still desired (or a different choice of substrate). An example of the influence of the substrate can be seen in figure 5.15, where a second voltage sweep was performed to remeasure the calibration curve. This resulted in a shifted calibration curve, most likely because of charging (the microfields give rise to a similar effect with the grounded stage). For DC and low frequency measurements a silicon substrate with a thin insulator, to prevent short circuiting, can be used to reduce problems with charging.
- Contamination and Degradation: Beam-induced contamination as well as sample degradation occur during measurements as shown in figure 5.6. This both affects the measured intensity and possibly the electrical properties of the sample. For this reason a low beam energy is used.

- Heating: During the first measurements samples became overheated and detached from the substrate. Proper adhesion to the substrate is required to prevent this and the power dissipation in operation should be adjusted for operation in vacuum.
- Measurement Inaccuracies: Voltages are currently applied by hand with an analog source (reading from the analog dial gives a significant error). Improvements in the accuracy can be made by using a digital source and by automating the measurements.
- Sample Dimensions: Currently the largest working distance of the SEM is used and samples fill almost the entire field of view. Around the edges deformation of the samples can be measured, since the SEM is not suited for such large samples (e.g. the height difference in the paper sample seems to cause the curved edges in figure 5.11).
- Electrical Drift: in some calibration curves a jump is present around 0 V as shown on the right in figure 5.14, which is caused by the way of measuring (the connections have to be switched from the negative to the positive connection by hand during measurements). The drop in intensity might be caused by various effects: errors in the applied voltage, charging, contamination, a change in impedance of the sample (the jump is measured when one measures the calibration curve from 0 V to −20 V and then from 0 V to 20 V).
- Acceleration Voltage: as described in the section on CPCs with VCSEM, the acceleration voltages makes a large difference in charging and contrast. In the experiments the acceleration voltage was always set to 1 kV, the effect of this and other values still needs to be studied.
- Shape Calibration Curves: For the theoretical SE intensity curves the work function of carbon is used. It is however unclear whether the SEs of the CB or of the TPU are dominant around the acceleration voltage of 1 kV. Currently the shapes of the calibration curves for normal detection operation are qualitatively similar, however mismatches are present. This might be caused by the dominance of SEs from the TPU, on the left in figure 5.14 the curves are less steep than the theoretical curve, which is the case for insulators (99).

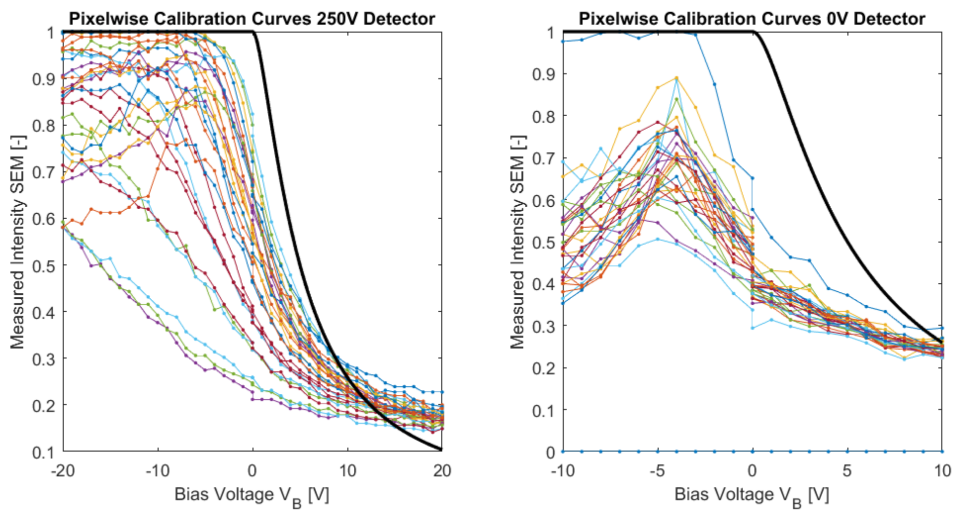

Figure 5.14: Pixelwise calibration curves (not normalized) of a 3D-print on kapton on silicon for a default detector voltage (left, 250 V) and for 0 V detector (right), showing a difference in intensity and curve shape.

5.5 Dynamic VCSEM

With active VCSEM the DC voltage distribution can be measured, however for AC measurements a different method is required. With dynamic VCSEM the asymmetry of the SE intensity

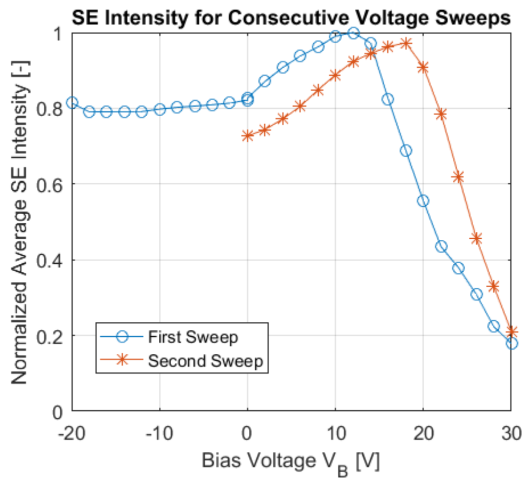

Figure 5.15: Calibration Curve Measurement for a 3D-printed sample on kapton on glass, showing a shift in Calibration curve for the second voltage sweep (swept from low to high voltage).

curve is used with asymmetrical sample driving to obtain an intensity distribution. The basics are shown in figure 5.16.

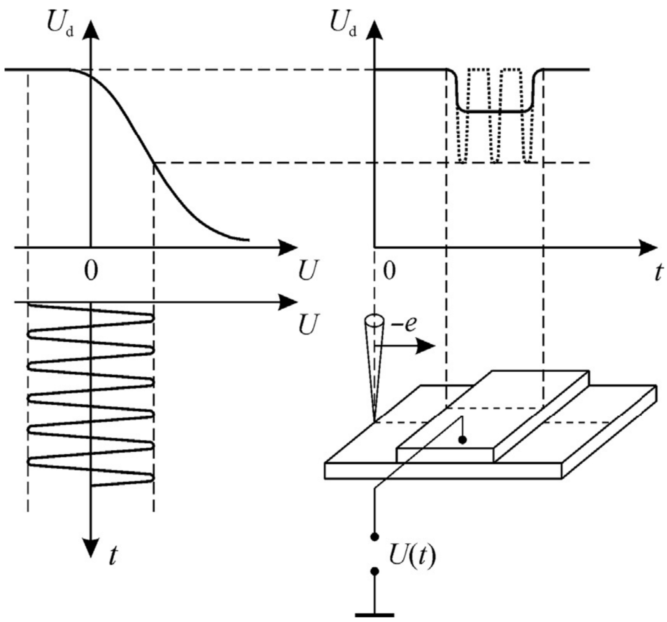

Figure 5.16: Detector transfer characteristic of a SEM, which illustrates the formation of dynamic VC-SEM (90). A harmonic voltage (lower left) is applied to the sample and a probe scans the sample (lower right). The instantaneous voltage yields an SE intensity from the intensity curve (upper left), from which the electron probe then measures a harmonically modulated nonlinear intensity while scanning over the sample.

A sample is grounded on one lead and a sinusoïdal signal is applied on the other lead (bottom left figure 5.16). The sine is "mapped" asymmetrically into an intensity in the SEM via the SE intensity function of the scanned sample (for $V \leq 0\,\text{V}$ the intensity is 1, for $V > 0\,\text{V}$ the intensity follows the curve). If the SEM electron probe scans over the AC signal, the intensity is modulated with the signal (top right figure 5.16, the dotted line indicates the measured intensity). When measuring the sample several times and averaging (averaging can be done with the video, and already happens in the SEM for high frequencies), the regions with the alternating voltage appear darker on the image. The analytical model for this method is derived in appendix F. For a sine with period T, amplitude V_p and bias V_b, a linear approximation of the measured averaged SE intensity then becomes (with a the linearized slope of the DC SE intensity function in equation 5.5):

$$k_{\text{SE,AC}} = \frac{-a}{\pi}\sqrt{V_\text{p}^2 - V_\text{b}^2} - aV_\text{b}\left(\frac{\pi + 2\arcsin(V_\text{b}/V_\text{p})}{2\pi}\right) + 1 \tag{5.6}$$

To tailor the measured SE intensity, both the signal amplitude and bias can be tweaked. For the best result the bias voltage is taken at the point of maximum nonlinearity ($V_\text{b} = 0$) (90). The theoretical AC intensity function in this case is shown in figure 5.17a (showing the full curve and the derived linear variant from equation 5.6).

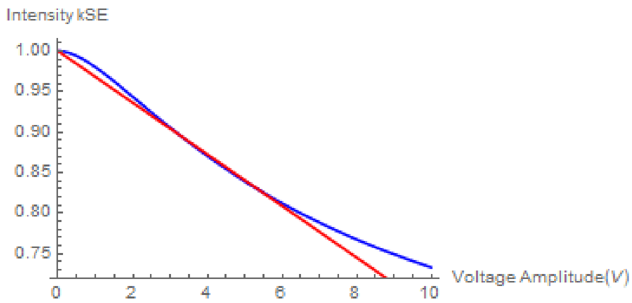

(a) The theoretical model for average measured SE intensity as a function of signal amplitude (and the linearized case).

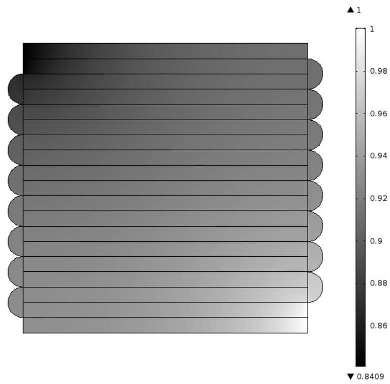

(b) Linear SE intensity function applied to a FEM model of a sample with $V_\text{p} = 5\,\text{V}$ and 0 V bias, the intensity corresponds to the values in figure 5.17a.

Figure 5.17: Theoretical SE intensity for a varying amplitude (left) and a FEM simulation showing the intensity based on the linear theoretical curve.

The curve in figure 5.17a is the calibration curve as used for dynamic VCSEM (0 bias and variable amplitude). It can be measured by applying the same AC signal to both samples leads (like with the bias in the DC case) and averaging the frames of the recorded SEM video. In case this curve function is applied to the average intensity from a video, one should obtain the average voltage of the sample (the bias, which in this case should be 0 V). Therefore to properly compare the simulated voltage of a sample to the measured case, the calibration curve is applied to the simulated voltage. One drawback of this method is that pixel-wise operations cannot easily be used to reduce the topographical artifacts, since the modelled voltage cannot easily be mapped to pixels in the SEM images (noise on the other hand is very limited since the images are averaged). For now the average calibration curve will be applied to the model. To check measurements the average voltage (hence the bias) can simply be determined with the calibration curve and the average voltage should be 0 V everywhere.

A FEM model mapped with the theoretical calibration curve is shown in figure 5.17b, where the signal amplitude is $V_\text{p} = 5\,\text{V}$ (a similar mapping can be performed with the model results). The signal lead appears dark (top left) and the grounded lead appears bright (bottom right) as expected, where the intensity values check out with figure 5.17a.

Several measurements have been performed, with and without bias voltage. For the calibration curve in these measurements still a fixed amplitude of 5 V and a variable bias were used, with the curves in figure 5.18. The pixel-wise curves are compared to the theoretical AC and the DC SE intensities. The AC curve seems to give a better description of the measured curves, except for the intensity around −5 V to 0 V (it is unclear where this difference comes from).

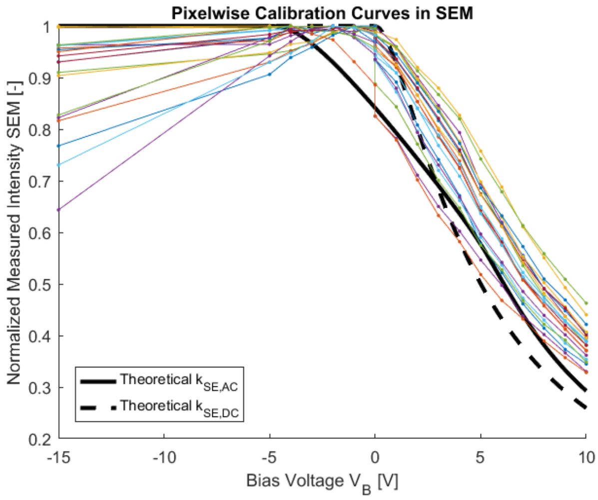

Figure 5.18: AC pixel-wise calibration curves for a 3D-printed sample with a signal amplitude of 5 V and a varied bias voltage (hence a bias mode measurement). The theoretical AC and DC SE intensity curves are also shown.

As mentioned the averaged intensity images should show a contrast distribution (like the simulated case in figure 5.17b). In figure 5.19a and 5.19b averaged distributions are shown. In these images a fixed amplitude of 5 V at a frequency of 0.1 Hz was used for a bias of respectively 2 V and 0 V. The ground (and bias) is connected to the upper right and appears significantly brighter in both cases. The signal is applied to the bottom left lead, yielding a darker area. However comparing the average intensities to the DC 0 V calibration image, shows that the intensity distribution is mainly caused by topography and sample orientation and no proper conclusions can be drawn.

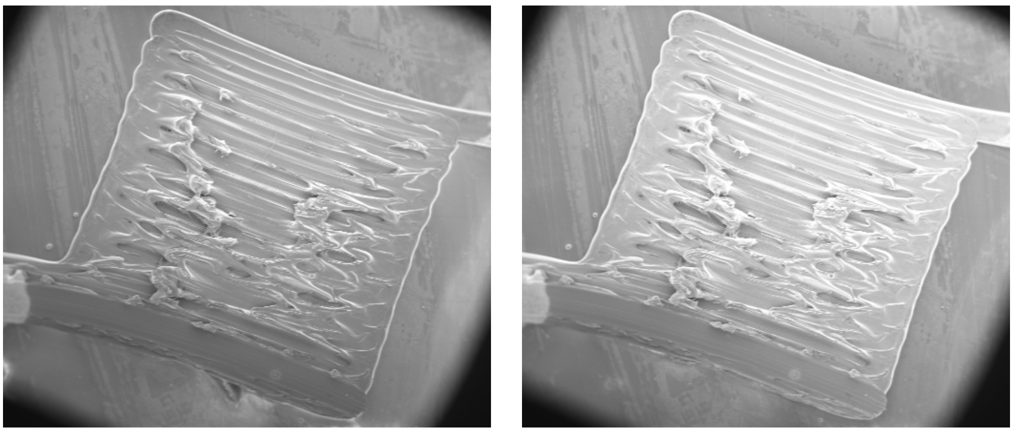

(a) The sample at 0.1 Hz with 2 V bias and 5 V amplitude.

(b) The sample at 0.1 Hz with 0 V bias and 5 V amplitude.

Figure 5.19: Averaged intensity image for a sample at different bias voltages. The rough surface topography is caused by imperfect printing settings.

The determined calibration functions (figure 5.18) were used to map the intensities to a voltage, however for both cases this theoretically gives incorrect results. The calibration curve was made for full amplitudes of 5 V and a variable bias, whereas the samples have a variable amplitude and a constant bias. In figure 5.20a and 5.20b it can therefore be seen that at the driving lead (with a full amplitude) the average voltage values are found with a high accuracy (respectively 2 V and 0 V), while towards the grounded and biased lead the errors becomes quite significant.

The error is smaller for the unbiased case, since the intensity around the flat maximum and negative voltages is used, whereas for the biased case a larger skewed part is used (yielding larger errors). In future measurements therefore the correct calibration curve should be measured for the suited measurement mode (curves for varying amplitude). A bias can only be used if the full calibration curve has also been made with this bias. However since the maximum nonlinearity is at 0 bias, it is advised to not use any bias.

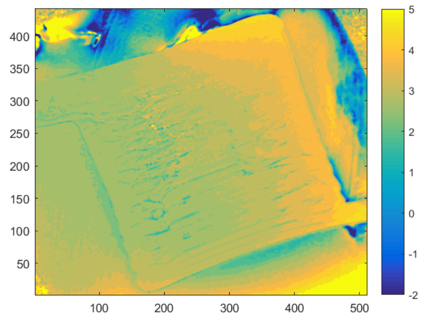

(a) Determined average voltage from the sample in figure 5.19a. The voltage in the top left driving lead is determined correctly (2 V), however errors occur throughout the rest of the sample.

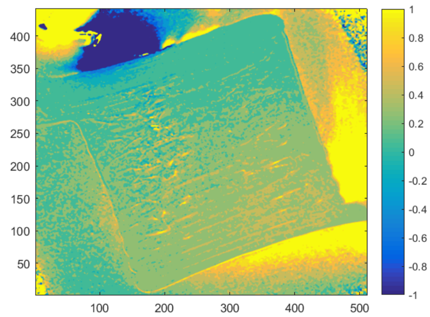

(b) Determined average voltage from the sample in figure 5.19b. The voltage in the top left driving lead is determined correctly (0 V), however errors occur throughout the rest of the sample.

Figure 5.20: Determined average voltage, showing errors since the distribution is not constant.

Finally one feature of dynamic VCSEM has to be pointed out. In figure 5.16 on the top right the measured modulated intensity is shown. This signal can also be found in the real measurements, with an example at 1 MHz in figure 5.21, where Moire fringes appear. Due to the difference in speed of the horizontal and vertical scanning, the pattern is tilted. The tilt and the width of the fringes depends on the signal frequency (the fringes become wider for lower frequencies). By averaging all the video frames, a single image without fringes can be obtained (spatial filtering should not be used on the fringes, since this removes part of the actual signal intensity).

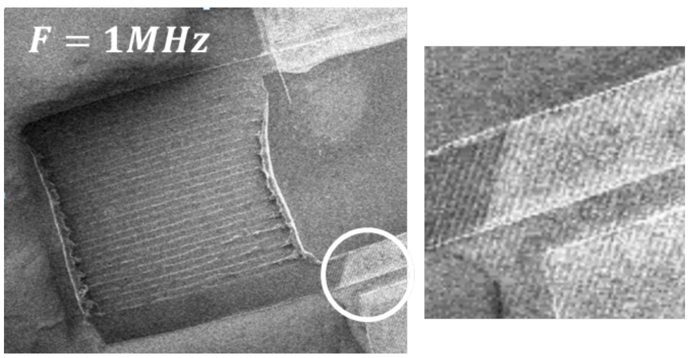

Figure 5.21: Moire fringes for a sample driven at 1 MHz.

5.5.1 Challenges dynamic VCSEM

The concept of dynamic VCSEM has been explained and simulations and measurements have been shown. Several challenges can be pinpointed:

- Active VCSEM challenges: Almost all challenges of active VCSEM described in section 5.4.1 also apply to dynamic VCSEM. Only the noise is a lot lower and needs less filtering, since the stochastic noise is already averaged out.
- Pixel-wise calibration: Pixel-wise calibration can only be used for mapping the intensity to a homogeneous voltage. The pixel-wise curves cannot easily be applied to the modelled voltage to study the expected intensity. Therefore topographical artifacts are more significant in the dynamic case.
- Signal Amplitude and Bias: As mentioned in previous section, the calibration curves should be made with the proper signal amplitude and bias, which is also used for the measurements. A bias of 0 V is advised to maximally utilize the calibration curve asymmetry.
- Substrate Material: For silicon wafers flickering of the wafer was measured during AC experiments. This is probably due to capacitive coupling and junction-like behaviour. Therefore no conductive or semiconductor materialshould be used as substrate for the AC experiments.
- Model Comparison: Comparing the data to the models is more difficult for the dynamic case, since the model has to be converted to an intensity (and hence either a theoretical SE intensity curve has to be used or a measured curve). For actual comparisons it is advised to use the averaged curve from the pixel-wise calibration curves.

5.6 Conclusion

In this chapter an introduction has been given into the basics of SEM, beam-sample interaction and the artifacts that arise due to the detection method. The voltage contrast method has been explained and both theoretical and experimental results have been shown. With the current set-up only qualitative measurements can be done, where for quantitative measurements an energy spectrometer (retarding field analyzer) is required to reduce the effects of micro and macro-fields around the sample and in the chamber.

For active VCSEM a method was presented to measure the SE intensity as a function of bias voltage per pixel. The resulting calibration curves can be fitted and used to determine the voltage distributions from intensity images of the same sample. Qualitative results were presented, however quantitative measurement did not match the actual voltages (most likely due to the presence of micro and macro-fields). For further improvement of the qualitative measurements more research needs to be done on the effect of the electric fields, the most suited substrate material to reduce charging, the effect of the acceleration voltage on the measurements and the deviations from theoretical SE intensity curves.

For dynamic VCSEM the theory has been presented and applied to the simulations. Due to the different basis of operation (asymmetry in the intensity due to the local signal amplitude instead of a relation between the bias and the intensity) the model results need to be mapped to an expected intensity to compare to the VCSEM results properly. A check of the measurements was shown by determining the voltage from the intensity measurements; which should yield the homogeneous, average voltage of the entire sample. The first steps of dynamic VCSEM have been shown, however measurements are still needed in order to show the voltage distribution of a sample at a high frequency.

All in all the voltage contrast method can be applied to characterizing the voltage distribution in anisotropic 3D-printed samples qualitatively and improvements have been proposed.

6 Infrared Thermography

In this chapter infrared thermography (IR thermography) is introduced as method to study power density in 3D-printed samples. With IR thermography the thermal radiation is measured, which is related to the power dissipation within the sample (due to ohmic/Joule/resistive heating the sample heats up and radiates IR light). Related work to this method and its use is presented, followed by a basic explanation of the physics, theoretical modelling and finally measurement results.

6.1 Related Work

Several relevant examples of IR thermography in combination with Joule heating of anisotropic solids exist. In the field of carbon fiber reinforced polymers (CFRP) the technique has been used for validating models of anisotropic resistivity due to fiber orientation and layering (39), figure 6.1a. This has also been done in the field of conductive fabrics, where IR thermography was used to fit a model to the measured current distribution to determine contact resistances between yarns (28; 100). Furthermore the anisotropic conduction in CNT webs was measured with IR thermography (101). Finally some studies show that it can be used for detecting defects in micro electronics and PCBs, where more advanced measurement schemes are used to achieve the required precision (lock-in thermography, in which an AC signal is applied and each pixel temperature is studied around the excitation frequency) (102; 103). All cases have in common that IR thermography is used next to a model. This is because it is an indirect measurement (IR is measured instead of the temperature, where the temperature is a result of Joule heating and heat transfer) and therefore the interpretation of the measurements is often not clear and unique. Furthermore in all mentioned examples the technique was shown to be suitable for finding defects or studying the anisotropic current distribution, which is also the goal of this study (3D-printing contacts can be considered as defects in an isotropic solid).

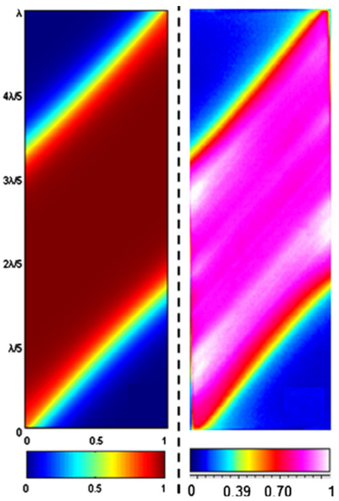

(a) Modelled (left) and measured (right) temperature of an anisotropic CFRP sample with Joule heating (39).

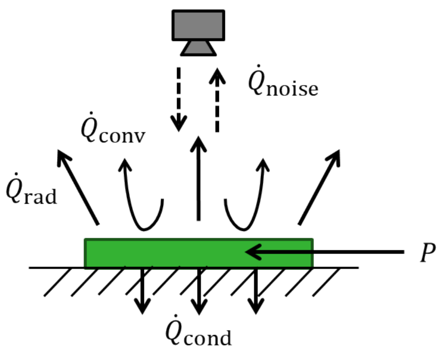

(b) Heat transfer in and from a sample during IR thermography (with additional noise from the camera and surroundings).

Figure 6.1: IR thermography with Joule heating in literature (left) and the schematic heat transfer during IR thermography (right).

6.2 Basics Infrared Thermography

The temperature induced at the surface of the sample is strongly affected by the heat generation, by the design of the 3D-print (geometry and materials) and by the thermal environment (cooling conditions). For the cooling conditions three forms of heat transfer need to be considered:

- Conduction: Heat transfer from the more energetic particles of a substance to the adjacent less energetic particles through interactions between the particles, described by equation 6.2.
- Convection: Heat transfer between a solid surface and the adjacent liquid or gas that is in motion, described by equation 6.3.
- Radiation: The energy emitted by matter in the form of electromagnetic waves due to changes in the electronic configurations, described by equation 6.4.

In a stationary system the generated heat (Joule heating P_{joule}) equals the dissipated heat (conduction $\dot{Q}_{\text{cond}}$, convection $\dot{Q}_{\text{conv}}$ and radiation $\dot{Q}_{\text{rad}}$) as shown in figure 6.1b:

$$P_{\text{joule}} = \dot{Q}_{\text{cond}} + \dot{Q}_{\text{conv}} + \dot{Q}_{\text{rad}} \tag{6.1}$$

Where the expressions for the three forms of heat transfer as well as the Joule heating are given by:

$$\dot{Q}_{\text{cond}} = -kA\frac{\nabla T}{L} \tag{6.2}$$

$$\dot{Q}_{\text{conv}} = hA_{\text{s}}(T_{\text{s}} - T_{\infty}) \tag{6.3}$$

$$\dot{Q}_{\text{rad}} = \epsilon\sigma A_{\text{s}}(T_{\text{s}} - T_{\infty}) \tag{6.4}$$

$$P_{\text{joule}} = UI = \frac{1}{2}\Re\left\{\frac{U \cdot U^*}{Z}\right\} \tag{6.5}$$

With k the thermal conductivity of a material in $\mathrm{W\,m^{-1}\,K^{-1}}$, A the surface area of the heat transfer in $\mathrm{m^2}$, h the convection heat transfer coefficient in $\mathrm{W\,m^{-2}\,K^{-1}}$ (an experimentally determined parameter depending on e.g. surface geometry and fluid motion), T_{s} the surface temperature in K, T_{∞} the surroundings temperature in K, ϵ the emissivity of the surface (a measure of how close a surface approximates a black body, which radiates all its energy and does not reflect heat), σ the Stefan-Boltzmann constant in $\mathrm{W\,m^{-2}\,K^{-4}}$ (the constant with which the total intensity radiated of a black body over all wavelengths increases as the temperature increases) and finally Z the impedance of the sample in Ω. With IR thermography the radiation is what is measured to determine the surface temperature. An important parameter is the emissivity, which depends on the material, angle and surface roughness. Since the camera is already programmed with a default emissivity value (0.9), this will cause errors in the actual results. Next to this reflections of the surroundings and of the camera and user also affect measurements (figure 6.1b).

With Joule heating the heat produced equals the electric power dissipated. The time averaged power dissipation is given in equation 6.5 (the instantaneous power would be $P = \Re\{U \cdot I\} = \Re\left\{\frac{U^2}{Z}\right\}$). The temperature rises quadratically with the voltage (while the cooling power only rises linearly with the temperature). To improve the measurements lock-in thermography can be used, where a sinewave is applied and the signals can be filtered to obtain the excited frequencies. A general AC input signal has an amplitude U_{p} and a bias U_{b}:

$$U(t) = U_{\text{p}}\sin(\omega t) + U_{\text{b}} \tag{6.6}$$

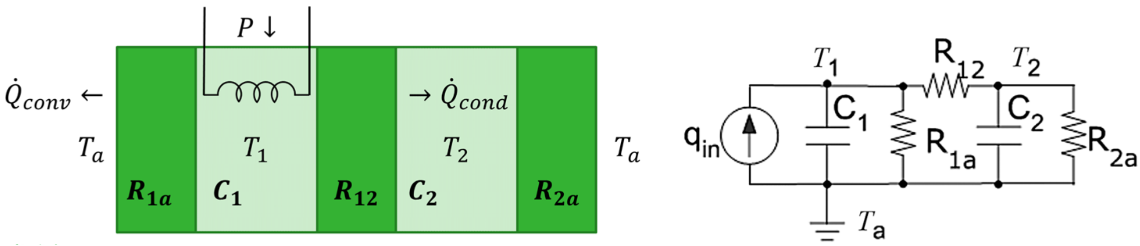

Figure 6.2: Physical model (left) and equivalent circuit (right) for thermal calculations (104).

The dissipated power can be found from combining equation 6.5 and 6.6:

$$P(t) = \Re\left\{\frac{U^2}{Z}\right\} = \Re\left\{\frac{U_\mathrm{b}^2 + 2U_\mathrm{p}U_\mathrm{b}\sin(\omega t) - \frac{1}{2}U_\mathrm{p}^2\cos(2\omega t) + \frac{1}{2}U_\mathrm{p}^2}{Z}\right\} \tag{6.7}$$

It is clear that next to the excitation frequency a second harmonic (2ω) arises in the frequency response of the temperature. With the expressions for the heat transfer and Joule heating a simple model can be made.

6.3 Thermal Modelling

To gain a basic understanding of the physical system and experiments a simple model has been made (the calculations and values are rough estimates). Furthermore the power dissipation has been implemented in the analytical model.

6.3.1 Lumped Model

A lumped physical model and its circuit equivalent are shown in figure 6.2. In this model R_{1a} is the thermal resistance of convection, R_{12} is the thermal resistance of the sample, R_{2a} is the thermal resistance of the substrate, C_1 is the heat capacitance of the sample and finally C_2 is the heat capacity of the substrate. Several assumptions are made in the model:

- Heat only flows perpendicular to the sample and substrate (one-dimensional heat conduction in horizontal direction). This is reasonable in case the sample and substrate are thin and convection and conduction to the surroundings are high.
- The bottom of the substrate is cooled to ambient temperature, which is possible in case of enough cooling.
- Radiation losses are neglected, since low sample temperatures are expected (from previous experiments temperatures of around 30 °C were measured) and there is a lot of cooling (during the model radiation was found to be approximately 5 % of the total heat transfer compared to convection with 16 % and conduction with 79 %).

The circuit on the right in figure 6.2 has been reduced to a single equivalent impedance:

$$Z_\mathrm{eq} = \frac{1}{j\omega C_1 + 1/R_{1\mathrm{a}} + 1/(R_{12} + 1/(j\omega C_2 + 1/R_{2\mathrm{a}}))} \tag{6.8}$$

The response of this model to a power input as in equation 6.7 has been simulated. During the simulation approximately 1 % random noise is added to the temperature to represent the noise from the surroundings (the value of 1 % was found by trial-and-error to resemble the experimental data in figure 6.8). The thermal cut-off frequency of the system is around 0.1 Hz. The experiments are performed at a driving frequency of 0.02 Hz, which is within the thermal bandwidth of the system. The signal is sampled at 1/10 of the signal frequency (satisfying Nyquist). For the parameter values and calculation of the convection coefficient appendix G can be consulted. The model has been calculated for both a silicon and glass wafer as substrate. The density and heat capacity of glass and silicon are approximately the same, however silicon has a more than 100 times higher thermal conductivity. This results in smaller temperature differences, making it more difficult to measure fluctuating temperatures on silicon wafers. Therefore glass wafers will be used for the experiments. The calculated temperature and frequency spectrum for a glass wafer can be seen in figure 6.3, where the signal frequency as well as the second harmonic are present. Measurements are expected to show approximately the same behaviour.

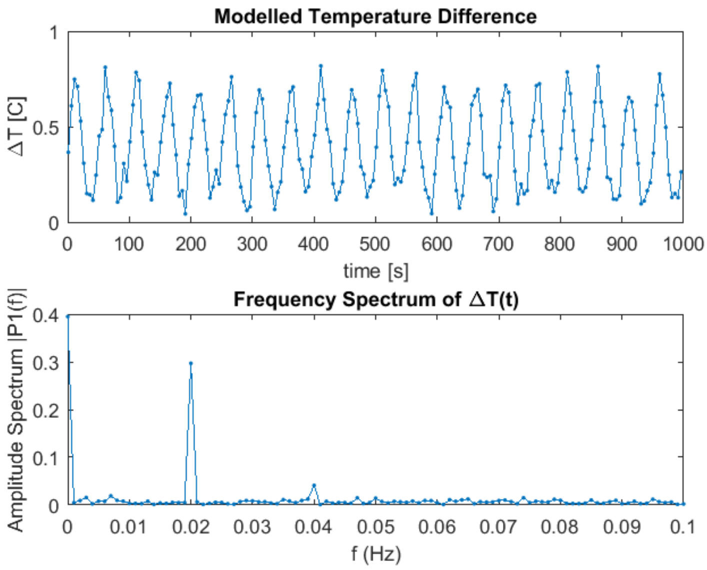

Figure 6.3: Temperature difference and frequency spectrum of the sample simulated using the circuit model in figure 6.2.

6.3.2 Power Dissipation

The power density has also been implemented in the (analytical) Matlab model from chapter 2. For the power the RMS value ($\frac{1}{2}$ times the peak value due to the squared voltage) has been used to compare to the measurement temperatures, since this gives the average power. To compute both the power dissipation due to the currents in the x as in the y-direction, half of the power dissipation of both adjacent contacts is added to the bulk power dissipation (where bulk power dissipation is taken in the center of the traxel):

$$\begin{aligned}\Delta P_n = &\frac{1}{2}\Re\left\{\left(\hat{U}_n(x+\Delta x)-\hat{U}_n(x)\right)\cdot I_n^*(x)\right\}\\ &+\frac{1}{4}\Re\left\{\frac{\left(\hat{U}_n(x)-\hat{U}_{n-1}(x)\right)\left(\hat{U}_n(x)-\hat{U}_{n-1}(x)\right)^*}{Z_{\text{it}}(\Delta x)}\right\}\\ &+\frac{1}{4}\Re\left\{\frac{\left(\hat{U}_n(x)-\hat{U}_{n+1}(x)\right)\left(\hat{U}_n(x)-\hat{U}_{n+1}(x)\right)^*}{Z_{\text{it}}(\Delta x)}\right\}\end{aligned} \tag{6.9}$$

Where $Z_{\text{it}}(\Delta x)$ is the inter-traxel impedance for a length Δx. This has been verified with FEM simulations in the same way as in chapter 2. A result of the model is shown in figure 6.4, where the analytical model is compared to FEM simulations and measurements performed by Wolterink (unpublished measurements connected to (13)) with large contacts (with fitted values for the model and FEM to match the measurements). In plots of the power dissipation, the power dissipation density is used (power dissipation per volume), to have a result independent of sample dimensions.

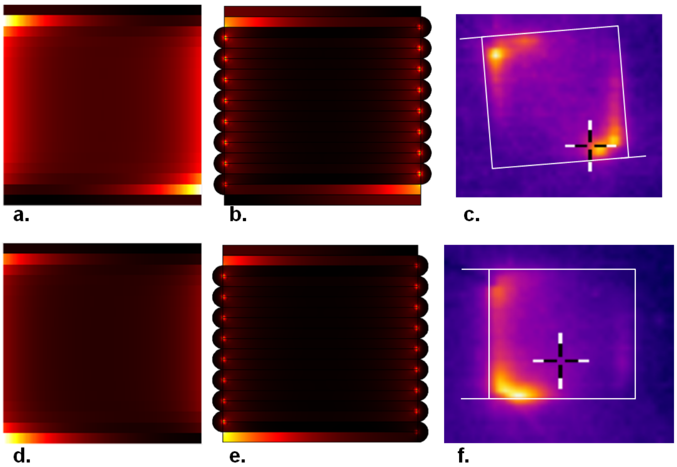

Figure 6.4: The power dissipation density according to model (a,d), FEM simulations (b,e) and as measured with thermal IR imaging by Wolterink (c,f) for same side leads (a,b,c) and opposite side (d,e,f) samples. The same linear colour scale is used for (a,b,d,e). In (c,f) an intuitive color scale from the FLIR software is shown (the iron palette, with a nonlinear scale), where the scale of (c) and (f) differs slightly.

6.4 Experimental Method

IR thermography measurements can be done as comparison to the models and simulations. For the experiments a USB thermal camera for smartphones is used (FLIR ONE Gen 2) for photos and timelapses. This particular type of camera has been tested and calibrated for clinical measurements, and showed comparable performance to a tested high-end thermal camera (checking for absolute temperature, relative temperatures, temporal variations and repeatability) (105). Important from these tests is that a spot size must be at least 10 pixels in diameter for a meaningful temperature measurement and 20 pixels in diameter to give an accurate measurement, which means that the camera has to be placed close for small samples (in the experiment the camera is placed at approximately 4 cm distance). Furthermore start-up effects occur during the first measurement, so the camera should not be turned off during measurements and the first measurement should not be taken into account. Relative measurements are measured with high accuracy, whereas absolute temperatures deviate a bit and have small variations over time.

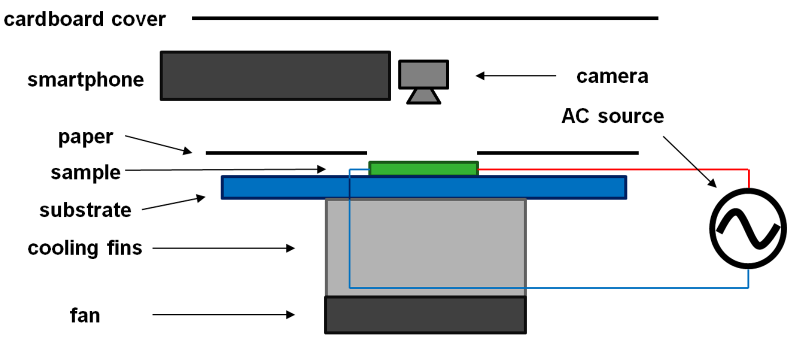

Figure 6.5: Experimental set-up for the IR thermography measurements.

The total experimental set-up for the IR thermography is shown in figure 6.5. The FLIR one camera is plugged into a smartphone placed over the sample. An AC source is connected to the sample to provide power for the Joule heating. The rest of the set-up is aimed at reducing unwanted effects and noise. The sample with substrate is placed on a cooling block with fan for active cooling. This ensures a thermal steady state during measurements, reduces thermal blurring (heating of the entire sample, which reduces thermal resolution) and enables faster measurements (heat is lost quicker). Next to this a cardboard cover is placed over the set-up to shield the measurements from heat sources in the lab (e.g. people, lighting). A paper cover is placed over the substrate to shield the camera from reflections (the camera and smartphone heat up during use and the glas substrate acts as thermal mirror).

6.4.1 Low and High Frequency IR Thermography

DC measurements can be done by taking a picture of the heated sample. When measurements are dominated by noise or when the spatial temperature difference is too small, lock-in thermography can be used. As explained earlier this uses an AC signal and the unwanted frequencies are filtered out per pixel, only the excitation frequency and its second harmonic carry useful information (as can be seen from the expression for the power in equation 6.7). The spatial resolution is limited by thermal blurring, which can be improved with a higher lock-in signal frequency (a higher lock-in frequency reduces the thermal diffusion length (106), which reduces blurring). On the other hand a higher lock-in frequency also leads to lower signal strength (since due to the heat capacitance the sample can only partly follow the heating power). Furthermore the Nyquist theorem has to be taken into account, limiting the lock-in frequency to $f_{\text{lock-in}} < f_{\text{frame}}/4$. To capture both the excitation signal and the second harmonic at least 4 frames of the IR camera per signal period are needed to yield the amplitude and phase information in each pixel independently (106). The sampling frequency of any thermal camera is limited by slow thermal processes, hence for the high frequency measurements a different method is required.

For thermal measurements on high frequency Joule heating (where high is defined as everything above the cut-off frequency of 0.1 Hz) the method of amplitude modulation could be an option. With amplitude modulation the desired high frequency signal is the carrier wave, from which the amplitude is modulated with a low frequency signal that can be measured, figure 6.6. In this way the Joule heating occurs for the high frequency, whereas the low frequency can be measured and used for lock-in thermography. For high frequency measurements a source is required which can deliver high enough voltages and which can go up to 1 MHz, to make sure enough power can be supplied to the sample.

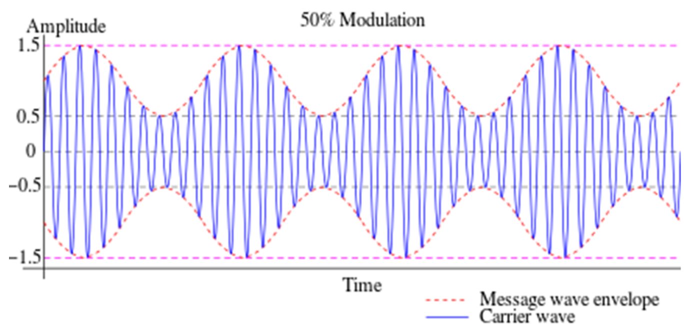

Figure 6.6: Illustration of amplitude modulation, showing the high frequency carrier wave for the heating and the low frequency wave for the measurement (107).

6.5 Results

Images of the measured temperature distribution at low frequency are given in figure 6.7. The samples are heated with a sinusoidal voltage in the range of 20 V to 50 V at 0.02 Hz.

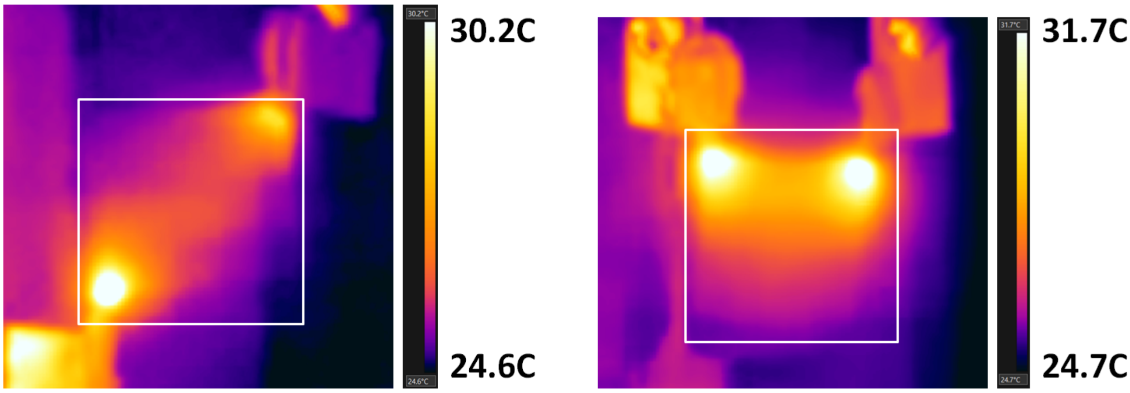

Figure 6.7: Infrared Lock-In Thermography for a 0.02 Hz measurement with almost isotropic samples at 50 V driving, the raw images are shown.

A pixel-wise analysis has been performed on the measurement of the right sample in figure 6.7. In figure 6.8 these measurements have been shown for a pixel in the center of a hot spot, at the outer edge of the sample and on the substrate. The 0.02 Hz excitation and its second harmonic can clearly be seen in both the intensity and the frequency spectrum, as opposed to the substrate pixel (showing mainly noise). The measured temperatures in the plot from figure 6.8 and figure 6.7 are several Kelvin, while the modelled temperature difference is below 1 K (figure 6.3). This can be explained from IR measurements of the back of the glass wafer during cooling, which showed hot spots with a high temperature. Hence the condition that the bottom of the wafer is cooled to ambient temperature is not valid, likely causing the difference between model and measurements. Furthermore the temperature variations in figure 6.3 are average temperature changes, while the temperature changes of the hot spot in figure 6.8 are far above average (since it is measured in the point that heats up most).

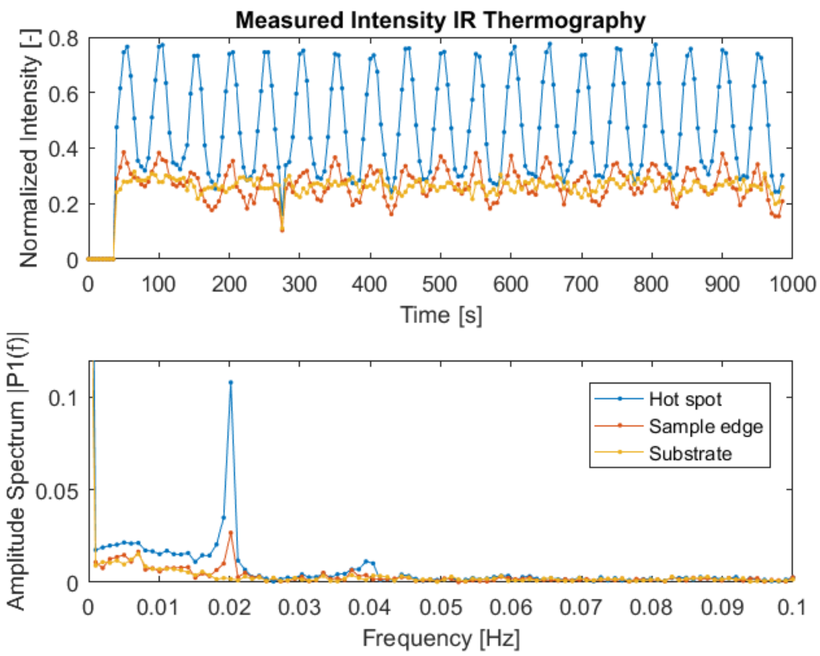

Figure 6.8: Measured in pixel with maximum heating (hot spot).

In figure 6.9a and in figure 6.9b the filtered image of the lock-in thermography video from figures 6.7 and 6.8 are shown (giving the relative intensity from the excitation frequency and its second harmonic). The filtered image is almost noise free and the contacts appear very dim. The filtering is done by taking out all signal except for excitation frequency and its first harmonic (with a band of ±0.005 Hz around the excitation frequency peak and a band of ±0.01 Hz around the second harmonic peak). The conduction occurs directly between the two leads with some spreading through the rest of the sample. Furthermore some conduction occurs through the edge opposite of the leads, caused by the lower number of contacts between the bends (as can be seen clearly in the model and simulations in figure 6.4). From the figures it becomes clear that lock-in thermography can clear out the static heating and lot of the noise. The lock-in method could also be used for the VCSEM method (although noise is less significant in that case).

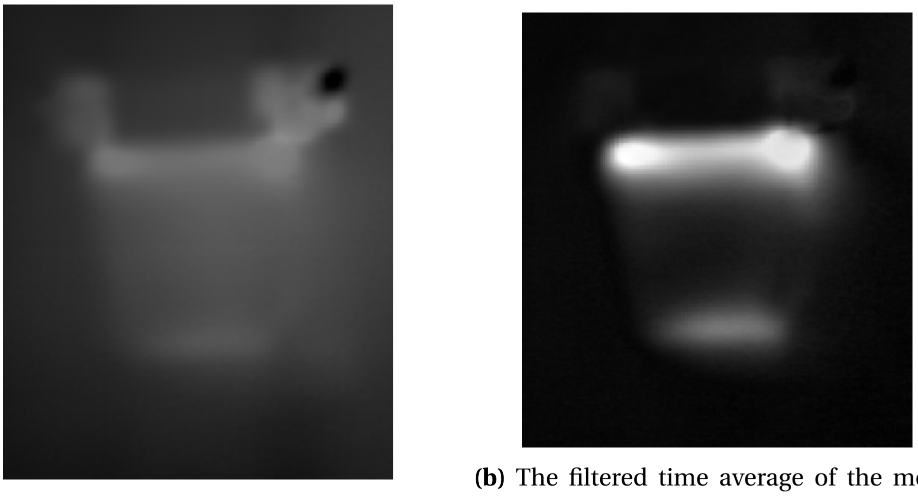

(a) The unfiltered time average of the measured temperature distribution, showing the leads and noise from the substrate.

(b) The filtered time average of the measured temperature distribution, yielding just the intensity at the excitation frequency and its second harmonic.

Figure 6.9: The unfiltered, time average of the measured temperature distribution (left) compared to the filtered, time average of the measured temperature distribution (right) from the right sample in figure 6.7.

Different samples have also been measured. Measurements on the paper sample from previous chapter indicate a difference in resistivity over the sample, the result is shown in appendix E. The anisotropic meander sample shows approximately equal heating throughout the entire sample in figure 6.10, which fits with theory since the resistivity and hence heating of a single traxel is the same everywhere. The individual traxel cannot be recognized, likely due to thermal blurring combined with blurring from the too small focus distance (the distance of 4 cm is closer than the focus distance of 15 cm from a similar camera, the FLIR one Pro). Improvements can be made with higher lock-in frequency and better (use of the) camera. Lock-in IR thermography with amplitude modulation still needs to be researched for the high frequency case.

6.5.1 Challenges

IR thermography has not been as studied as extensively as VCSEM has been studied during this project, therefore some challenges and opportunities can be identified for future research.

- Cooling Conditions: The thermal losses in the model are not well defined, as was found from the hot spots on the back of the glass substrate. Both a more extensive model needs to be used and better defined cooling conditions need to be applied to improve the comparison of model to measurements.
- Camera Performance: The current camera has a relatively low resolution, requiring to film from close by for the small samples (closer than the focus distance). This likely in-

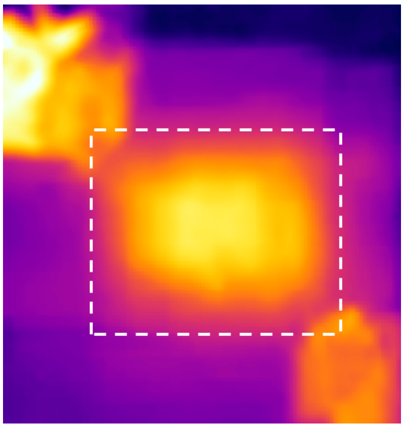

Figure 6.10: IR thermography measurement on a single meandering traxel, showing heating throughout the entire sample (sample from figure 5.13).

duces blurriness. Furthermore the current camera has a very limited frame rate, which limits faster experiments and higher lock-in frequencies (and hence reduced spatial resolution).

- High Frequency Measurements: The lock-in thermography method with amplitude modulation still has to be implemented and tested, to be able to measure samples at high frequencies.
- Emissivity eTPU: Relatively high temperatures have been measured with the camera (the surroundings in figure 6.7 indicate more than 24 °C). The low emissivity of the camera (0.9) and the close distance during filming might be explanations for the spurious temperatures (105). The emissivity of eTPU can be determined experimentally to improve the quantitative measurements (although mainly the local temperature difference is of interest, making the temperature offset less important).
- Thermal Blurring: As discussed a higher lock-in frequency can be used to reduce thermal blurring. In this way it might be possible to distinguish individual traxels in the measurements.
- Quantitative analysis: To improve the quantitative analysis a thermocouple can be included in the measurement set-up to adjust for offsets in the camera. Furthermore the power can be measured and used to improve the cooling condition parameters (through equation 6.1).

6.6 Conclusion

IR thermography by means of Joule heating has been studied in literature, showing the importance of modelling alongside the measurements. A simple equivalent circuit model has been presented, predicting a frequency response with a second harmonic from the quadratic relation between voltage and temperature. Qualitatively similar results were found in the measurements, however the temperature differences did not match (most likely because of comparing the average temperature, as calculated in the model, to measured hot spot temperatures). Next the power dissipation has been included in the Matlab model, showing the possibility to qualitatively capture measured temperature distributions. For better results lock-in thermography can be used to remove static heating and noise. It has been suggested that amplitude modulation combined with lock-in thermography could potentially be used to measure the temperature distribution at high sample frequencies. However this still needs to be implemented and tested. Furthermore improvements in measurement approaches are required to obtain improved quantitative experimental results, enabling comparison of modelling and measurements. Several options for improvement have been proposed.

7 Results

This chapter shows the measurement results from the different measurement methods with the manufactured samples from previous chapter. The measurement data is compared to the developed model and to FEM simulations. The measurement methods are performed as described in their corresponding chapters.

Variable\Sample	**Opposite**	**Parallel**
Resistivity ρ	$2.8\,\Omega\,\mathrm{m}$	$2.8\,\Omega\,\mathrm{m}$
Relative permittivity ϵ_{r}	0.9×10^5	1.5×10^5
Inter-traxel resistivity σ	$2 \times 10^{-3}\,\Omega\,\mathrm{m}^2$	$2 \times 10^{-3}\,\Omega\,\mathrm{m}^2$
Inter-traxel capacitance C_0	$2.8 \times 10^{-4}\,\mathrm{F\,m}^{-2}$	$4 \times 10^{-3}\,\mathrm{F\,m}^{-2}$
Traxel width W	0.8 mm	0.8 mm
Traxel length L	15 mm	15 mm
Traxel height H	200 µm	200 µm
Number of traxels N	19	19
Frequency f	1 Hz to 1×10^8 Hz	1 Hz to 1×10^8 Hz

Table 7.1: Modelling and simulation parameters for the parallel and opposite sample.

7.1 Modelling and Simulations

The model and FEM simulations are compared to the results from the different measurement methods. The electrical parameters are fitted on the global electrical measurements and are shown in table 7.1 together with the geometrical parameters.

7.2 Electrical Measurements

Electrical measurements have been performed on the sample with both the LCR and the gain-phase analyzer. The gain-phase results are shown in figure 7.1, where they are compared to the FEM simulations and the analytical model . The LCR measurements are compromised and therefore are not included. The data shows a good fit from 1 kHz to 1 MHz. Some deviations occur at both lower (around 100 Hz) and higher frequencies (around 1 MHz) for which the cause is still unclear. The fitted model parameters are presented in table 7.1.

7.3 VCSEM Measurements

Fig 7.2 shows the DC VCSEM results as used for pixel-wise calibration (figure 7.2 a, b, d, e) and as used for voltage distribution analysis (7.2 c, f). The calibration images have the same contrast everywhere in the samples, apart from the topographic and edge effects of the SEM. The measured voltage distribution images show a clear transition in contrast between both leads (dark representing the high potential). Figure 7.3 gives the corresponding analytical model, FEM simulations and experimentally determined voltages, showing good qualitative correspondence. The quantitative comparison shows that the VCSEM results are off by approximately 0.4 V for the opposite sample at the leads (which is around 20 %) and approximately 1.0 V for the parallel sample at the leads (which is around 10 %). The results show almost isotropic conduction in the samples, due to a low contact resistance.

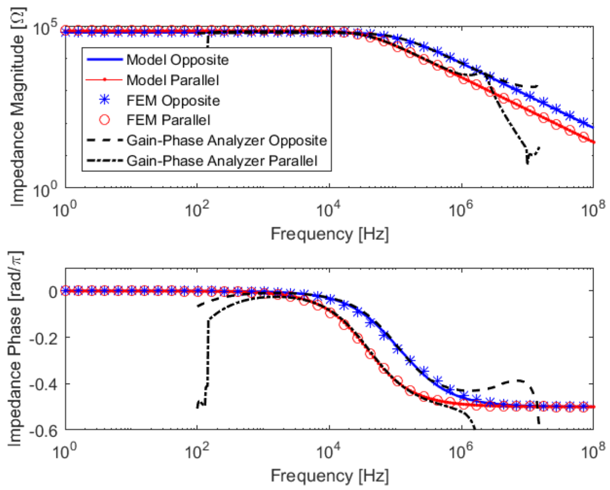

Figure 7.1: Impedance and phase data of the FEM simulations in comparison with the gain-phase measurements.

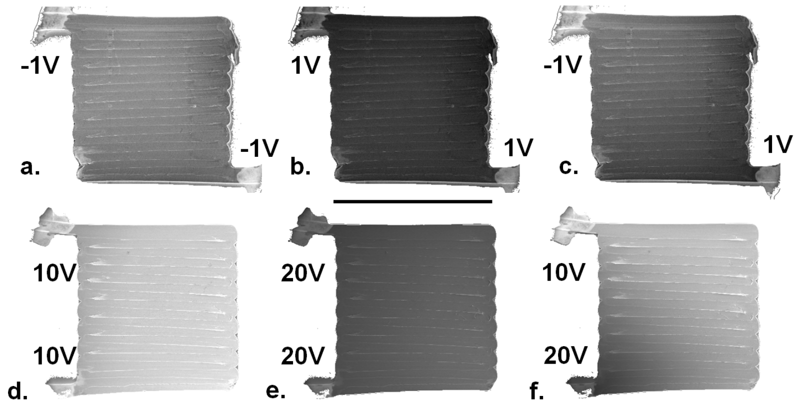

Figure 7.2: VCSEM results with constant voltage images for calibration (a, b, d, e) and the contrast of a measured voltage distribution (c, f) of the opposite lead (fig 1.a) and parallel lead sample (fig 1.b). The central bar indicates 15 mm.

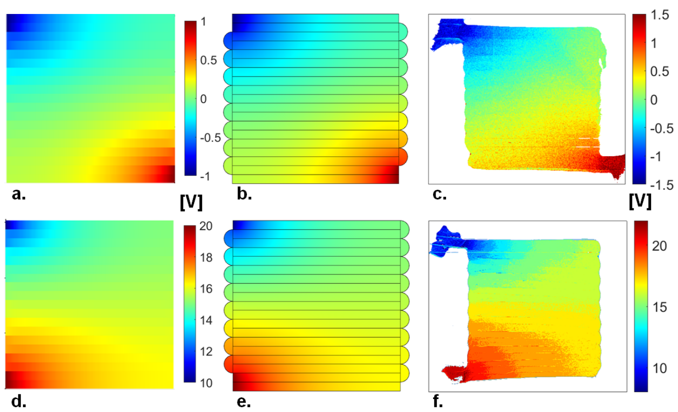

Figure 7.3: VCSEM DC voltage distribution according to the model (a,d), FEM simulations (b,e) and as determined with VCSEM (c,f) for same side and opposite side leads samples.

7.4 IR Thermography Measurements

Figure 7.4 shows the dissipated power density in the analytical model (a,d) and in the FEM simulations (b,e) compared to the measured thermal images with temperatures ranging from 24 °C to 32 °C. From these images it becomes clear that the model and simulations have very high power density at the direct connection to the leads (where the analytical model and FEM simulations give comparable results). In the case of the temperature distribution the gradients are a lot lower and the heating is spread out more evenly, which is expected to be due to thermal conduction. To give a better view of the model and simulation results, the plotted colour range is limited to a maximum value (to make the power density pattern more clear). The result is shown in figure 7.5, where comparable patterns are found with the (unfiltered) measurement data. In both the model and simulations heating along the meanders is found, this is not seen in the measurement data. This could be because of the small features, which can be averaged out by thermal conduction and the camera resolution. The hot spots around the leads occur for all cases, where the conduction path between the leads also corresponds for the several cases. The thermal measurements still show quite some spread of the temperatures compared to the calculated power dissipation. Most likely the high heat capacity of the glass wafer in combination with the thermal conductivity of the eTPU yield this result.

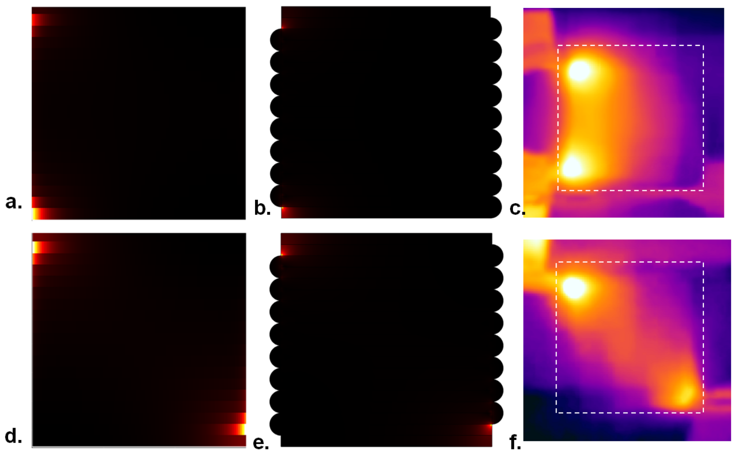

Figure 7.4: Infrared Thermography lock-in measurement data with almost isotropic samples. For these measurements 50 V driving was used at a frequency of 0.02 Hz.

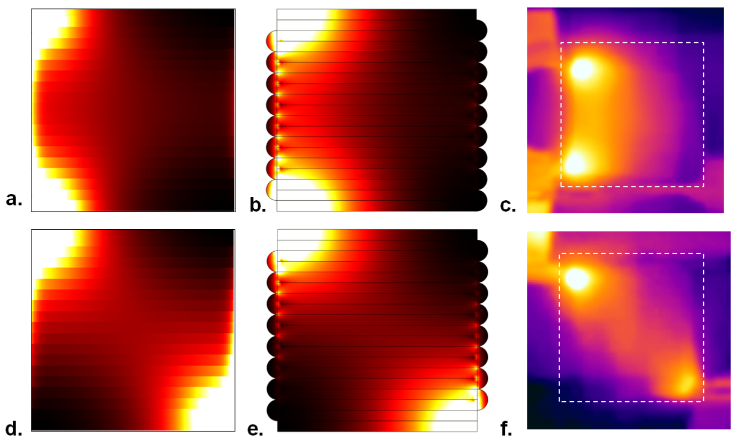

Figure 7.5: Infrared Thermography lock-in measurement with almost isotropic samples. For these measurements 50 V driving was used at a frequency of 0.02 Hz. The plotting intensity in the model and simulations are limited to a maximum for a better comparison to the thermal measurements.

7.5 Conclusion

The global electrical measurements are performed and the model and simulation parameters are fitted to this experimental data. Obtaining proper data from both LCR and gain-phase measurements is still difficult, for which the reason is still unclear.

Results from the VCSEM measurements show a good qualitative correspondence to the model and simulations. Quantitatively the biggest errors are respectively 20 % and 10 % for the opposite and parallel sample, which is quite good for measurements without an energy spectrometer.

The modelled and simulated power dissipation values show peak values at the leads, whereas the thermal distribution is more spread out by thermal diffusion. By limiting the maximum plotted model and simulation values, the modelled power dissipation has more resemblance to the temperature measurements. In reality sharp gradients of power dissipation are smoothed by thermal diffusion, giving rise to hot spots instead of sharp peaks in the thermal distribution. This effect makes it difficult to compare the modelled power dissipation to thermal measurements without adjusting the plot range of the model and simulations.

The measurement methods, modelling and FEM results correspond well with each other. The fitted values from the global electrical measurements give good results in the modelling of the VCSEM and IR thermography measurements (the permittivity and contact capacitance fits should still be checked with high frequency measurements). From the measurements it becomes clear that the samples are almost of an isotropic electrical nature. Some anisotropy can be recognized in the VCSEM voltage distributions with the voltage extending more in-line with the traxels. For future work it would be interesting to study the model and methods with anisotropic samples.

8 Discussion and Conclusion

3D-printing of conductive structures is an upcoming research area, where it has been shown that he 3D-printing process affects the electrical properties of conductive samples. Therefore to fully understand the resulting anisotropic electrical properties, new methods of modelling and measuring are required for predictions and characterization of 3D-printed samples. This research focuses on analytical modelling of 3D-printed conductive sheets and measuring of the anisotropic electrical properties by means of the voltage contrast method in SEM and IR thermography. The following research question which is studied and is split in several subquestions:
"How can the anisotropic, electrical characteristics of 3D-printed, conductive structures be modelled and determined?".

The first subquestion concerns the modelling aspect:
"How can the electrical characteristics of 3D printed conductive structures be modelled, to gain a deeper understanding?"
To model the anisotropic electrical properties a system of partial differential equations has been derived based on the combination of bulk and contact properties in and between traxels (track elements). An eigenvalue expansion method has been used to solve the model and to calculate the voltages and currents. With the model it could be shown that three possible different conduction modes exist in meandering sheets. The conduction mode of a sample depends on the relative importance of the contact impedance, the three different possibilities are conduction through: the traxels, through the bulk and a mix of both. The model is verified by FEM simulations and corresponds well. The main differences occur due to the simplified meandering bends in the model. Experimental methods are required for validation of the physical model.

The second subquestion covers techniques for measuring the electrical characteristics:
"How can the electrical characteristics of 3D printed conductive structures be measured experimentally? "
A conductive polymer composite of TPU with carbon black particles is used for the experiments. The electrical conduction in this material can be explained by percolation theory with quantum-mechanical junction tunneling. A series micro-capacitor model is used to describe the AC electrical properties of the material. This is a simplification that does not reflect the physics properly, however it captures all necessary behaviour. Dielectric impedance spectroscopy is subsequently used to measure the electrical impedance of samples. The ohmic behaviour of the material is shown and the resistivity and permittivity are determined through the RC-model. Measurements and fitted RC-model results fit rather well, however the found permittivity value of the material is high compared to literature. This might be explained from the simplifications in the RC-model.

Samples for the experiments are fabricated with FDM, which gives rise to the electrical interfaces. The nature of these electrical interfaces is unclear. Possible explanations are improper traxel fusion, voids and an inhomogeneous carbon black distribution. Furthermore analysis shows that the actual contact geometry is dissimilar from the modelled geometry, yielding fitted contact resistivity and capacitance values that do not match reality. A better measurement method and understanding of the electrical contacts needs to be developed.

The voltage contrast SEM method has been used to study voltage distributions during operation. Through pixel-wise calibration and curve fitting the voltage distribution can be determined from intensity images of samples. Qualitative voltage measurements can be performed properly. For the performed quantitative measurements errors of 10 % to 20 % with respect to the actual voltages are reported, which is likely due to micro and macro electric fields inside the SEM. To reduce the effect of electric fields inside the SEM chamber on quantitative measurements, the use of an energy spectrometer is required. Furthermore VCSEM measurements at higher frequencies are proposed theoretically by using the nonlinear relation between the voltage and detected intensity. Additional improvements can be made if artifacts like charging and topography can be reduced.

IR thermography has been studied in combination with Joule heating to measure the power dissipation in samples. A lumped thermal model is compared to the measurement results, giving corresponding qualitative results. Quantitatively it is difficult to model the heating because of the difficult thermal boundary conditions. A frequency analysis of the temperature of the harmonically heated sample, called lock-in thermography, can be used to improve the measurements. Amplitude modulation combined with lock-in thermography is proposed to measure the temperature distribution at higher sample frequencies. Furthermore improvements of the modelling and measurements are required to have improved quantitative results.

The final subquestion treats the combination of the modelling and measurement techniques:
"Do results of experimentally determined electrical characteristics of 3D-printed conductors validate the analytical models?"
The developed modelling and measurement methods are applied to two samples. The modelling parameters are fitted to the impedance spectroscopy data. VCSEM and IR thermography show voltage distributions and power dissipation distributions that are consistent with each other (as is also shown with the paper sample in appendix E). The outcomes show that qualitative measurements at low frequencies can be performed. Measurements at higher frequencies with VCSEM and IR thermography still need to be implemented and tested to be able to study the conduction modes over a large frequency range. When this is possible, the model can be validated over its entire range instead of just at the low frequencies. The results from the low frequency measurements are described in a conference abstract and will be presented at the IEEE International Conference on Flexible and Printable Sensors and Systems 2019 (appendix H).

In conclusion a modelling method and characterization methods have been presented to predict and measure the electrical properties of 3D-printed conductors. It is shown that modelling and experiments correspond well and can therefore be used alongside each other. The methods can be used to enable improvement of 3D-printed transducer design and exploit electrical properties of 3D-printed conductors.

8.1 Recommendations

Several recommendations can be made on the basis of the findings of this research. In the modelling and measurement chapters the specific improvements for the respective characterization method are mentioned. More general recommendations for the electrical characterization of anisotropic, 3D-printed conductive sheets are:

- <u>3D-Modelling</u>: The eigenmode/eigenvector model can be extended to 3 dimensions for modelling of rectangular prism-shaped samples (for the validation of this model and measurements on these samples a different characterization approach is necessary, since VCSEM and IR thermography perform surface measurements).
- <u>Multiphysics Effects</u>: By including thermal effects in the modelling procedure, the model can be made more accurate. The eigenmode/eigenvector model might be able to describe the anisotropic thermal conduction through the sample through the analogy between electrical and thermal systems (the main heating occurs directly at the voltage

input, this can also be done to approximate the thermal input). A real multiphysics coupling between the electrical and thermal domain is not possible since the model does not support locally varying properties (e.g. locally increased resistivity by increased temperature). By assuming a fixed resistivity, the temperature distribution as a result of the electrical heating can possibly be modelled.

- Material Behaviour: Additional research on the electrical properties of carbon black doped polymers can improve the experimentally determined electrical parameters and the coupling between the modelling and the measurements. Improved models like the transmission line model and possibly correcting the RC-model (which assumes similar areas between carbon black for quantum tunneling and capacitance effects).
- High Frequency Measurements: The proposed methods for high frequency measurements can be implemented to measure conduction modes and validate the model at higher frequencies. For VCSEM this entails calibrating and measuring the intensity from AC signals without bias voltage and with changing amplitude. For IR thermography the method of lock-in thermography combined with amplitude modulation can be implemented.
- Fabrication Effects: The effect of the printing parameters on the electrical characteristics still needs to be studied thoroughly. Parameters like the extrusion factor, extrusion width and overlap percentage can be studied to actively tailor the electrical contact properties.
- Transducer Design: The characterization methods should be used for improving 3D-printed transducers. A feasible use case is the improvement of a capacitive force sensor based on the electrical anisotropy in 3D-printed structures like studied by Wolterink (13).

Bibliography

[1] Y. Xu, X. Wu, X. Guo, B. Kong, M. Zhang, X. Qian, S. Mi, and W. Sun, “The boom in 3d-printed sensor technology,” *Sensors*, vol. 17, no. 5, 2017.

[2] G. Krijnen, A. Dijkshoorn, P. Werkman, M. Welleweerd, G. Wolterink, B. Eijking, J. Delamare, and R. Sanders, “Embedded sensing: Integrating sensors in 3-d printed structures,” *Journal of Sensors and Sensor Systems*, vol. 7, no. 1, pp. 169–181, 2018.

[3] S. Kwok, K. Goh, Z. Tan, S. Tan, W. Tjiu, J. Soh, Z. Ng, Y. Chan, H. Hui, and K. Goh, “Electrically conductive filament for 3d-printed circuits and sensors,” *Applied Materials Today*, vol. 9, pp. 167–175, 2017.

[4] S. Leigh, R. Bradley, C. Purssell, D. Billson, and D. Hutchins, “A simple, low-cost conductive composite material for 3d printing of electronic sensors,” *PLoS ONE*, vol. 7, no. 11, 2012.

[5] K. Gnanasekaran, T. Heijmans, S. van Bennekom, H. Woldhuis, S. Wijnia, G. de With, and H. Friedrich, “3d printing of cnt- and graphene-based conductive polymer nanocomposites by fused deposition modeling,” *Applied Materials Today*, vol. 9, pp. 21 – 28, 2017.

[6] Voxel8, “Multi-Material Digital Manufacturing.” http://www.voxel8.com. [Online; accessed 05-March-2019].

[7] Wikipedia, “Fused deposition modeling — Wikipedia, the free encyclopedia.” http://nl.wikipedia.org/w/index.php?title=Fused%20deposition%20modeling&oldid=51709861, 2019. [Online; accessed 05-March-2019].

[8] Palmiga Innovation, “I-etpu 95-250 carbon black the conductive and flexible 3d printing filament..” https://rubber3dprinting.com/pi-etpu-95-250-carbon-black/, 2016. [Online; accessed 05-March-2019].

[9] Proto-pasta, “Conductive pla.” https://www.proto-pasta.com/pages/conductive-pla, 2016. [Online; accessed 05-March-2019].

[10] H. Watschke, K. Hilbig, and T. Vietor, “Design and characterization of electrically conductive structures additively manufactured by material extrusion,” *Applied Sciences (Switzerland)*, vol. 9, no. 4, 2019.

[11] J. Zhang, B. Yang, F. Fu, F. You, X. Dong, and M. Dai, “Resistivity and its anisotropy characterization of 3d-printed acrylonitrile butadiene styrene copolymer (abs)/carbon black (cb) composites,” *Applied Sciences (Switzerland)*, vol. 7, no. 1, 2017.

[12] M. Dawoud, I. Taha, and S. Ebeid, “Strain sensing behaviour of 3d printed carbon black filled abs,” *Journal of Manufacturing Processes*, vol. 35, pp. 337–342, 2018.

[13] G. Wolterink, R. Sanders, and G. Krijnen, “Thin, flexible, capacitive force sensors based on anisotropy in 3d-printed structures,” 10 2018. IEEE Sensors 2018 ; Conference date: 28-10-2018 Through 31-10-2018.

[14] P. Flowers, C. Reyes, S. Ye, M. Kim, and B. Wiley, “3d printing electronic components and circuits with conductive thermoplastic filament,” *Additive Manufacturing*, vol. 18, pp. 156–163, 2017.

[15] B. Hampel, S. Monshausen, and M. Schilling, “Properties and applications of electrically conductive thermoplastics for additive manufacturing of sensors,” *Technisches Messen*, vol. 84, no. 9, pp. 593–599, 2017.

[16] G. Wolterink, R. Sanders, F. Muijzer, B. van Beijnum, and G. Krijnen, “3d-printing soft semg sensing structures,” in *2017 IEEE SENSORS*, pp. 1–3, Oct 2017.

[17] C. Dos Santos, A. De Campos, M. Da Luz, B. White, J. Neumeier, B. De Lima, and C. Shigue, “Procedure for measuring electrical resistivity of anisotropic materials: A revi-

sion of the montgomery method," *Journal of Applied Physics*, vol. 110, no. 8, 2011.

[18] M. Tokarska and K. Gniotek, "Anisotropy of the electrical properties of flat textiles," *Journal of the Textile Institute*, vol. 106, no. 1, pp. 9–18, 2015.

[19] I. Kazani, G. de Mey, C. Hertleer, J. Banaszczyk, A. Schwarz, G. Guxho, and L. Van Langenhove, "Van der pauw method for measuring resistivities of anisotropic layers printed on textile substrates," *Textile Research Journal*, vol. 81, no. 20, pp. 2117–2124, 2011.

[20] S. Nonn, M. Schagerl, Y. Zhao, S. Gschossmann, and C. Kralovec, "Application of electrical impedance tomography to an anisotropic carbon fiber-reinforced polymer composite laminate for damage localization," *Composites Science and Technology*, vol. 160, pp. 231–236, 2018.

[21] J. Cagan, "Hardware implementation of electrical resistance tomography for damage detection of carbon fibreÃćâĆňâĂIJreinforced polymer composites," *Structural Health Monitoring*, vol. 16, no. 2, pp. 129–141, 2017.

[22] H. Lee, D. Kwon, H. Cho, I. Park, and J. Kim, "Soft nanocomposite based multi-point, multi-directional strain mapping sensor using anisotropic electrical impedance tomography," *Scientific Reports*, vol. 7, 2017.

[23] M. Naidjate, B. Helifa, M. Feliachi, I.-K. Lefkaier, H. Heuer, and M. Schulze, "A smart eddy current sensor dedicated to the nondestructive evaluation of carbon fibers reinforced polymers," *Sensors (Switzerland)*, vol. 17, no. 9, 2017.

[24] X.-J. Xu, H.-I. Ji, J.-H. Qiu, and T. Takagi, "Effects of interlamianr electrical behavior on eddy currents in carbon fiber composite materials," pp. 133–137, 2018.

[25] G. Krukowski, S. Gratkowski, and R. Sikora, *Imaging of Two-Dimensional Current Density Distributions from Their Magnetic Field.* Springer, 2005.

[26] P. Girard, "VOLTAGE CONTRAST," *Journal de Physique IV Colloque*, vol. 01, no. C6, pp. C6–259–C6–270, 1991.

[27] H. Bui, F. Senghor, G. Wasselynck, D. Trichet, J. Fouladgar, K. Lee, and G. Berthiau, "Characterization of electrical conductivity of anisotropic cfrp materials by means of induction thermography technique," *IEEE Transactions on Magnetics*, vol. 54, no. 3, 2018.

[28] J. Banaszczyka, A. Anca, and G. De Mey, "Infrared thermography of electroconductive woven textiles," *Quantitative InfraRed Thermography Journal*, vol. 6, no. 2, pp. 163–173, 2009.

[29] N. Athanasopoulos and V. Kostopoulos, "A comprehensive study on the equivalent electrical conductivity tensor validity for thin multidirectional carbon fibre reinforced plastics," *Composites Part B: Engineering*, vol. 67, pp. 244 – 255, 2014.

[30] S. Spallek, *Electron Microscopy Studies on Structure-property Relationships of Nanoparticulate Transparent Electrodes for Printed Electronics.* PhD thesis, Friedrich-Alexander-Universität, Erlangen-Nürnberg, 1 2016.

[31] R. Rosenkranz, "Failure localization with active and passive voltage contrast in fib and sem," *Journal of Materials Science: Materials in Electronics*, vol. 22, no. 10, pp. 1523–1535, 2011.

[32] M. Neruda, *Modelling of electrical resistivity for electrically conductive textile materials.* PhD thesis, Czech Technical University in Prague,Faculty of Electrical Engineering, Department of Telecommunication Engineering, Prague, 2 2014.

[33] E. Gunnarsson, M. Karlsteen, L. Berglin, and J. Stray, "A novel technique for direct measurements of contact resistance between interlaced conductive yarns in a plain weave," *Textile Research Journal*, vol. 85, no. 5, pp. 499–511, 2015.

[34] M. Tokarska and M. Orpel, "Study of anisotropic electrical resistance of knitted fabrics," *Textile Research Journal*, vol. 89, no. 6, pp. 1073–1083, 2019.

[35] N. Athanasopoulos and V. Kostopoulos, "Calculation of an equivalent electrical conductivity tensor for multidirectional carbon fiber reinforced materials," pp. 1013–1018, 2012.

[36] A. Todoroki, "Electric current analysis of cfrp using perfect fluid potential flow," *Transactions of the Japan Society for Aeronautical and Space Sciences*, vol. 55, no. 3, pp. 183–190, 2012.

[37] K. Almuhammadi, T. Bera, and G. Lubineau, "Electrical impedance spectroscopy for measuring the impedance response of carbon-fiber-reinforced polymer composite laminates," *Composite Structures*, vol. 168, pp. 510–521, 2017.

[38] P. Dias, "Development of pi-etpu based sensors for prosthesis control," September 2018. University of Twente, MSc-thesis.

[39] N. Athanasopoulos, *Calculation of electrical conductivity and electrothermal analysis of multilayered carbon reinforced composites: application to damage detection.* PhD thesis, University of Patras, Patras, Feb 2013.

[40] W. Yi, Y. Wang, G. Wang, and X. Tao, "Investigation of carbon black/silicone elastomer/dimethylsilicone oil composites for flexible strain sensors," *Polymer Testing*, vol. 31, no. 5, pp. 677–684, 2012.

[41] K. Kim, J. Park, J.-H. Suh, M. Kim, Y. Jeong, and I. Park, "3d printing of multiaxial force sensors using carbon nanotube (cnt)/thermoplastic polyurethane (tpu) filaments," *Sensors and Actuators, A: Physical*, vol. 263, pp. 493–500, 2017.

[42] J. Christ, N. Aliheidari, P. Pötschke, and A. Ameli, "Bidirectional and stretchable piezoresistive sensors enabled by multimaterial 3d printing of carbon nanotube/thermoplastic polyurethane nanocomposites," *Polymers*, vol. 11, no. 1, 2018.

[43] D. Zhang, B. Chi, B. Li, Z. Gao, Y. Du, J. Guo, and J. Wei, "Fabrication of highly conductive graphene flexible circuits by 3d printing," *Synthetic Metals*, vol. 217, pp. 79–86, 2016.

[44] Black Magic 3D, "Conductive graphene pla filament 100g." http://www.blackmagic3d.com/Conductive-p/grphn-pla.htm, 2017. [Online; accessed 05-March-2019].

[45] J. McGhee, M. Sinclair, D. Southee, and K. Wijayantha, "Strain sensing characteristics of 3d-printed conductive plastics," *Electronics Letters*, vol. 54, no. 9, pp. 570–572, 2018.

[46] M. Darnis, "Integrating sensors in components using additive manufacturing," 2 2016. Hochschule Esslingen, MSc thesis.

[47] B. Eijking, R. Sanders, and G. Krijnen, "Development of whisker inspired 3d multimaterial printed flexible tactile sensors," in *2017 IEEE SENSORS*, pp. 1–3, Oct 2017.

[48] M. Schouten, "Towards additively manufactured complex robotic systems," December 2017. University of Twente, MSc-thesis.

[49] M. Schouten, R. Sanders, and G. Krijnen, "3d printed flexible capacitive force sensor with a simple micro-controller based readout," vol. 2017-December, pp. 1–3, 2017.

[50] C. Manganiello, D. Naso, F. Cupertino, O. Fiume, and G. Percoco, "Investigating the potential of commercial-grade carbon black-filled tpu for the 3d printing of compressive sensors," *Micromachines*, vol. 10, no. 1, 2019.

[51] M. E. Spahr, R. Gilardi, and D. Bonacchi, *Carbon Black for Electrically Conductive Polymer Applications*, pp. 1–20. Berlin, Heidelberg: Springer Berlin Heidelberg, 2021.

[52] N. Stübler, J. Fritzsche, and M. Klüppel, "Mechanical and electrical analysis of carbon black networking in elastomers under strain," *Polymer Engineering and Science*, vol. 51, no. 6, pp. 1206–1217, 2011.

[53] H. Deng, L. Lin, M. Ji, S. Zhang, M. Yang, and Q. Fu, "Progress on the morphological control of conductive network in conductive polymer composites and the use as electro-

active multifunctional materials," *Progress in Polymer Science*, vol. 39, no. 4, pp. 627–655, 2014.

[54] M. Kupke, "Electrically conductive glass fibre reinforced epoxy resin," *Materials Research Innovations*, vol. 2, no. 3, pp. 164–169, 1998.

[55] E.-C. Shin, H.-H. Seo, J.-H. Kim, P.-A. Ahn, S. Park, Y. Lim, S. Kim, C. Kim, D. Kim, C. Hong, G. Seo, and J.-S. Lee, "A new diagnostic tool for the percolating carbon network in the polymer matrix," *Polymer*, vol. 54, no. 3, pp. 999–1003, 2013.

[56] J.-C. Huang, "Carbon black filled conducting polymers and polymer blends," *Advances in Polymer Technology*, vol. 21, no. 4, pp. 299–313, 2002.

[57] G. Ouyang, "On immittance spectroscopy for carbon black network characterization," *KGK-Kautschuk und Gummi Kunststoffe*, vol. 55, no. 3, pp. 104–113, 2002.

[58] J. Meier, J. Mani, and M. Klüppel, "Analysis of carbon black networking in elastomers by dielectric spectroscopy," *Physical Review B - Condensed Matter and Materials Physics*, vol. 75, no. 5, 2007.

[59] E. Sichel, J. Gittleman, and P. Sheng, "Electrical properties of carbon-polymer composites," *Journal of Electronic Materials*, vol. 11, no. 4, pp. 699–747, 1982.

[60] A. Mdarhri, C. Brosseau, M. Zaghrioui, and I. El Aboudi, "Electronic conduction and microstructure in polymer composites filled with carbonaceous particles," *Journal of Applied Physics*, vol. 112, no. 3, 2012.

[61] J. Xu, M. Wong, and C. Wong, "Super high dielectric constant carbon black-filled polymer composites as integral capacitor dielectrics," vol. 1, pp. 536–541, 2004.

[62] E. Asare, J. Evans, M. Newton, T. Peijs, and E. Bilotti, "Effect of particle size and shape on positive temperature coefficient (ptc) of conductive polymer composites (cpc) - a model study," *Materials and Design*, vol. 97, pp. 459–463, 2016.

[63] Y. Liu, H. Zhang, H. Porwal, J. Busfield, T. Peijs, and E. Bilotti, "Pyroresistivity in conductive polymer composites: a perspective on recent advances and new applications," *Polymer International*, vol. 68, no. 3, pp. 299–305, 2019.

[64] H. Tang, X. Chen, and Y. Luo, "Studies on the ptc/ntc effect of carbon black filled low density polyethylene composites," *European Polymer Journal*, vol. 33, no. 8, pp. 1383–1386, 1997.

[65] H. Xu, Y. Wu, D. Yang, J. Wang, and H. Xie, "Study on theories and influence factors of ptc property in polymer-based conductive composites," *Reviews on Advanced Materials Science*, vol. 27, no. 2, pp. 173–183, 2011.

[66] C. Nieves, I. Ramos, N. Pinto, and N. Zimbovskaya, "Electron transport mechanisms in polymer-carbon sphere composites," *Journal of Applied Physics*, vol. 120, no. 1, 2016.

[67] J. Zhang, S. Feng, and X. Wang, "Dc current voltage characteristics of silicone rubber filled with conductive carbon black," *Journal of Applied Polymer Science*, vol. 94, no. 2, pp. 587–592, 2004.

[68] M. Alzamil, K. Alfaramawi, S. Abboudy, and L. Abulnasr, "Electrical conduction hysteresis in carbon black-filled butyl rubber compounds," *International Journal of Modern Physics B*, vol. 32, no. 9, 2018.

[69] Electrolube, "Silver conductive paint." https://www.electrolube.com/products/maintenance-service-aids/scp/paints_and_paint_removers/. [Online; accessed 05-March-2019].

[70] Keysight Technologies, *Impedance Measurement Handbook: A guide to measurement technology and techniques*. Keysight Technologies, 6 ed., 2016.

[71] M. Schönleber, D. Klotz, and E. Ivers-Tiffee, "A method for improving the robustness of linear kramers-kronig validity tests," *Electrochimica Acta*, vol. 131, pp. 20–27, 2014.

[72] B. Boukamp, "A linear kronig-kramers transform test for immittance data validation," *Journal of the Electrochemical Society*, vol. 142, no. 6, pp. 1885–1901, 1995.

[73] M. Schönleber and E. Ivers-Tiffee, "Approximability of impedance spectra by rc elements and implications for impedance analysis," *Electrochemistry Communications*, vol. 58, pp. 15–19, 2015.

[74] m. Schönleder, "Kramers-kronig validity test lin-kk for impedance spectra." https://www.iam.kit.edu/wet/english/Lin-KK.php, 12 2015. [Online; accessed 05-March-2019].

[75] J. I. Goldstein and H. Yakowitz, *Practical Scanning Electron Microscopy: Electron and Ion Microprobe Analysis.* 01 1975.

[76] R. Hafer, O. Patterson, R. Hahn, and H. Xiao, "Full-wafer voltage contrast inspection for detection of beol defects," *IEEE Transactions on Semiconductor Manufacturing*, vol. 28, no. 4, pp. 461–468, 2015.

[77] W. Li, S. Buschhorn, K. Schulte, and W. Bauhofer, "The imaging mechanism, imaging depth, and parameters influencing the visibility of carbon nanotubes in a polymer matrix using an sem," *Carbon*, vol. 49, no. 6, pp. 1955–1964, 2011.

[78] A. Vladar, "Strategies for scanning electron microscopy sample preparation and characterization of multiwall carbon nanotube polymer composites," *NIST Pubs*, no. 1200-17, 2015.

[79] A. Vijayaraghavan, M. Timmermans, K. Grigoras, A. Nasibulin, E. Kauppinen, and R. Krupke, "Imaging conduction pathways in carbon nanotube network transistors by voltage-contrast scanning electron microscopy," *Nanotechnology*, vol. 22, no. 26, 2011.

[80] W. Li and W. Bauhofer, "Imaging of cnts in a polymer matrix at low accelerating voltages using a sem," *Carbon*, vol. 49, no. 12, pp. 3891–3898, 2011.

[81] Y. Liu, X. Zhou, J. Carr, C. Butler, S. Mills, J. O'Connor, E. McAlpine, T. Hashimoto, X. Zhong, G. Thompson, G. Scamans, P. Howe, M. McCool, and N. Malone, "Visualisation of conductive filler distributions in polymer composites using voltage and energy contrast imaging in sem," *Polymer*, vol. 54, no. 1, pp. 330–340, 2013.

[82] A. Vijayaraghavan, S. Blatt, C. Marquardt, S. Dehm, R. Wahi, F. Hennrich, and R. Krupke, "Imaging electronic structure of carbon nanotubes by voltage-contrast scanning electron microscopy," *Nano Research*, vol. 1, pp. 321–332, Oct 2008.

[83] JEOL, "Scanning electron microscope a to z." https://www.jeol.co.jp/en/applications/detail/891.html. [Online; accessed 05-March-2019].

[84] J. Goldstein, D. E. Newbury, J. Michael, N. Ritchie, J. Henry J. Scott, and D. C. Joy, *Scanning Electron Microscopy and X-Ray Microanalysis.* 01 2018.

[85] B. Hafner, "Scanning electron microscopy primer." http://www.charfac.umn.edu/sem_primer.pdf, 2007. CharFac University of Minnesota.

[86] Hitachi, "Signal detection." https://www.utoledo.edu/engineering/cmsc/pdfs/SEM%20Workshop%20presentation%202.pdf. [Online; accessed 23-May-2019].

[87] D. C. Joy, *Noise and Its Effects on the Low-Voltage SEM*, pp. 129–144. New York, NY: Springer New York, 2008.

[88] J. Frank and L. Al-Ali, "Signal-to-noise ratio of electron micrographs obtained by cross correlation," *Nature*, vol. 256, no. 5516, pp. 376–379, 1975.

[89] N. Marturi, S. Dembélé, and N. Piat, "Performance Evaluation of Scanning Electron Microscopes using Signal-to-Noise Ratio.," in *The 8th International Workshop on Micro-Factories, IWMF'12.*, vol. sur CD ROM, (Tampere, Finland), pp. 1–6, June 2012.

[90] V. Dyukov, S. Nepijko, and G. Schönhense, "Voltage contrast modes in a scanning electron microscope and their application," *Advances in Imaging and Electron Physics*, vol. 196, pp. 165–246, 2016.

[91] J. Cazaux, "Material contrast in sem: Fermi energy and work function effects," *Ultramicroscopy*, vol. 110, no. 3, pp. 242–253, 2010.

[92] M. Chung and T. Everhart, "Simple calculation of energy distribution of low-energy secondary electrons emitted from metals under electron bombardment," *Journal of Applied Physics*, vol. 45, no. 2, pp. 707–709, 1974.

[93] L. Reimer, *Scanning Electron Microscopy.* Springer, 2 ed., 1998.

[94] H. Seiler, "Secondary electron emission in the scanning electron microscope," *Journal of Applied Physics*, vol. 54, no. 11, pp. R1–R18, 1983.

[95] K. Nakamae, H. Fujioka, and K. Ura, "Local field effects on voltage contrast in the scanning electron microscope," *Journal of Physics D: Applied Physics*, vol. 14, no. 11, pp. 1939–1960, 1981.

[96] W. Chim, "A novel correction scheme for quantitative voltage contrast measurements using low extraction fields in the scanning electron microscope," *Measurement Science and Technology*, vol. 6, no. 5, pp. 488–495, 1995.

[97] W. E. Wager and E. D. Wolf, "Effects of local electric fields and specimen geometry on voltage contrast in the scanning electron microscope.," *Journal of Vacuum Science and Technology B: Microelectronics and Nanometer Structures*, vol. 4, no. 1, pp. 209–212, 1986.

[98] K. Chung, J. Reisner, and E. Campbell, "Charging phenomena in the scanning electron microscopy of conductor-insulator composites: A tool for composite structural analysis," *Journal of Applied Physics*, vol. 54, no. 11, pp. 6099–6112, 1983.

[99] J. Cazaux, "From the physics of secondary electron emission to image contrasts in scanning electron microscopy," *Journal of Electron Microscopy*, vol. 61, no. 5, pp. 261–284, 2012.

[100] J. Meul, "Study of electro-conductive contacts in hybrid woven fabrics," May 2015. Unversiteit Gent, MSc-thesis.

[101] X. Yao, B. Falzon, and S. Hawkins, "Orthotropic electro-thermal behaviour of highly-aligned carbon nanotube web based composites," *Composites Science and Technology*, vol. 170, pp. 157–164, 2019.

[102] S. Röhrig, I. Petschenig, R. Bermejo, M. Hofstätter, F. Aldrian, R. Danzer, and P. Supancic, "Thermography and complementary measurements as tools to detect micro-irregularities in electronic components," *Journal of Ceramic Science and Technology*, vol. 6, no. 4, pp. 255–260, 2015.

[103] M. Hofstätter, N. Raidl, B. Sartory, and P. Supancic, "Nonlinear lock-in infrared microscopy: A complementary investigation technique for the analysis of functional electroceramic components," *Microscopy and Microanalysis*, vol. 21, no. 5, pp. 1145–1152, 2015.

[104] Unknown, "Thermal-electrical analogy: thermal network." http://www.ingaero.uniroma1.it/attachments/2176_Cap_3%20Thermal-electrical%20analogy.pdf, 2017. [Online; accessed 23-May-2019].

[105] J. Klaessens, A. Van Der Veen, and R. Verdaasdonk, "Comparison of the temperature accuracy between smart phone based and high-end thermal cameras using a temperature gradient phantom," vol. 10056, 2017.

[106] O. Breitenstein, J. Rakotoniaina, M. Al Rifai, M. Gradhand, F. Altmann, and T. Riediger, “New developments in ir lock-in thermography,” pp. 595–599, 2004.

[107] W. Commons, “File:amplitude modulated wave-hm-64.svg — wikimedia commons, the free media repository,” 2017. [Online; accessed 23-May-2019].

[108] I. Konvalina and I. Müllerova, “The trajectories of secondary electrons in the scanning electron microscope,” *Scanning*, vol. 28, no. 5, pp. 245–256, 2006.

[109] N. Kurra and G. Kulkarni, “Pencil-on-paper: Electronic devices,” *Lab on a Chip*, vol. 13, no. 15, pp. 2866–2873, 2013.

[110] C.-W. Lin, Z. Zhao, J. Kim, and J. Huang, “Pencil drawn strain gauges and chemiresistors on paper,” *Scientific Reports*, vol. 4, 2014.

[111] T.-K. Kang, “Tunable piezoresistive sensors based on pencil-on-paper,” *Applied Physics Letters*, vol. 104, no. 7, 2014.

[112] Y. Çengel and A. Ghajar, *Heat and Mass Transfer: Fundamentals & Applications*. Asia Higher Education Engineering/Computer Science Mechanical Engineering, McGraw-Hill Education, 2015.

A Continuum Model

For large prints a continuum model can be applied. This model is based on homogenization of the electrical properties by combining the bulk and contact properties in a global anisotropic conductivity tensor. These so-called equivalent electrical conductivity tensors are already being used in the field of composites (29; 35; 36; 39). Such a model is only suited for large prints without meanders, since the tensor values need to be the same everywhere (and meanders would locally yield different conductivity).

Derivation

The model can be derived from Ohm's law and the Maxwell equations, with Ohm's law in vector form being (with σ being a tensor for anisotropic materials):

$$\vec{J} = \sigma \vec{E} \tag{A.1}$$

And the equation for conservation of charge without an internal source (for time-independent problems):

$$\nabla \cdot \vec{J} = 0 \tag{A.2}$$

Combining these two equations yields (and using the relation between electric field and potential: $\vec{E} = -\nabla\phi$):

$$\nabla \cdot (\sigma \vec{E}) = -\nabla \cdot (\sigma \nabla \phi) = 0 \tag{A.3}$$

By assuming a constant σ and a 2D situation one obtains:

$$\sigma_x \frac{\partial^2 \phi}{\partial x^2} + \sigma_y \frac{\partial^2 \phi}{\partial y^2} = 0 \tag{A.4}$$

Assuming the conductivity and hence current in the x and y direction are independent of each other, one can apply the method of separation of variables. The potential is then defined as a multiplication of a function depending on x and a function depending on y:

$$\phi = X(x)Y(y) \tag{A.5}$$

Substituting this into equation A.4:

$$\sigma_x X''Y + \sigma_y XY'' = 0 \tag{A.6}$$

Separating variables, one obtains:

$$\sigma_x \frac{X''}{X} = -\sigma_y \frac{Y''}{Y} = \lambda \tag{A.7}$$

Where the two expressions have been set equal to the constant λ because they are functions of the independent variables x and y, and the only way these can be equal is if they are both constants. This yields two ODE's:

$$\sigma_x X'' - \lambda_x X = 0 \text{ and } \sigma_y Y'' + \lambda_y Y = 0 \tag{A.8}$$

The general solution of equation X becomes:

$$X(x) = c_1 \cos(\sqrt{\lambda_x} x) + c_2 \sin(\sqrt{\lambda_x} x) \tag{A.9}$$

With c_1 and c_2 arbitrary constants. The general solution of Y then becomes:

$$Y(y) = c_3 \cosh(\sqrt{\lambda_y} y) + c_4 \sinh(\sqrt{\lambda_y} y) = c_5 e^{\sqrt{\lambda_y} y} + c_6 e^{-\sqrt{\lambda_y} y} \tag{A.10}$$

The potential then becomes:

$$\phi(x, y) = \left(c_1 \cos(\sqrt{\lambda_x} x) + c_2 \sin(\sqrt{\lambda_x} x)\right) * \left(c_5 e^{\sqrt{\lambda_y} y} + c_6 e^{-\sqrt{\lambda_y} y}\right) \tag{A.11}$$

With the boundary conditions of a sample the coefficients can then be determined. It is difficult with this method to analytically solve for boundary conditions on individual traxels (requiring large fourier series solutions to represent steps in potentials). An example of what the full outcome may look like is shown in figure A.1, where a FEM simulation of the voltage distribution in a continuous solid with anisotropic conductivity can be seen.

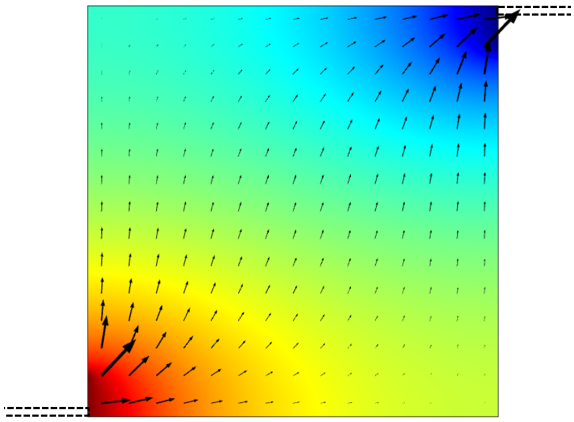

Figure A.1: A FEM simulation of the voltage distribution as example of conduction through a continuous solid with anisotropic conductivity. The current leads are indicated with dotted lines.

B Equivalent Impedance Combined Contact and Bulk Properties

In this chapter the total impedance of the equivalent model for the circuit in figure 2.7 is derived. The goal is to obtain a single equivalent impedance as shown in figure B.1. For a single parallel RC-element the impedance becomes:

$$\hat{Z}_{\text{RC-parallel}} = \frac{1}{\frac{1}{R} + j\omega C} = \frac{R}{1 + \omega RC} \tag{B.1}$$

The circuit in figure 2.7 contains three of the elements in series (with subscript b for bulk properties and c for contact properties), for which the impedance can be found by simple addition (because of linearity the two half terms for the bulk properties can be taken as one fraction, which has to be taken into account with the geometry):

$$\hat{Z}_{\text{eq}} = \frac{R_{\text{b}}}{1 + \omega R_{\text{b}} C_{\text{b}}} + \frac{R_{\text{c}}}{1 + \omega R_{\text{c}} C_{\text{c}}} \tag{B.2}$$

Combining both fractions yields the following expression:

$$\hat{Z}_{\text{eq}} = \frac{R_{\text{b}} + R_{\text{c}} + j\omega R_{\text{b}} R_{\text{c}} C_{\text{c}} + j\omega R_{\text{b}} R_{\text{c}} C_{\text{b}}}{(1 + j\omega R_{\text{b}} C_{\text{b}})(1 + j\omega R_{\text{c}} C_{\text{c}})} \tag{B.3}$$

The bulk resistance and capacitance become different than in section 2.2.1, since we are considering the vertical geometry. The bulk resistance can then be defined as $R_{\text{b}} = \frac{\rho W}{H \Delta x}$, the bulk capacitance is described with $C_{\text{b}} = \frac{\epsilon_0 \epsilon_{\text{r}} H \Delta x}{W}$, the contact resistance is defined as $R_{\text{c}} = \frac{\sigma}{A} = \frac{\sigma}{H \Delta x}$ and finally the contact capacitance can be expressed as $C_{\text{c}} = C_0 H \Delta x$. Substituting these representations yields:

$$\hat{Z}_{\text{eq}} = \frac{\frac{\rho W}{H\Delta x} + \frac{\sigma}{H\Delta x} + j\omega \frac{\rho W}{H\Delta x}\frac{\sigma}{H\Delta x} C_0 H \Delta x + j\omega \frac{\rho W}{H\Delta x}\frac{\sigma}{H\Delta x}\frac{\epsilon_0\epsilon_{\text{r}} H\Delta x}{W}}{(1 + j\omega \frac{\rho W}{H\Delta x}\frac{\epsilon_0\epsilon_{\text{r}} H\Delta x}{W})(1 + j\omega \frac{\sigma}{H\Delta x} C_0 H \Delta x)} \tag{B.4}$$

Combining terms and simplifying finally gives the following result:

$$\hat{Z}_{\text{eq}} = \frac{1}{H\Delta x}\frac{\rho W + \sigma + j\omega\rho\sigma W C_0 + j\omega\rho\sigma\epsilon_0\epsilon_{\text{r}}}{(1 + j\omega\rho\epsilon_0\epsilon_{\text{r}} + j\omega\sigma C_0 - \omega^2\rho\sigma\epsilon_0\epsilon_{\text{r}} C_0} \tag{B.5}$$

Equation B.5 can be used for the derivation of the model in section 2.2.1.

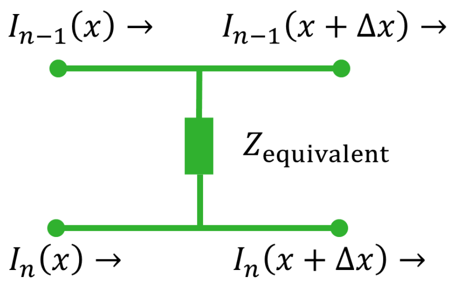

Figure B.1: Equivalent impedance circuit representation for the electrical contact properties combined with the vertical bulk properties of a slice of two neighbouring traxels of Δx wide.

C RC-Area Mismatch

In the RC-model the carbon black particles are assumed to act as conductive parallel plates, whereas they are approximately spherical in reality (figure 3.4). Since the quantum-mechanical junction tunneling relies heavily on the gap distance and the capacitance depends less on the gap density, the plate assumption might cause the overestimation of the permittivity.

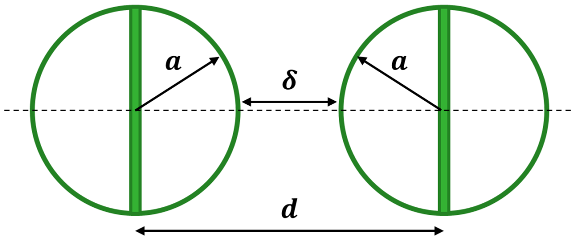

Figure C.1: The spherical carbon black particles, represented as parallel plates in the RC-model.

In figure C.1 the parallel plate model is shown together with the spherical CB particles. To illustrate the problem, values have been assumed for the geometry. Carbon black particles with a radius a of 20 nm with a gap δ between them of 5 nm (based on (58)). The distance d is the distance between the centers of the particles (45 nm). The parallel plates are positioned at the distance d (in the centers). An expression for the electrical resistance between two CB particles with quantum-mechanical junction tunneling is given by (57) for the parallel plates p:

$$R_\mathrm{p} = \frac{U}{JA} = \frac{8\pi^2\hbar}{e^2}\frac{d}{AB\phi^{1/2}}\exp(B\phi^{1/2}d) \tag{C.1}$$

In this equation A is the cross-sectional area for tunneling, $\hbar$ is the Planck constant in eVs, e is the electric charge in C and ϕ is the mean potential barrier height in eV. B can be calculated from $B = 2(2m)^2/\hbar$, where m is the electron mass in kg. A typical potential barrier height is 1 eV (58).

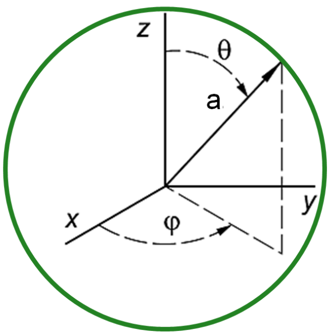

Figure C.2: A description of a point on the sphere by the angles from the point its position vector.

For the parallel plate the distance at every point of the plate to its neighbour is d, for the spheres however the distance depends on the position on the particle. The x-position on the particle can be described by the angles its position vector makes with the axes as shown in figure C.2:

$$x = a\cos(\theta)\cos(\phi) \tag{C.2}$$

The distance between the two spherical particles becomes in this case:

$$\Delta x = 2(a - a\cos(\theta)\cos(\phi)) + \delta \tag{C.3}$$

The resistance for quantum tunneling can then be calculated from integrating equation **??** with Δx over angles ϕ and θ from the half of the sphere facing the other half. This can be simplified by taking four times the integral over a part of the area (both angles from 0 to $pi/2$). The resistivity for the sphere s then becomes:

$$R_\mathrm{s} = 4\frac{8\pi^2\hbar}{e^2}\frac{1}{AB\phi^{1/2}}\int_0^{\pi/2}\int_0^{\pi/2}\left(\Delta x(\phi,\theta)\exp(B\phi^{1/2}\Delta x(\phi,\theta))\right)d\phi d\theta \tag{C.4}$$

The ratio between the resistances of the sphere and plates can be taken and several constant terms drop out:

$$\frac{R_\mathrm{s}}{R_\mathrm{p}} = \frac{4\int_0^{\pi/2}\int_0^{\pi/2}\left(\Delta x(\phi,\theta)\exp(B\phi^{1/2}\Delta x(\phi,\theta))\right)d\phi d\theta}{d\exp(B\phi^{1/2}d)} \tag{C.5}$$

By substituting the values and calculating the integral with mathematica the equation was solved:

$$\frac{R_\mathrm{s}}{R_\mathrm{p}} \approx 6.3 \tag{C.6}$$

This would mean that the found resistance value is 6.3 times smaller than the actual resistance value of the junction. By using the cut-off frequency $f_\mathrm{c} = 1/(2\pi\omega RC)$ (this step uses the mismatch in area in the RC product, causing the problem), the capacitance then is 6.3 times bigger than the real value. Determining the resistivity and permittivity would result in a resistivity which is a factor 6.3 too small and a permittivity which is 6.3 times too big.

The used values are estimations, so in reality it is not known what the mismatch factor between the areas really is. From the above analysis it however becomes clear that it could a factor that adds to the too high permittivity. Further study is required for a clear view on the area mismatch. One side note can be given. Since the used models in this research are phenomelogical the determined resistivity and permittivity values can be used to describe the measured impedances.

D VCSEM Chamber Influence

In chapter 5 calibration curves for the VCSEM measurements are determined for both measurements with 250 V and 0 V detector voltage. In the second case, the measurements differ from theory in that for lower negative voltages there is also a decline in the measured SE intensity as shown in figure D.1 (this also happens a bit for the default detector operation as shown in figure 5.10). It is questioned if this effect can be caused by electric fields from the grounded sample stage and pole-piece in the SEM chamber.

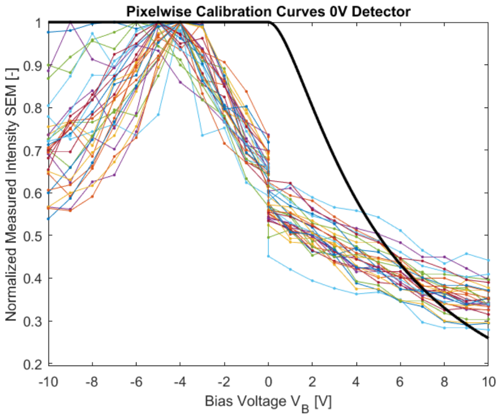

Figure D.1: Normalized calibration curves for a 3D-printed sample with 0 V detector voltage, showing a decline in SE intensity for large negative voltages that does not happen in the theoretical curve.

In literature it can indeed be found that all grounded objects in the SEM chamber have been proven to influence the SE extraction field (108). FEM simulations showed the electrical extraction field and the influence of the grounded objects, in figure D.2 (a.). Cazaux shows with calculated SE trajectories that a positive biasing of the sample holder re-attracts the SE below a certain kinetic energy, giving the collected spectra to contain more high-energy SEs. A negative biasing is shown to push the SEs towards the pole piece. However the deflection of the low-energy SEs is greater than that of higher energy SEs and hence the collected SE spectra are enriched with low-energy SEs (99).

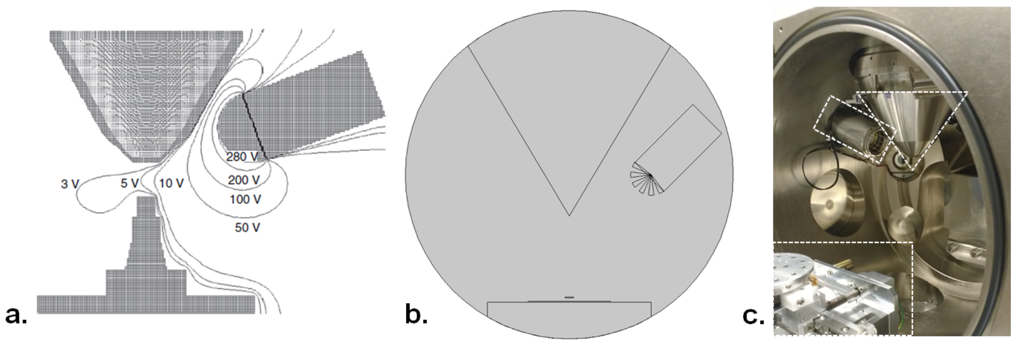

Figure D.2: a. FEM simulation of the SEM chamber with objects showing the potential everywhere (108); b. COMSOL geometry as used for the FEM simulations to determine the potential for the FEI quanta 450; c. the inside of the FEI quanta 450 with the pole piece, ET-detector and sample stage highlighted.

FEM simulations are performed in COMSOL to study the electric fields and trajectories to check this. The dimensions in this model are approximately based on the FEI quanta 450 and are only meant for checking the qualitative behaviour. Figure D.2 gives: a. the electric field as modelled by Konvalina et al., b. the FEM geometry as used for the simulations (the triangular shape is the lens pole piece, at the bottom the sample is placed on the sample stage and on the right the ET-detector is placed with its circular grid) and c. an image of the FEI quanta 450 internals with the ET-detector, pole piece and sample stage highlighted. The FEM simulations are performed with the COMSOL electrostatics module. The sample stage, substrate, walls, pole piece and detector are grounded (the scintillator of the detector is placed behind the grounded detector grid and has a high voltage of 10 kV), whereas the sample voltage is changed (−20 V, 0 V and 20 V). The simulations are performed with the default mesh size and parameter settings from the electrostatics module.

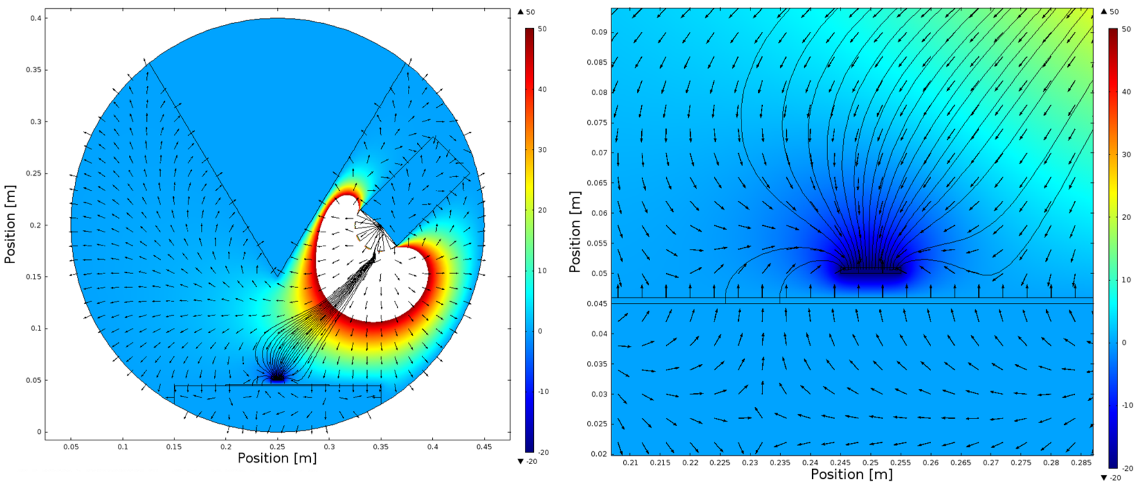

Figure D.3: Grounded substrate, −20 V on sample. View of the electric potential in the chamber (left) and a sample close-up.

D.1 Results

The results from the FEM simulations are shown in figure D.3, D.4 and D.5 for the sample voltages of −20 V, 0 V and 20 V respectively. An attractive field towards the detector for the SEs still exists despite the grounded detector grid, because of the high scintillator voltage. From the simulations it was found that the attractive field is highest for a grounded sample and substrate. For negative samples a part of the electrons is attracted towards the substrate, while for positive samples SEs with a low energy cannot escape the Coulombic attraction of the sample. Similar simulations with a different substrate voltage showed that the highest attraction field occurs for the case where the substrate and sample have the same voltage.

D.2 Discussion and Conclusion

The attraction fields have been simulated in the SEM by means of FEM analysis. It was shown that the ET-detector still creates an attractive electric field when its grid is set at 0 V, enabling measurements. The attraction fields for different sample voltages showed that the attraction is biggest if the sample and substrate have the same voltage. This has been determined from the electric field streamlines, these are not the actual SE trajectories. Depending on the kinetic energy of the SEs they will follow these streamlines more easily or not (with a higher kinetic energy the SEs are influenced less by the electric field). The shift from the highest intensity peak in the calibration data in figure D.1 is still unclear, but might be explained from negative charging of the substrate (which would yield the highest detected SE intensity when the substrate and sample have the same voltage). It is therefore advised to ground the substrate, since this yields the highest detector efficiency over the entire measurement range.

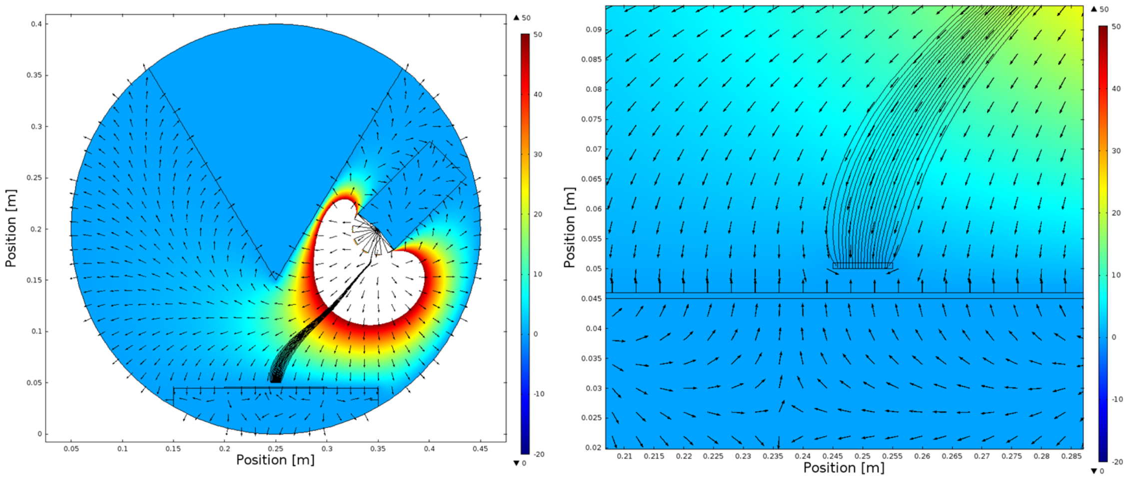

Figure D.4: Grounded substrate, 0 V on sample. View of the electric potential in the chamber (left) and a sample close-up.

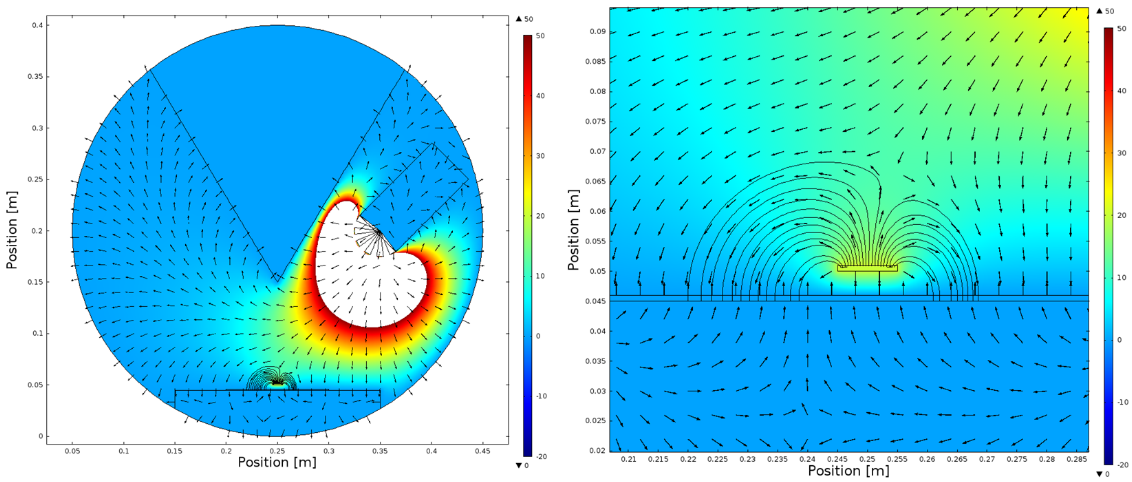

Figure D.5: Grounded substrate, 20 V on sample. View of the electric potential in the chamber (left) and a sample close-up.

E Paper Sample

The VCSEM measurements on 3D-Printed eTPU samples were sometimes difficult to interpret. At the same time the VCSEM method was researched and applied to samples with a difficult topography. To be able to test the method on a sample without a difficult geometry, an alternative was required. A simple alternative with a work function close to that of the carbon black particles was found in a pencil-on-paper sample. In literature research on pencil-on-paper sensors has already shown reliable sensors like strain gauges and chemiresistors (109; 110; 111), and therefore a pencil-on-paper sample was chosen as an eTPU alternative.

The sample is made by manually coloring an area of a piece of A4 printer paper with a soft, dark pencil (soft and dark indicates high graphite content and low clay content). A square of approximately 1 cm by 1 cm is cut out with opposite leads. The sample is fixed on a silicon wafer with a layer of kapton by means of copper tape and electrically connected via silver paint, figure E.1. SEM imaging at an acceleration voltage of 20 kV reveals the cellulose surface with graphite deposits, figure E.2. The light areas indicate larger graphite densities, from which it is difficult to determine the homogeneity of the graphite (and hence the resistivity).

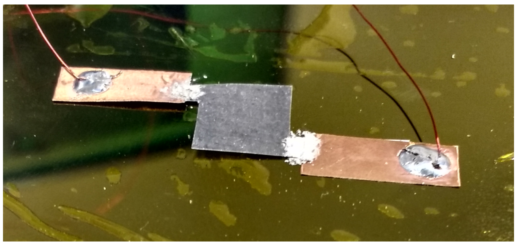

Figure E.1: A pencil-on-paper sheet on kapton with copper tape-silver paint connections.

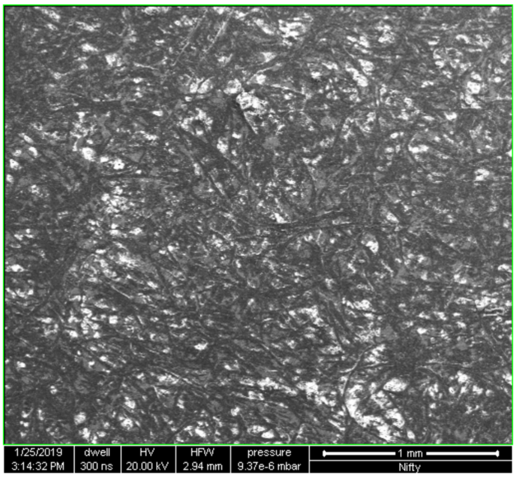

Figure E.2: SEM image of cellulose fibers and graphitic deposits on a paper surface.

Next VCSEM has been applied to study the voltage distribution of the sample with an acceleration voltage of 1 kV. A voltage of 5 V is applied to the lower left lead and of 0 V to the upper right lead in figure E.3a. The lack of topography yields little artifacts and noise as was desired, figure E.3a. In case the graphite is applied homogeneously, the measurements should show isotropic conduction with a similar voltage gradient at both leads. From the determined voltage however it can be seen that the resistivity around the lower left lead is higher than the resistivity around the upper right lead, indicating inhomogeneous spread of the graphite. The measured voltages on the leads have an error with respect to the applied voltages and are 5.1 V on the lower lead and −0.8 V in the upper lead.

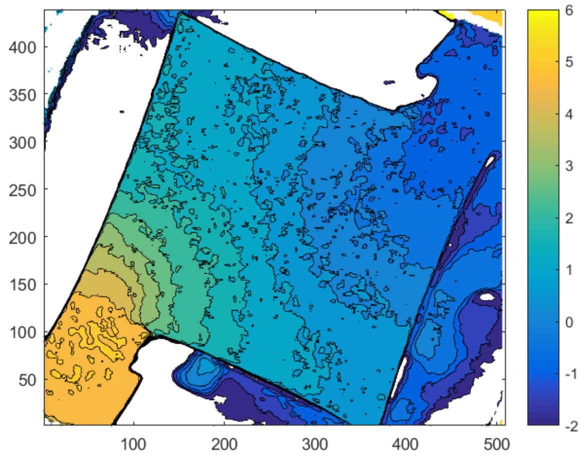

(a) The determined voltage distribution of the pencil-on-paper sample from a VCSEM measurement with a voltage applied to the leads of 0 V and 5 V. A larger voltage gradient is present in the lower left lead than in the upper right lead, indicating an inhomogeneous resistivity.

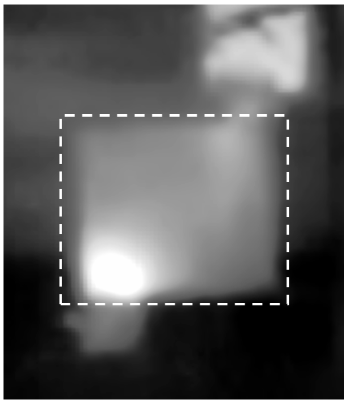

(b) IR thermography image of the pencil-on-paper sample, indicating a higher resistivity in the lower left lead than in the upper right lead.

Figure E.3: VCSEM (left) and IR thermography of a pencil-on-paper sample.

This inhomogeneous resistivity can also be seen in IR thermography measurements, as shown in figure E.3b. The heating around the lead with high resistivity, as found with VCSEM, is significantly higher than the heating in the other lead. This confirms the findings from the VCSEM measurement, showing inhomogeneous resistivity in the pencil-on-paper sample.

E.1 Conclusion

The pencil-on-paper sample could be used for VCSEM measurements with reduced topography, enabling better research on the VCSEM method. The smooth surface gives less topography artifacts, reducing the errors. Furthermore through a combination of VCSEM and IR thermography it was shown that the sample does not have a homogeneous resistivity and therefore most likely has an inhomogeneously spread graphite deposition. If the fabrication of pencil-on-paper samples and in particular the spreads of graphite deposit can be controlled, samples with tailored resistivity and anisotropy can be fabricated. Such samples can be used to study VCSEM artifacts.

F Analytical Model Dynamic VCSEM

This section derives the theoretical equations for the dynamic VCSEM method based on a general sinusoidal input signal. A linear approximation is given and compared to the full nonlinear model. For dynamic VCSEM it is important to realize that an AC signal covers a range of the DC SE intensity function $k_{\text{SE,DC}}$ every period as shown in figure 5.16. A new average SE intensity function can be derived for an AC signal by averaging over an entire period:

$$k_{\text{SE,AC}} = \frac{1}{T}\int_0^T \left(k_{\text{SE,DC}}(V(t))\right) dt \tag{F.1}$$

A general sinusoidal input signal can be described with:

$$V(t) = V_{\text{peak}} \sin\left(\frac{2\pi}{T}t\right) + V_{\text{bias}} \tag{F.2}$$

Important to note is the definition of $k_{\text{SE,DC}}$, which is defined on two intervals (chapter 5 for more information):

$$k_{\text{SE,DC}} = 1 \qquad \text{for} \quad V = [-\infty, 0] \tag{F.3}$$

$$k_{\text{SE,DC}} = \frac{3E+\phi}{6(E+\phi)^3} \qquad \text{for} \quad V = [0, \infty] \tag{F.4}$$

The transition between these two intervals can be calculated and depends on the offset in the input signal (V_{bias}). The zero crossings of the signal determine the integral bounds as shown in figure F.1. They can be determined by calculating where the unbiased function would cross the bias voltage:

$$t = \frac{T}{2\pi}\arcsin\left(\frac{-V_{\text{bias}}}{V_{\text{peak}}}\right) \tag{F.5}$$

The transitions are given for a positive bias smaller than the signal amplitude by (the values are similar for a negative bias only with a shift of half a period):

$$t_1 = \frac{\pi T + T\arcsin(V_{\text{bias}}/V_{\text{peak}})}{2\pi} \tag{F.6}$$

$$t_2 = \frac{2\pi T - T\arcsin(V_{\text{bias}}/V_{\text{peak}})}{2\pi} \tag{F.7}$$

The full integral then becomes:

$$k_{\text{SE,AC}} = \frac{\int_0^{t_1}\left(k_{\text{SE,DC}}(V(t))\right)dt}{T} + \frac{\int_{t_1}^{t_2}(1)\,dt}{T} + \frac{\int_{t_2}^{T}\left(k_{\text{SE,DC}}(V(t))\right)dt}{T} \tag{F.8}$$

Equation F.4 for the DC SE intensity is relatively complicated, hence first a linear approximation is made.

F.1 Linear Approximation Intensity

The linear approximation of the intensity curve is estimated from on the theoretical carbon equation while having an intensity of 1 at 0 V, giving a slope with a magnitude of $a = 1/10$ in the range of 0 V to 10 V. For now the general linear approximation is used (which is 1 at $V \leq 0$):

$$k_{\text{SE}} = -aV + 1 \tag{F.9}$$

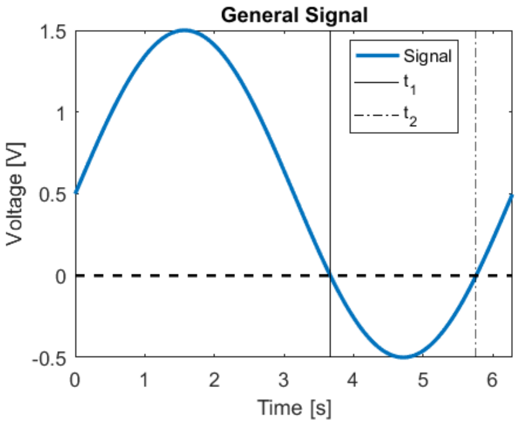

Figure F.1: Generalized sinusoïdal input signal, showing three distinct intervals.

The linear approximation of the intensity curve is only useful for the case in which the voltage crosses 0 V twice per period. In case the bias is negative and the voltage never exceeds 0 V, the theoretical result will always be an intensity of 1 everywhere. In case the bias is positive and exceeds the sine amplitude, the intensity is always linear and adds up to the same averaged intensity everywhere. Only in the case the voltage crosses 0 V two times per period a non-linear intensity-voltage relation arises for the curve around 0 V (where $V_{\mathrm{peak}} = V_{\mathrm{p}}$ and $V_{\mathrm{bias}} = V_{\mathrm{b}}$):

$$k_{\mathrm{SE,AC}} = \frac{\int_0^{t_1}\left(-a\left(V_{\mathrm{p}}\sin\left(\frac{2\pi}{T}t\right)+V_{\mathrm{b}}\right)+1\right)dt}{T} + \frac{\int_{t_1}^{t_2}(1)\,dt}{T} + \frac{\int_{t_2}^{T}\left(-a\left(V_{\mathrm{p}}\sin\left(\frac{2\pi}{T}t\right)+V_{\mathrm{b}}\right)+1\right)dt}{T} \tag{F.10}$$

Substituting the integral bounds from equation F.6 and performing the integration yields the final result for the linear approximation:

$$k_{\mathrm{SE,AC}} = \frac{-a}{\pi}\sqrt{V_{\mathrm{p}}^2 - V_{\mathrm{b}}^2} - aV_{\mathrm{b}}\left(\frac{\pi + 2\arcsin(V_{\mathrm{b}}/V_{\mathrm{p}})}{2\pi}\right) + 1 \tag{F.11}$$

From equation F.11 can be concluded that there is no frequency dependence for $k_{\mathrm{SE,AC}}$ (apart from limitations imposed by the SEM itself). Furthermore both the signal bias and amplitude influence the SE intensity. The response of the full nonlinear model has been determined numerically as shown in figure F.2 on the right. From this figure it can be seen that the general behaviour of the linear approximation fits well with the full model.

The percentual error between the linear form and the full nonlinear function is shown in figure F.3. In the area for which the negative bias is bigger than the amplitude the error is 0 (since the intensity is always 1 in this area). Besides this the error for 0 V bias with an arbitrary amplitude is relatively small.

F.2 Operation Modes

Both the bias and amplitude of the signal can be chosen, and hence the measured SE intensity can be tailored. For simple driving either the bias of the whole sample with respect to ground (bias mode) or amplitude of the harmonic driving (amplitude mode) can be varied for calibration and for the signal (using both requires a combination of multiple function generators). The bias mode is used for the active VCSEM, which results in the DC voltage distribution. In case of dynamic VCSEM with bias mode the SE curves become smoothed around 0 V as shown in figure F.4. For dynamic VCSEM the amplitude mode will be used, since adding a bias to the applied AC signal will result in a potential distribution that is a combination of the potential distibution at DC and at the used AC frequency (giving a bivalent result). TThe amplitude mode on the other hand is only influenced by the voltage drop (giving a monovalent result).

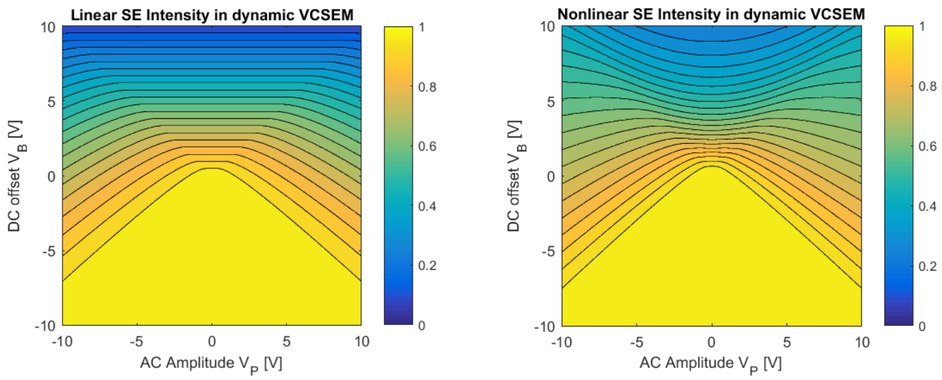

Figure F.2: Linear and Nonlinear SE intensity functions with their dependence on signal bias and amplitude.

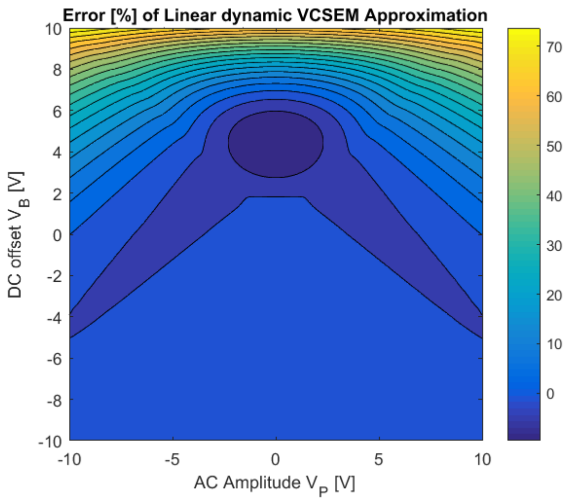

Figure F.3: The percentual error of the linear SE intensity approximation as compared to the full nonlinear function.

F.3 Analytical Amplitude Mode

Both a linear and nonlinear equation can be derived for the amplitude mode. The bias is taken as 0 V and for simplicity a period of 2π is assumed, giving an input signal of:

$$V = V_{\text{peak}} \sin(t) \tag{F.12}$$

For the linear approximation equation F.11 reduces to:

$$k_{\text{SE,AC,linear}} = \frac{-a}{\pi} V_{\text{peak}} + 1 \tag{F.13}$$

For the full nonlinear equation the following integrals have to be calculated, using the analytical expression for the SE intensity (and normalizing it, the maximum value is $\frac{1}{6\phi^2}$):

$$k_{\text{SE,AC}} = \frac{\int_0^{\pi} \left(6\phi^2 \frac{3V_p \sin(t)+\phi}{6(V_p \sin(t)+\phi)^3}\right) dt}{2\pi} + \frac{\int_{\pi}^{2\pi} (1)\, dt}{2\pi} \tag{F.14}$$

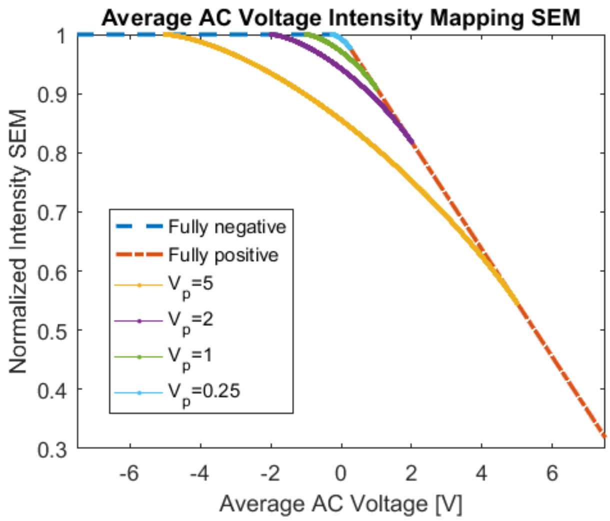

Figure F.4: The linear analytical bias mode expression for various amplitudes.

This has been computed with the Mathematica software package, yielding:

$$k_{\text{SE,AC,amplitude}} = \frac{\sqrt{-V^2+\phi^2}\left(2V\phi(2V^2+\phi^2)+\pi(V^4+\phi^4(1+\sqrt{\frac{\phi^2}{-V^2+\phi^2}}-2V^2\phi^2(1+2\sqrt{\frac{\phi^2}{-V^2+\phi^2}})))\right)}{2\pi(V-\phi)^2(V+\phi)^2\sqrt{-V^2+\phi^2}} + \frac{(8V^2\phi^3-2\phi^5)\arctan\left(\frac{V}{\sqrt{-V^2+\phi^2}}\right)}{2\pi(V-\phi)^2(V+\phi)^2\sqrt{-V^2+\phi^2}} \tag{F.15}$$

The comparison of the linear and nonlinear model are shown in figure F.5.

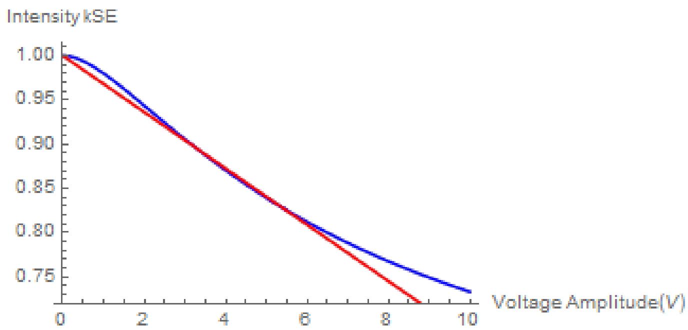

Figure F.5: The linear and nonlinear analytical amplitude mode expressions.

G Heat Transfer Modelling

The modelling of the heat transfer from the sample is done with a steady state lumped model. A rectangular flat sample on top of a glass plate is taken. On the bottom of the glass substrate cooling takes place while on the top natural convection takes place (radiation is neglected, since it is very low compared to the conduction and convection at this temperature). The parameters for the model (for conduction, convection and radiation) are given in table G.1.

The heat flux of the three types of heat transfer can be calculated through:

$$\dot{Q}_{\mathrm{cond}} = -kA\frac{\nabla T}{L} \tag{G.1}$$

$$\dot{Q}_{\mathrm{conv}} = hA_{\mathrm{s}}(T_{\mathrm{s}} - T_{\mathrm{a}}) \tag{G.2}$$

$$\dot{Q}_{\mathrm{rad}} = \epsilon\sigma A_{\mathrm{s}}(T_{\mathrm{s}} - T_{\mathrm{a}}) \tag{G.3}$$

(G.4)

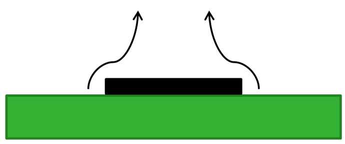

Figure G.1: Schematical drawing of natural convection from the heated horizontal 3D-printed sample on a substrate.

For convection calculations the convection coefficient h is required. There is no active cooling on the top sample of the sample, so natural convection has to be considered (shown in figure G.1). The convection coefficient can be calculated approximately from the empirical relations below. These equations calculate the average heat transfer coefficient from the isothermal upper surface of a flat plate. First the average temperature T_{f} of the heated film of air above the sample is calculated (equation G.5), from which the film density ρ can be calculated (equation G.6). Then the thermal diffusivity of the film air α is calculated (equation G.7). The dominant heat transfer is calculated through the Prandtl number Pr (equation G.8), which gives the ratio between momentum diffusivity and thermal diffusivity in the air film (to calculate whether convection or conduction is dominant). The Grashoff number Gr is calculated after this (equation G.10) and indicates the ratio of buoyancy to viscous forces (to determine if natural convection takes place, the buoyancy forces need to overcome the viscous forces for this to happen). For the Grashoff number the characteristic length of the sample L_{c} is used (equation G.9) to give a length scale basis. The finally the Rayleigh number Ra can be calculated from previous results (equation G.11), which gives a value in which regime of natural convection the sample is. Depending on the range of the Rayleigh number, the Nusselt number Nu gives the ratio of convective to conductive heat transfer at the sample surface (equations G.12 and G.13). Finally the convective heat transfer coefficient is a part of the Nusselt number, and can therefore be derived from it (equation G.14). For more information on this calculation and natural convection the reader is referred to (112).

Parameter	Value	Unit	Description
T_a	295	(K)	ambient temperature
T_s	-	(K)	sample temperature
W	0.8e-3	(m)	traxel width
L	15e-3	(m)	sample length
C_p	1007	($\mathrm{J\,kg^{-1}\,K^{-1}}$)	specific heat air at constant pressure, room temperature
B	0.0262	($\mathrm{K^{-1}}$)	thermal expansion coefficient air at 25 °C
k	0.0261	($\mathrm{W\,m^{-1}\,K^{-1}}$)	thermal conductivity air, room temperature
μ	1.85e-5	(Pa s)	dynamic viscosity, room temperature
g	9.81	($\mathrm{m\,s^{-2}}$)	gravitational acceleration
p	101325	(Pa)	air pressure, room temperature
R_s	287.058	($\mathrm{J\,kg^{-1}\,K^{-1}}$)	specific gas constant for dry air
k_{glass}	1.05	($\mathrm{W\,m^{-1}\,K}$)	thermal conductivity glass, room temperature
L_{glass}	1e-3	(m)	thickness glass wafer
ϵ	0.95	(-)	estimated emissivity sample
σ_{SB}	5.67e-8	($\mathrm{W\,m^{-2}\,K^{-4}}$)	Stefan-Boltzmann constant

Table G.1: Lumped thermal model parameters.

$$T_f = \frac{T_a - T_p}{2} \tag{G.5}$$

$$\rho = \frac{P}{R_s T_f} \tag{G.6}$$

$$\alpha = \frac{k}{\rho C_P} \tag{G.7}$$

$$Pr = \frac{\mu}{\rho\alpha} \tag{G.8}$$

$$L_c = \frac{WL}{2W + 2L} \tag{G.9}$$

$$Gr = gB(T_a - T_p)\frac{L_c^3}{\nu^2} \tag{G.10}$$

$$Ra = GrPr \tag{G.11}$$

$$Nu = 0.59Ra^{0.25} \qquad (200 < Ra < 10^4) \tag{G.12}$$

$$Nu = 0.96Ra^{1/6} \qquad (1 < Ra < 200) \tag{G.13}$$

$$h = \frac{Nuk}{L_c} \tag{G.14}$$

H Abstract FLEPS 2019

The abstract as submitted and accepted for the IEEE International Conference on Flexible and Printable Sensors and Systems 2019 (IEEE FLEPS 2019).

Characterizing the Electrical Properties of Anisotropic, 3D-Printed Conductive Sheets

Alexander Dijkshoorn, Martijn Schouten, Gerjan Wolterink, Remco Sanders and Gijs Krijnen
University of Twente, Robotics and Mechatronics, Enschede, the Netherlands
a.p.dijkshoorn@alumnus.utwente.nl

Summary And Motivation

This paper introduces characterization techniques to investigate electrical properties of 3D printed conductors. It presents a physical model to describe frequency dependent electrical properties of 3D-printed conductors; the use of infrared thermography to characterize electrical anisotropy in 3D-printed sheets and the use of the voltage contrast Scanning Electron Microscopy method (VCSEM) to determine potential distributions in 3D-printed sheets. The characterization methods could enable improvement of 3D-printed transducer design and exploit electrical properties of 3D-printed conductors.

Advances over Previous Works

3D-printing conductors, and in particular transducers, by means of fused deposition modelling is an upcoming research area [1], where 3D-printed piezo resistive, EMG and capacitive sensors have been demonstrated [2] and a significant amount of research has been done on electrical properties of conductive-polymer composites for printing [3,4]. However, printing conditions remarkably affect the electrical properties due to voids and bonding conditions between adjacent traxels (i.e. track-elements), as shown by measurements and simulations [4,5]. Insight is gained by developing appropriate physical models, representing conductive structures by fused traxels. In previous research conductance was already described in this way; however this was limited to a 1D-solution in the DC-case [6]. Furthermore, electrical characterization has primarily focused on global impedance measurements, whereas the 2D distribution of the electrical impedance is of interest. Here we show that IR thermography, so far used for studying heating power in 3D-printed samples [4], can also be used for studying the anisotropic electrical properties of 3D-printed samples as has been done for characterization of carbon fibre reinforced polymers [7]. Next it is shown that VCSEM, used e.g. to characterize conducting networks in CNT composites [8], can also be applied to 3D printed conductors.

Fig. 1: Printed sample design with leads on opposite (a) and same (parallel) side (b).

Methodology

Two different printing designs are used, with leads on the opposite and parallel side (Fig 1). The conductors are simulated by means of traxels with bulk (resistivity ρ, relative permittivity ϵ_r) and mutual contact properties (inter-traxel resistivity σ, inter-traxel capacitance C_0) to describe the electrical characteristics, making it an AC-extension of the work by Hampel et al. [6]. An equivalent electrical network to represent these properties is shown in Fig 2.

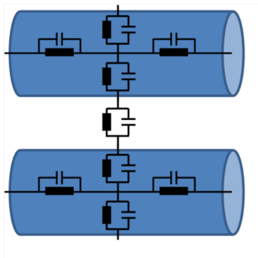

Fig. 2: Physical model showing traxels with an equivalent electrical network representing the 2D bulk and inter-traxel

Finite Element Experiments are performed for validation of the FEM simulations with COMSOL software.

CAD designs are sliced with Simplify3D and 3D printed from flexible carbon black-filled TPU (Palmiga Innovations PI-ETPU 85-700+ [9]) using a Flashforge with Flexion extruder. The samples are single-layer sheets of 15mm by 15mm printed on glass wafers with electrical contact leads on either the same (parallel) or opposite side (Fig 1), made via copper tape with Ag-conductive paint (Electrolube SCP26G).

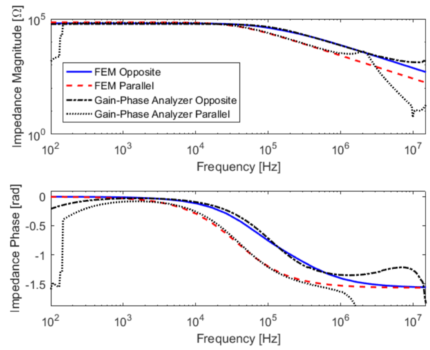

Fig. 3: Impedance and phase data of the FEM simulations in comparison with the gain-phase measurements.

Impedance measurements are done using a gain-phase analyser (HP 4194A). Since printing conditions influence contact properties, the two dissimilar designs (Fig 1) are fitted separately. DC thermal measurements are based on temperature increases due to resistive heating, using infrared thermography with an IR camera (FLIR ONE Gen 2). However, actual heat transport may cause differences between simulations and measurements. To have more clear measurements, samples with larger inter-traxel resistivity are used for the thermal measurements.
DC VCSEM measurements are done with an FEI Quanta 450, where the different leads have a different bias relative to the ground of the SEM. A more positive bias reduces the number of secondary electrons reaching the detector, giving rise to a nonlinear dependency [8]. By means of creating a SEM intensity calibration curve for a sample for different voltages, voltage distributions of samples are reconstructed by fitting and inverting in a pixel-wise manner to reduce SEM artefacts.

IV. Results and Discussion

Fig 3 shows the gain-phase measurements compared to the FEM simulations showing a good fit from 1 kHz to 1 MHz. The fitted parameters are presented in Tab 1. Some deviations occur at both lower (around 100Hz) and higher frequencies (around 1MHz) for which the cause is still unclear.

Variable \ Sample	Opposite	Parallel
Resistivity ρ $[\Omega m]$	2.8	2.8
Relative permittivity ϵ_r [-]	0.9e5	1.5e5
Inter-traxel resistivity σ $[\Omega m^2]$	2e-3	2e-3
Inter-traxel capacitance C_0 $[F/m^2]$	2.8e-4	4e-3

Tab. 1: Fitting parameters for the impedance and VCSEM simulations.

Fig 4 shows the dissipated power density in the FEM simulations compared to measured thermal images with temperatures ranging from 24˚C to 28˚C. The general power and temperature distributions are similar, with most dissipation in the leads and around the edges. Though the

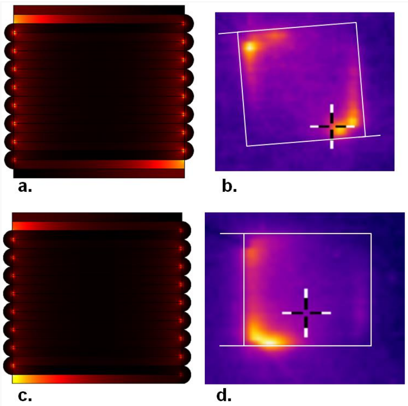

Fig. 4: DC Power density of FEM (a, c) simulations versus thermal measurements (b, d) of the opposite lead (fig. 1.a) and parallel lead sample (fig 1.b).

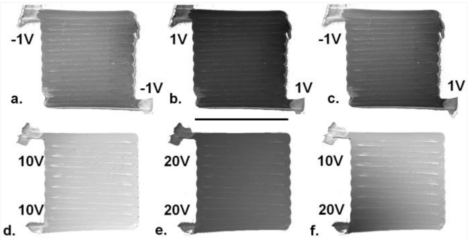

Fig. 5: VCSEM results with constant voltage images for calibration (a, b, d, e) and the contrast of a measured voltage distribution (c, f) of the opposite lead (fig 1.a) and parallel lead sample (fig 1.b). The central bar indicates 15mm.

measurements have a more spread out distribution, which is expected to be due to thermal conduction.
Fig 5 shows DC VCSEM images as used for pixel-wise calibration (4.a, 4.b, 4.d, 4.e) and as used for voltage distribution analysis (4.c, 4.f). The calibration images have the same contrast everywhere in the samples, apart from the topographic and edge effects of the SEM. The measured voltage distribution images show a clear transition in contrast between both leads.
Fig 6 gives the corresponding FEM simulations and experimental results, showing both qualitatively and quantitatively good correspondence. The results show almost isotropic conduction in the samples, due to a low contact resistance (Tab 1).

In conclusion characterization methods have been presented to predict the electrical properties of 3D-printed conductors in combination with a physical model for FEM simulations. Classical impedance measurements have been used as validation of the FEM simulations. Infrared thermography and voltage contrast SEM have been applied for DC characterization, showing promising results. Future work will focus on the influence of the printing parameters on the inter-traxel properties and on improving the characterization methods and extending them to AC measurements.

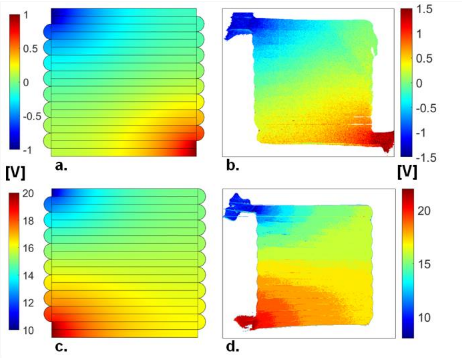

Fig. 6: VCSEM DC voltage distribution of FEM simulations (a,c) compared to the experimental results (b, d).

REFERENCES

[1] Xu, Y.; Wu, X.; Guo, X.; Kong, B.; Zhang, M.; Qian, X.; Mi, S.; Sun, W., "The Boom in 3D-Printed Sensor Technology,". Sensors 2017, 17, 1166.

[2] Dijkshoorn, A., Werkman, P., Welleweerd, M., Wolterink, G., Eijking, B., Delamare, J., Sanders, R., and Krijnen, G. J. M.: "Embedded sensing: integrating sensors in 3-D printed structures," J. Sens. Sens. Syst., 7, 2018, pp. 169-181.

[3] Kwok, S.W.; Goh, K.H.H.; Tan, Z.D.; Tan, S.T.M.; Tjiu, W.W.; Soh, J.Y.; Ng, Z.J.G.; Chan, Y.Z.; Hui, H.K.; Goh, K.E.J., "Electrically conductive filament for 3D-printed circuits and sensors," Appl. Mater. Today, 2017, 9, pp. 167–175.

[4] Watschke, H., Hilbig, K., Vietor, T., "Design and Characterization of Electrically Conductive Structures Additively Manufactured by Material Extrusion," Appl. Sci. 2019, 9, 779.

[5] Zhang, J.; Yang, B.; Fu, F.; You, F.; Dong, X.; Dai, M., "Resistivity and Its Anisotropy Characterization of 3D-Printed Acrylonitrile Butadiene Styrene Copolymer (ABS)/Carbon Black (CB) Composites," Appl. Sci. 2017, 7, 20.

[6] Hampel, B., Monshausen, S., Schilling, M., "Properties and applications of electrically conductive thermoplastics for additive manufacturing of sensors," Tech. Mess. 2017, 84, pp. 593–599.

[7] Athanasopoulos N., Kostopoulos V., "A comprehensive study on the equivalent electrical conductivity tensor validity for thin multidirectional carbon fibre reinforced plastics," Composites Part B, 2014, 67, pp. 244–255.

[8] Spallek, S., "Electron Microscopy Studies on Structure-property Relationships of Nanoparticulate Transparent Electrodes for Printed Electronics," Ph.D. thesis, 2016, Friedrich-Alexander-Universität, Erlangen-Nürnberg.

[9] Palmiga Innovations, Rubber 3d printing, http://rubber3dprinting.com.